# Proceedings of

# 15th
# European Fuel Cell Forum
# 2011

# Chapter 11 - Session A13

## Fuel Cell Modelling


**Edited By**
Andreas Friedrich (Chair)
Wolfgang G. Bessler
Günter Schiller
Norbert Wagner

**Co-Edited By**
Olivier Bucheli
Robert Leibinger
Javad Motevallian
Leandra Spirig
Michael Spirig
Nancy Thamke





www.efcf.com

# Chapter 11 - Session A13
# Fuel Cell Modelling

**Content** **Page A13 - ..**

A1301

# Understanding Water Removal from Fuel-Cell Gas-Diffusion Layers

**Prodip Das[2], Haluna P Gunterman[1,2], John Newman,[2] and Adam Z Weber[1]**
[1]Lawrence Berkeley National Laboratory
1 Cyclotron Rd, MS 70-108B
[2]University of California
Berkeley, CA, 94720, USA
Tel.: +1-510-486-6308
Fax: +1-510-486-4773
azweber@lbl.gov

## Abstract

It is well known that for PEFCs operating below 100°C, water management is a critical issue. If there is too much water, then the catalyst layers and GDLs will become saturated with liquid water and flood; if there is too little, then the membrane becomes highly resistive. In terms of flooding, the liquid water blocks the access of oxygen to the reaction sites. Key in controlling water management is the impact of the GDLs, especially on the cathode side of the cell. Within these layers, two-phase flow dominates and, especially at lower temperatures, where water is removed from their surface in liquid form. Single-droplet existence has been studied by various groups, but these studies do not necessarily include the impact of multiple droplets and also depend on contact-angle hysteresis of droplets placed on the GDL surface to predict the adhesion force. The above issues will be discussed and an approach to alleviate them introduced including experimental measurements of the adhesion force and droplets using a tilted goniometer. Combined with a theoretical treatment of the pressure force, on can begin to predict droplet instability and movement. In addition, an approach using a combined liquid-surface coverage and a fluctuating capillary-pressure boundary condition will discussed along with capillary-pressure measurements for the liquid saturation.

# Introduction

Water management in proton-exchange-membrane fuel cells (PEMFCs) is critical for optimum fuel-cell performance. This is especially true at lower temperatures, where water exists as a liquid and phase-change-induced flow is insufficient to remove the product water in the vapor phase [1]. There is a need to understand liquid-water movement and removal from the cell and thus the gas-diffusion layer (GDL). In addition, liquid water in these various materials can limit performance due to blocking either gas transport pathways or reaction sites. In this work, the water properties including capillary pressure – saturation relationships and droplet and water removal will be discussed.

# 1. Water Removal in the Vapor Phase

Water can be removed from the PEMFC in either the liquid or vapor phases. Obviously, if the inlet gas streams are subsaturated, a water-vapor partial-pressure gradient will exist and move water from the catalyst layer and into the gas channel. However, even under saturated conditions, water can move through the vapor phase due to a vapor-pressure gradient that is setup due to the temperature gradient in the cell [1-2]. A schematic of this phase-change-induced (PCI) flow is shown in Figure 1.

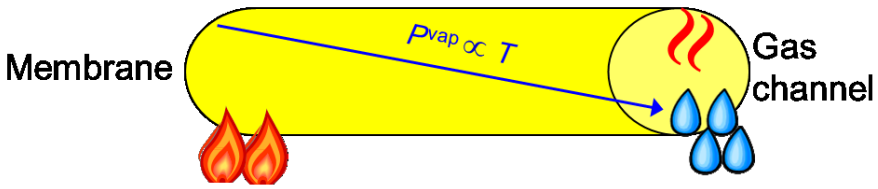


Figure 1. Schematic of PCI flow.

PCI flow will be dominant at higher operating temperatures, where the saturation or vapor pressure varies more significantly with temperature. A simple calculation using Stefan-Maxwel equations and isobaric conditions [3-4] will show that PCI flow can be dominant at higher temperatures and results in mass-transport limitations as shown in Figure 2. From the top graph in Figure 2, one can see that only a small temperature gradient is necessary to remove the electrochemically generated water, especially at 80°C. Such an effect can be the main driver of water out of the cell which is beneficial in avoiding liquid-water flooding. However, in the bottom graph of Figure 2, one can see how the temperature gradient reduces performance by lowering the oxygen concentration. The figure shows that both the dilution effect at the higher temperature and the PCI flow decrease the oxygen partial pressure at the catalyst layer.

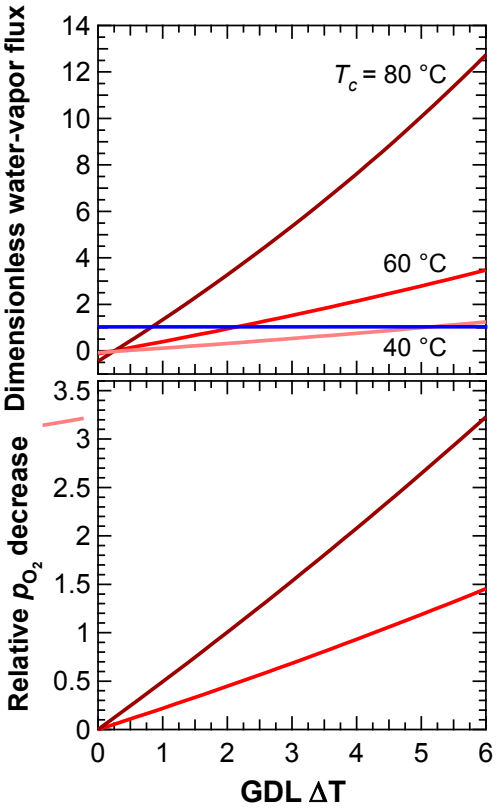


Figure 2. Results of simple calculation showing impact of PCI flow where the blue line in the top figure indicates the water-production rate.

## 2. Water Removal in the Liquid Phase

For liquid water, removal is often through liquid-water droplets from the surface of the cathode GDL. These droplets can also cause water holdup due to increased capillary pressures and through the water uptake or saturation, which can be related to the material pore-size and contact-angle distributions [5]. A significant amount of experimental and theoretical work devoted to the study of droplet dynamics in PEMFC gas-flow channels has already highlighted some of the fundamental issues [6-8]. Most of these studies, however, are based on the contact-angle hysteresis and a static force balance on a single droplet,

$$F_P + F_G + F_A = 0 \quad (1)$$

where P, G, and A, denote the pressure, gravitation, and adhesion or surface-tension force, respectively. The gravitational force has been shown by us and others to not be significant under normal fuel-cell conditions and droplet sizes. While the overall force-balance approach is fine, the contact-angle hysteresis does not provide an accurate estimation of the adhesion force, which is the dominating force holding a droplet on the GDL surface and preventing its detachment. Therefore, we have designed and used a tilted-plate experiment to quantify and directly measure the sliding angles and adhesion forces for liquid -water droplets on the GDL surfaces. The experimental setup used in the tilted-plate experiment to measure the sliding angles and adhesion forces is shown in Figure 3.

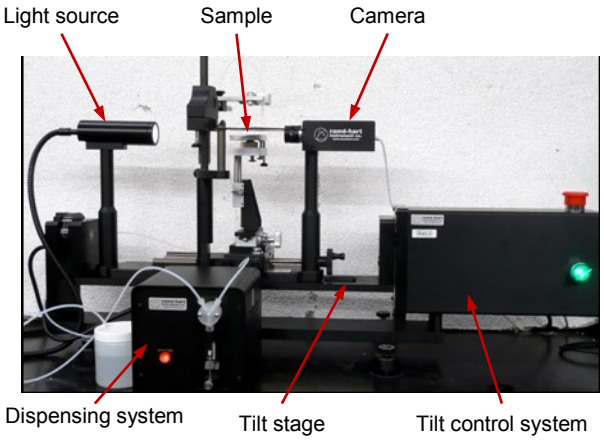


Figure 3. Experimental apparatus (tilted-plate goniometer) to measure adhesion force.

In the experiments, two droplet placement methods (placed on a horizontal surface and placed on a tilted surface) are investaged. Figure 4 shows how the sliding-angle experiment is performed.

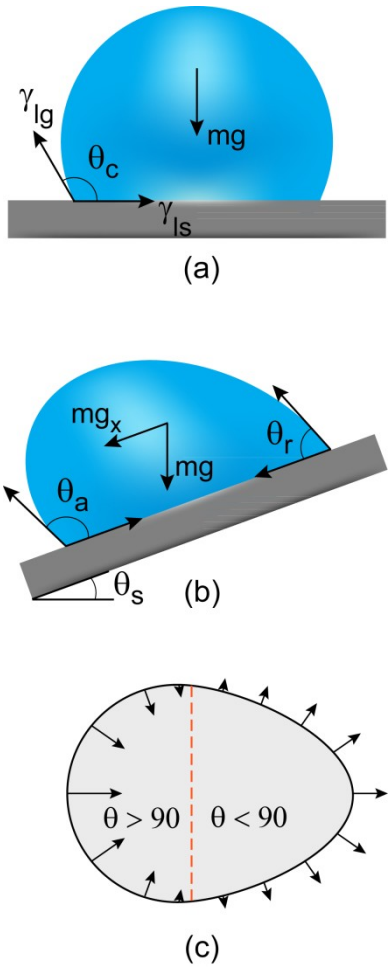


**Figure 4**. Illustration of contact angles and forces acting on a liquid water droplet on a hydrophobic GDL surface. (a) Static contact angle (θc) with the body gravity force (mg) and surface tension forces (γlg and γls). (b) Advancing (θa) and receding (θr) contact angles and sliding angle (θs). (c) Top view of the adhesion force distribution that is parallel to the GDL surface; dashed line shows contact angle transition through 90°.

Some preliminary results are shown in Figure 5, clearly demonstrating that larger injection volumes results in less angles due to the mass increase as explained in Figure 4. The figure also shows the sensitivity of the measurement technique, which is greater than that of static, horizontal contact angles.

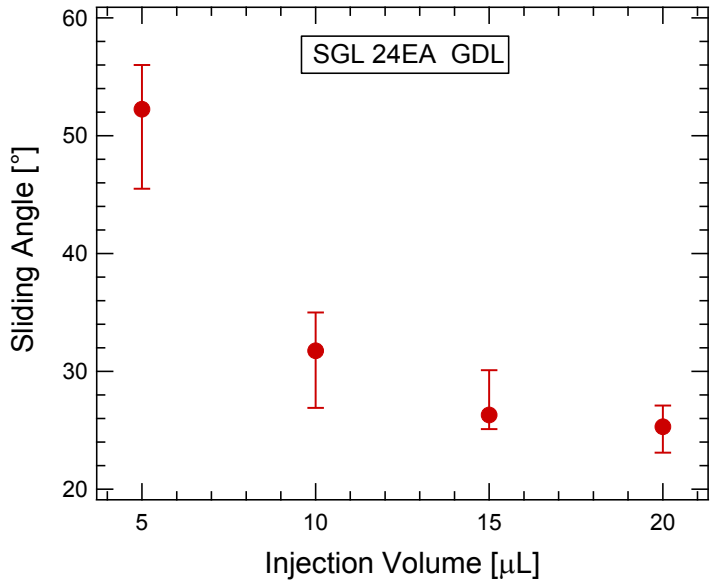


Figure 5. Effect of injection volume on the mean sliding angle for SGL 24EA GDL.

## 3. Bottom-Injected Droplets

In addition to changing the angle and determining the adhesion force on a droplet on top of the GDL, we devised a stage so that one can inject water through the GDL and image the droplets on the surface. The two measurement techniques are contrasted in Figure 6 for droplets at rest and at incipient inclination where the droplet begins to slide. As seen, while the contact angle of the droplet on the flat surface is similar for both the top and bottom injections, the bottom injection requires a much higher inclination angle, which is due to the increased adhesion between the droplet and the underlying water reservoir. This result highlights the fact that analysis with surface drops is inadequate in capturing the correct underlying physics.

Another impact of injection through the bottom, is that multiple droplets can exist as shown in Figure 7. In the figure, part (a) shows that multiple droplets are growing on the GDL surface. Part (b) indicates that the droplet which has favorable water-transport path underneath of it is growing and it coalescences with a smaller droplet. Part (c) indicates exactly the same nature like part (b) and also indicates that the droplet that has unfavorable water-transport path underneath of it remains unchanged. Part (d) shows that the bigger droplet coalescences with nearby smaller droplets before detaching from the GDL surface. Both Figures 6 and 7 demonstrate that our derived method of adhesion-force determination results in a more realistic description of actual fuel-cell phenomena.

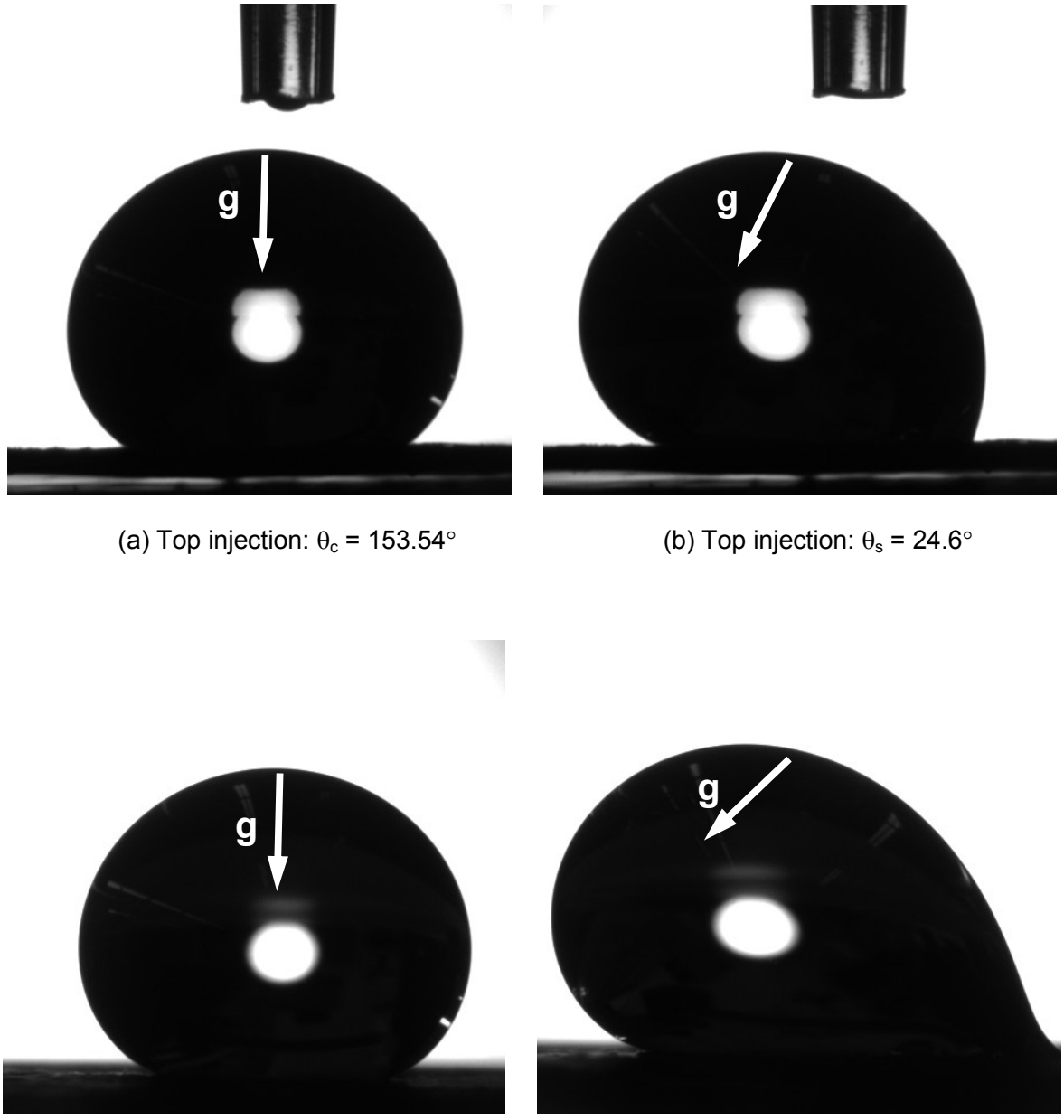


(a) Top injection: $\theta_c$ = 153.54°

(b) Top injection: $\theta_s$ = 24.6°

(c) Bottom injection: $\theta_c$ = 152.69°

(d) Bottom injection: $\theta_s$ = 44.9°

Figure 6. Snapshots of liquid-water droplet (20 μl) on SGL 24EA using two injection methods. Parts (a) and (c) show without inclination and parts (b) and (d) show with inclination (drop about to slide) results. In the bottom injection method, liquid water was injected through a small hole (about 100 μm diameter) on the GDL

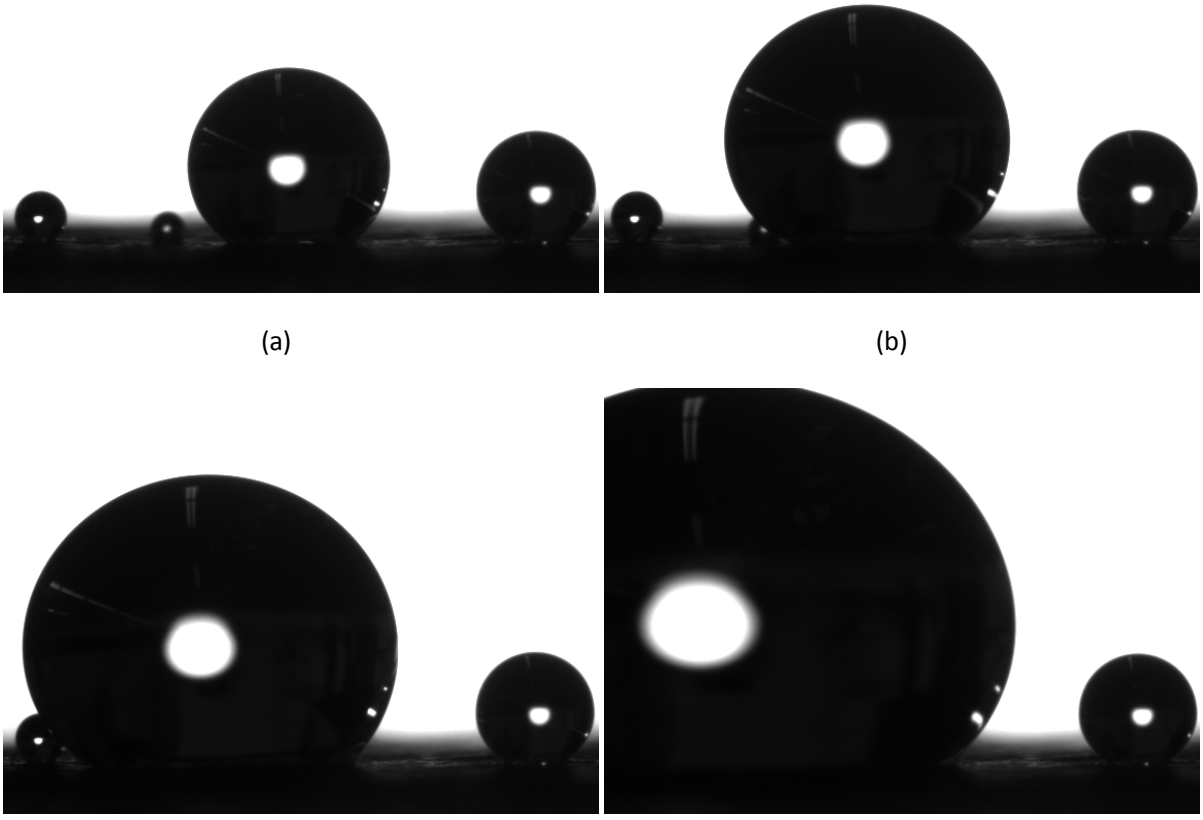


Figure 7. Snapshots of the liquid-water droplet growth on SGL 24DA.

## 3. Calculation of the Pressure Force on a Droplet

As shown in equation 1, to determine water-droplet instability or movement requires a balance between the adhesion and pressure forces (since gravity is negligible in a PEMFC environment for the droplets). In the above section, we have shown how one can measure the adhesion force. For the pressure or drag force, we have used a control-volume approach to determine its value as shown in Figure 8.

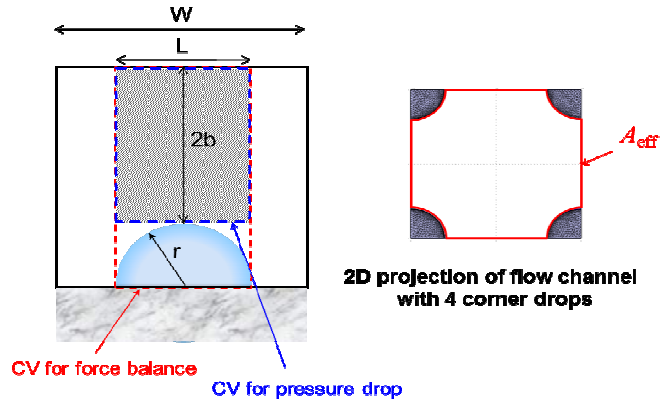


Figure 8. Control volumes for calculation the pressure force.

The pressure force can be calculated through some relatively straightforward modification of the pressure force derived in the literature [7]. The modifications results in

$$\Delta P = \frac{a\mu U_{\text{eff}} L}{H_{\text{eff}}^2}$$

$$a = 12\left[1 - \frac{192}{\alpha\pi^5}\tanh\left(\frac{\alpha\pi}{2}\right)\right]^{-1};\ U_{\text{eff}} = \frac{UH}{H_{\text{eff}}};\ H_{\text{eff}} = \frac{A_{\text{eff}}}{W};\ A_{\text{eff}} = A_{\text{ch}} - nA_{\text{drop}} \quad (2)$$

where $\alpha$ is the effective aspect ratio, $U_{\text{eff}}$ is the effective gas velocity, $H_{\text{eff}}$ is the effective channel dimension, and $A_{\text{eff}}$ is the effective cross-sectional area. This equation was compared to literature approaches and detailed finite-volume calculation using Comsol Multiphysics as show in Figure 9.

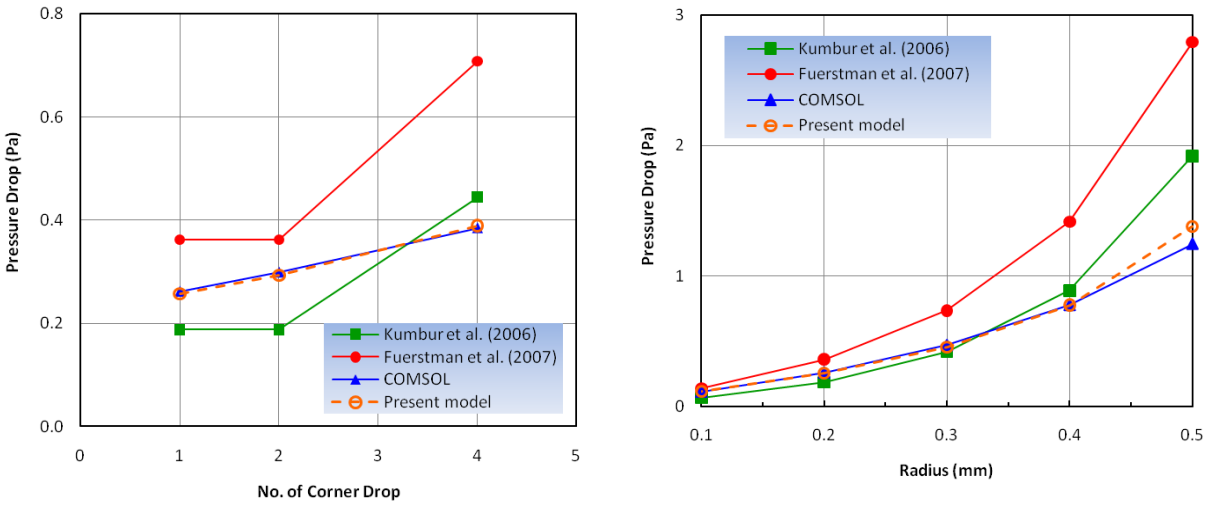


Figure 9. Comparisons of our pressure-drop correlation and those in the literature [7-8] to the detailed numerical one from Comsol.

## 4. Impact of Droplets on Transport

The above force balance and approach can predict when a droplet will become unstable and move or detach from the GDL surface or underlying water film. The number of droplets can be used to determine the overall surface area that contains liquid water, and this surface area reduces the area into which the reactant gases can diffuse. While one does not expect significant impacts at low surface coverages, as one increases the coverage that becomes similar to having a larger rib-to-channel ratio. Such an increase causes more significant mass-transport limitations, which can be predicted for a 1-D model using an effective GDL thickness through a conformal-mapping approach [9].

In addition to the surface coverage, with the prediction of the incipient droplet size, one can predict the liquid pressure at the GDL surface. This liquid pressure minus the gas pressure is the capillary pressure of water in the medium. Through experiments pioneered by Gostick et al. [10], we can measure this relationship as shown in Figure 10. Thus, knowing the droplet sizes, we average over the surface and also time-average to come up with the average capillary pressure, which can be used to get the saturation as a boundary

condition using either the data directly or fits to the data using pore-size and contact-angle distributions [5].

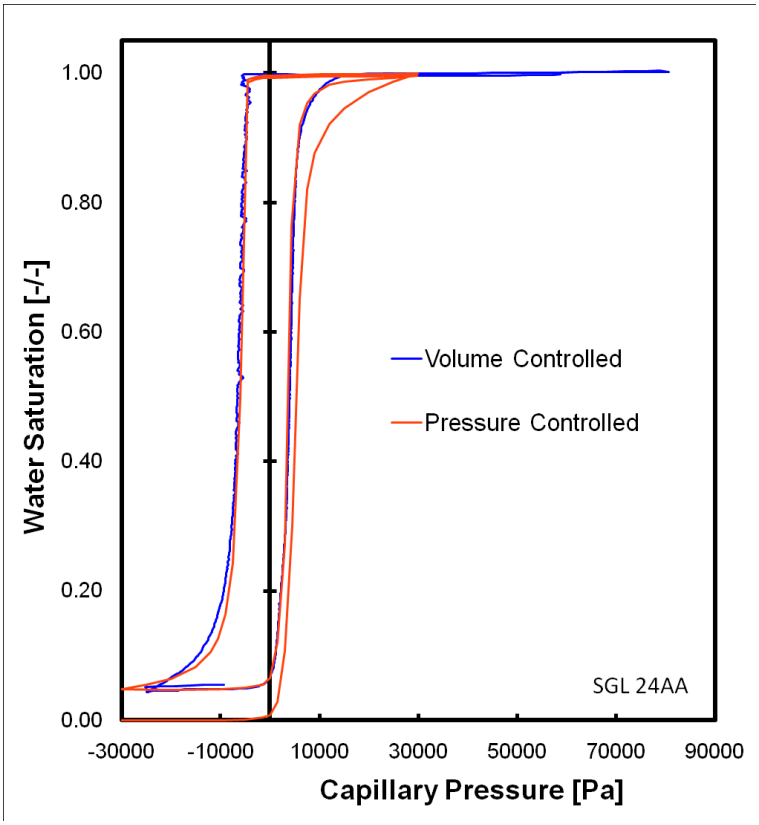


Figure 10. Saturation as a function of capillary pressure for SGL 24AA GDL using two different control methods. The injection curves require positive pressures while the withdrawal curves require negative pressures.

## Conclusions

Management of water is critical for optimal fuel-cell operation. At higher temperatures, the temperature gradient from the catalyst layer to the gas channel can move water through the vapor phase, even with humidified feed conditions. However, at lower temperatures, there is the issue of removing water in the liquid phase as droplets from the GDL surface. In order to predict droplet instability and detachment, a force balance is used. While the pressure or drag force on the droplet can be derived, the adhesion or surface-tension force requires measurement using a sliding-angle approach. It is shown that droplets produced by forcing water through the gas-diffusion layer rather than placing them on top of it show much stronger adhesion forces owing to the contact to the subsurface water as well as the existence of multiple droplets. Using the approaches and values for the adhesion and pressure forces, one can determine the rate and number of droplet detachments or movement from the GDL surface. These can then be related to the capillary pressure in the droplet and hence the saturation of the GDL. In addition, one can also look at where the droplets go in terms of coalescence, wicking into a channel corner, etc.

## Acknowledgment

This work was supported by the DOE EERE Funding, Office of Fuel Cell Technologies under contract number DE-AC02-05CH11231 and Toyota Motor Company under a CRADA agreement. We also acknowledge SGL Carbon for providing GDL materials.

## References

[1] A. Z. Weber and M. A. Hickner, Electrochim. Acta **53** (26), 7668-7674 (2008).
[2] S. Kim and M. M. Mench, J. Electrochem. Soc. **156** (3), B353-B362 (2009).
[3] R. B. Bird, W. E. Stewart and E. N. Lightfoot, *Transport Phenomena*, 2nd ed. (John Wiley & Sons, Inc., New York, 2002).
[4] J. Newman and K. E. Thomas-Alyea, *Electrochemical Systems*, 3rd ed. (John Wiley & Sons, New York, 2004).
[5] A. Z. Weber, J. Power Sources **195**, 5292-5304 (2010).
[6] K. S. Chen, M. A. Hickner and D. R. Noble, International Journal of Energy Research **29** (12), 1113-1132 (2005).
[7] E. C. Kumbur, K. V. Sharp and M. M. Mench, J. Power Sources **161** (1), 333-345 (2006).
[8] M. J. Fuerstman, A. Lai, M. E. Thrlow, S. S. Shevkoplyas, H. A. Stone and G. M. Whitesides, Lab on a Chip **7** (11), 1479-1489 (2007).
[9] A. Z. Weber, Electrochim. Acta **54** (2), 311-315 (2008).
[10] J. T. Gostick, M. A. Ioannidis, M. W. Fowler and M. D. Pritzker, Electrochemistry Communications **10** (10), 1520-1523 (2008).

A1302 (Abstract)

# Two phase Pore Network Model of the cathode catalyst layer of the PEMFC: application to the analysis of gas diffusion and effect of wettability

**Mohamed El Hannach, Joël Pauchet and Marc Prat**
CEA, LITEN
LCPEM
17, rue des Martyrs
38054 Grenoble
France
Tel.: +33-4-38781713
mohamed.el-hannach@cea.fr

## Abstract

Understanding the liquid and gas phase transport inside the cathode catalyst layer (CCL) of the PEM fuel cell is an important step in the process of performance improvement.
The reactant (oxygen) is transported by diffusion, and water is supposed to be produced in liquid phase from the oxygen reduction reaction (ORR). Water transport is mainly driven by capillary effects. The two-phase transport phenomena are coupled through the ORR.
The pore network modelling (PNM) is well adapted for the multiphase transport in porous medium. It is used in this work to simulate the two-phase transport inside the secondary pores of the CCL. 3D regular networks made of spherical pores and cylindrical throats are constructed to describe the porous structure of the CCL. The effect of the structural and wetting properties of the CCL on the two-phase transport is studied.
The results show that liquid water clusters have different shapes depending on the wettability (hydrophobic, hydrophilic and mixed) of the pores, which affects the liquid water distribution inside the network, and then the oxygen effective diffusivity.

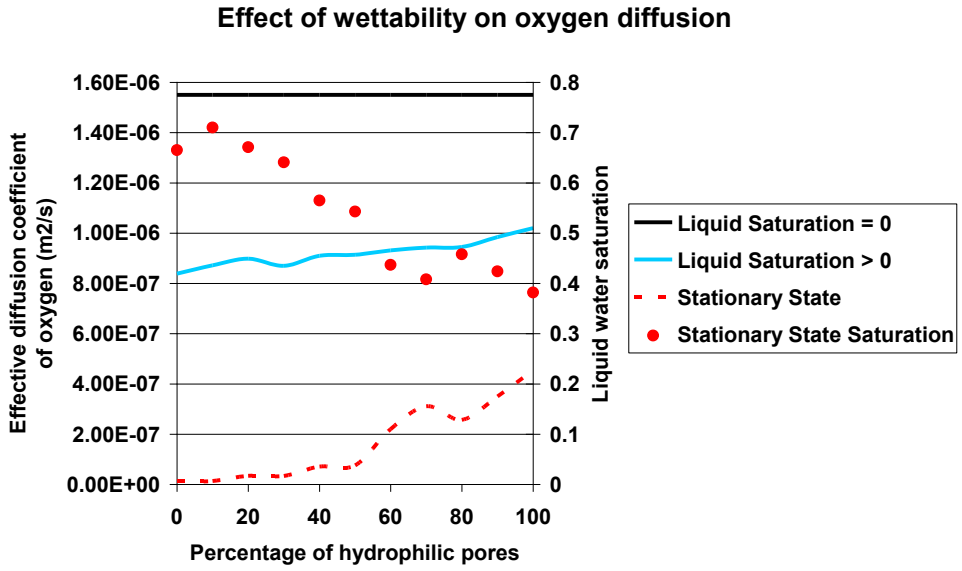

A1303

# A Numerical Model Predicting Liquid Water Saturation within the Cathode Electrode of a Proton Exchange Membrane Fuel Cell

**Naveed Akhtar and Piet J.A.M. Kerkhof**
Technical University, Eindhoven
Department of Chemical Engineering and Chemistry
Den Dolech 2, P.O.Box 513
5600 MB, Eindhoven
The Netherlands
Tel.: +31-622-296029
Fax: +49-040-2446653
N.Akhtar@tue.nl

## Abstract

A two-phase, half cell, model of a proton exchange membrane fuel cell cathode has been developed with emphasis on the liquid water saturation within the three porous layer structure, i.e. the catalyst layer, the micro-porous layer and the gas-diffusion layer. The model was run under varying current density, operating temperature, relative humidity and gaseous flow rate. The results show that the calculated liquid saturation profiles strongly depends on the local distribution of these variables which are highly coupled. For example, an under-humidified gas feed entering into the cell, first undergoes through the evaporation regime at low current densities, followed by liquid-water generation at moderate current densities, and finally evaporation of the liquid-water at higher current densities due to increase in the cell temperature. The increase in air flow rate enhances the liquid-water saturation within the catalyst layer, near the channel area, and reduces its amount under the ribs. The reduced liquid-saturation under the ribs is due to higher local temperature because of increased reactant transport that results in its evaporation. In summary, prediction of liquid-water saturation within the cathode is a highly complicated phenomenon that is strongly coupled to the above variables.

## Introduction

Proton exchange membrane fuel cells (PEMFCs) show their interest in portable market, such as, in automotive and small scale applications where quick start-up, shut-down is required [1]. Due to operation at relatively low temperatures, i.e. in the range of 40-80°C, they are quite suitable for stationary applications [2]. On one hand, this low operating temperature is useful; on the other hand, it causes the water management problems inside the PEMFCs. The lower operating temperature range of PEMFCs allows two-phases of water to co-exist. The water that has been produced in liquid via electrochemical route may turn into vapor form and vice versa. The combined effect of relative humidity, operating temperature and current density is crucial in determining the form in which the water exists inside the porous medium [3]. Irrespective of the operating values, the local distribution of these variables does also play an important role in calculating their distribution inside the porous medium. For example, increasing the operating temperature is advantageous in lowering the overpotentials, but higher temperature may results in drying of the membrane because of excessive vaporization. Increasing the operating current density generates additional heat that may further promote the vaporization of the produced liquid water and eventually membrane dry out [4]. Once the membrane becomes dry, it loses its ionic conductivity for proton conduction; therefore, performance of the cell will drop. As understood from above, the quite complicated water management inside the PEMFC cathode is highly coupled with the heat transport effects that sensitively depend upon current distribution inside the cell.

Furthermore, the bipolar plates in PEMFCs are usually embedded with provision for channels and lands. The presence of channels allows the gases to flow in a specified manner to be transported to the active layers. The use of land areas permits electrical connection with the porous layers for the transfer of electrical current [5,6]. It should be noted that the presence of channels and lands could also affect the transport behavior inside the PEMFCs. These different areas could give different temperature distribution inside the porous medium, as the thermal conductivity near the land and channel area may be influenced by the non-uniform temperature distribution [7-9]. The presence of channel and land areas could add further complexity in the distribution profiles of above transport parameters. The present study is therefore aiming at investigating those effects, especially taking into account the presence of land and channel areas. The model employed in this study is previously developed by us and has been briefly described below. For detailed formulation and the background assumptions, the reader is referred to Ref: [4].

| Dimensions | Values (mm) |
|---|---|
| Length of gas-diffusion layer | 50 |
| Length of micro-porous layer | 50 |
| Length of catalyst layer | 50 |
| Thickness of gas-diffusion layer | $350 \times 10^{-3}$ |
| Thickness of micro-porous layer | $50 \times 10^{-3}$ |
| Thickness of catalyst layer | $10 \times 10^{-3}$ |

Table 1: Geometry dimensions

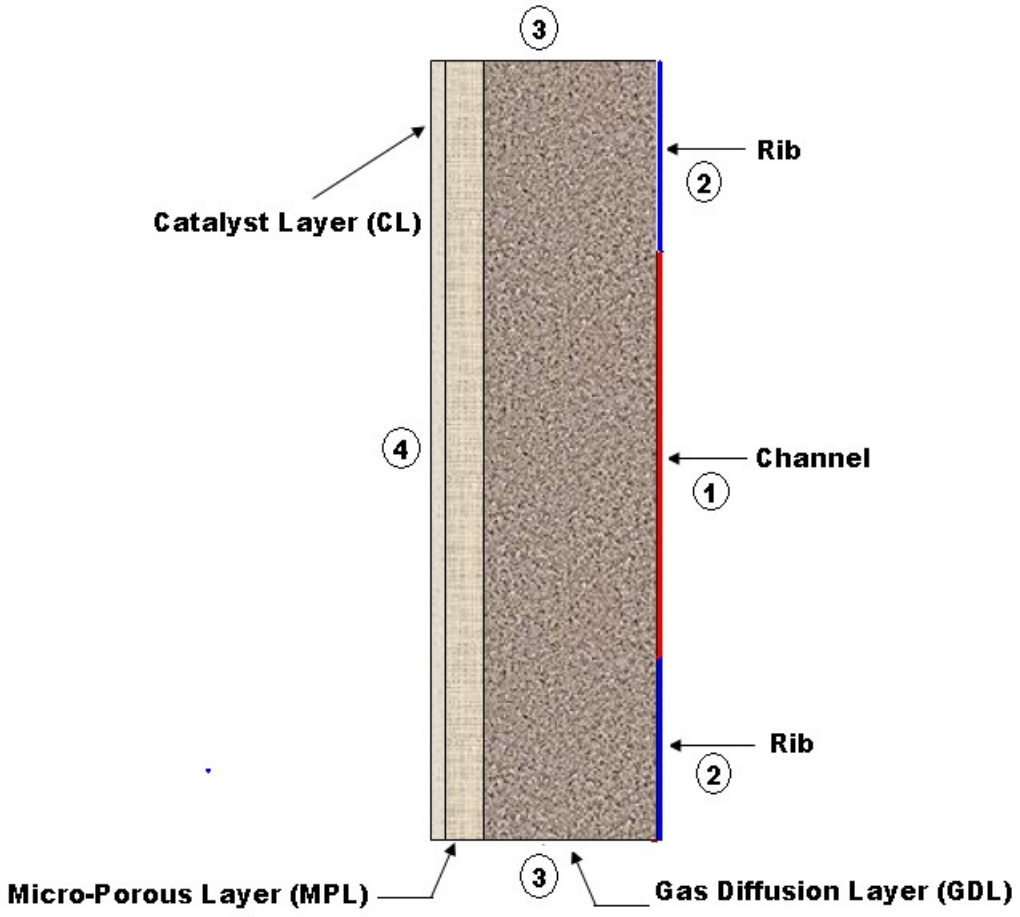


Figure 1

## Modeling Approach

The model geometry has been shown in Figure 1, with dimensions listed in Table-1. The model employs mass, momentum, species, energy and liquid water transport equation for the two-phase transport inside the PEMFC cathode. The two phase transport has been accomplished using two-fluid approach. The corresponding source and sink terms have been accommodated in respective equations for liquid and gas phase. The phase change term has been incorporated in all porous layers, and the corresponding heat transfer effects are included via condensation/evaporation mechanism. The liquid water transport equation was custom developed via partial differential equation (PDE) module of COMSOL, 3.5a. All other equations were directly available in the commercial package. Table-2, shows the modeling equations used with boundary conditions listed in Table-3.

| Domain | Equation solved |
|---|---|
| $\Omega_{GDL/MPL}$ | $\nabla \cdot (\rho_g u_g) = S_{phase}$<br>$\nabla p_g = -\frac{\mu_g}{k k_{rg}} u_g$<br>$\nabla \cdot (\rho_l u_l) = S_{phase}$<br>$\nabla p_l = -\frac{\mu_l}{k k_{rl}} u_l$<br>$\nabla \cdot (\rho_g u_g Y_i) = \nabla \cdot (\rho_g D_i^{eff} Y_i) + S_{phase,i}$<br>$\nabla \cdot \left( (-k_{eff} \nabla T) + (\rho C_p)_{eff} u T \right) = Q_{GDL/MPL}$ |
| $\Omega_{CL}$ | $\nabla \cdot (\rho_g u_g) = S_r + S_{phase}$<br>$\nabla p_g = -\frac{\mu_g}{k k_{rg}} u_g$<br>$\nabla \cdot (\rho_l u_l) = S_l + S_{phase}$<br>$\nabla p_l = -\frac{\mu_l}{k k_{rl}} u_l$<br>$\nabla \cdot (\rho_g u_g Y_i) = \nabla \cdot (\rho_g D_i^{eff} Y_i) + S_{r,i} + S_{phase,i}$<br>$\nabla \cdot \left( (-k_{eff} \nabla T) + (\rho C_p)_{eff} u T \right) = Q_{CL}$ |

Table 2: Modeling equations

| | |
|---|---|
| 1 | $s = s_{in}, u_g = u_{in}, n \cdot (-k \nabla T) = 0, Y_{H2O} = \frac{RH_{in} P_{H2O}^{sat} M_{H2O}}{p M_{mix}}$ |
| 2 | $n \cdot (\nabla S) = 0, u = 0, T = T_o, n \cdot \left( -\rho D_{eff} \nabla \mathrm{Y_i} + \rho \mathrm{u Y_i} \right) = 0$ |
| 3 | $n \cdot (\nabla S) = 0, u = 0, n \cdot (-k \nabla T), n \cdot \left( -\rho D_{eff} \nabla \mathrm{Y_i} + \rho \mathrm{u Y_i} \right) = 0$ |
| 4 | $n \cdot (\nabla S) = 0, u = 0, n \cdot \left( -k_{eff} \nabla T \right)_{in} = n \cdot \left( -k_{eff} \nabla T \right)_{out}, n \cdot \left( -\rho D_{eff} \nabla \mathrm{Y_i} + \rho \mathrm{u Y_i} \right) = 0$ |

Table 3: Boundary conditions

## Numerical Implementation

The model equations were developed in COMSOL, Multiphysics, 3.5a. The computations were performed on a 32-node Linux cluster; 32 x dual 3 GHz Intel Xeon Sun Fire V60 servers each with 4GB memory. The system of equations was solved using a parametric solver with a total computing time of 31.5 minutes.

## Results and Discussion

The values of various electrochemical/hydrodynamic transport parameters were taken from our earlier study, Ref: [4]. Figs. 2-5 show distribution of different parameters, each at three distinct operating temperatures of 80, 60 and 40°C, respectively. The cathode feed was under-humidified having an inlet relative humidity of 30%, unless stated otherwise. Furthermore, the results are computed at three different current densities of 0.25, 0.75 and 1.25 $Acm^{-2}$ as shown in the figures.

- **Liquid water saturation:**

Figure 2 (a-c) shows the liquid water saturation distribution at three different operating temperatures of 80, 60 and 40°C, respectively. As can be seen in Figure 2(a), with increase in current density, the liquid saturation is increasing near the catalyst layer/membrane interface. With a partially humidified gas feed (RH = 30%), under-saturation is taking place, as soon the gas enters the gas diffusion electrode. With increase in operating current density, the under-saturation effects diminish because of water generation within the catalyst layer due to electrochemical conversion. The land areas which were dryer before became saturated due to the flow movement via capillary effect. The catalyst area directly facing the channel has a higher liquid saturation as compared to the area covered by the land. This is due to short diffusion path of the incoming oxygen that reacts electrochemically with a very low resistance path to encounter. In Figures 2(b) and 2(c), the increasing liquid saturation under the land area is due to more water production at higher current densities that ultimately transport from the catalyst layer towards land areas via capillary fingering and phase change induced effect.

- **Oxygen distribution:**

Figure 3 (a-c) shows the oxygen distribution at three distinct operating temperatures of 80, 60 and 40°C, respectively. Figure 3(a) shows that oxygen is quickly consumed directly in front of channel area within the catalyst layer. The land areas are not fully accessible to oxygen, therefore, oxygen starvation could be observed in those locations. Furthermore, with increasing current density, more and more oxygen is consumed within the catalyst layer and oxygen starved region is extending. An interesting thing to note is that with increase in temperature, the inlet oxygen mass fraction decreases (see Figure 3 (a-c)). This behavior of oxygen mass fraction with increase in temperature is related to the vaporization of the electrochemically produced liquid water. With increasing temperature, more liquid water is evaporated; therefore, the mass fraction of oxygen decreases with increase in water vapor.

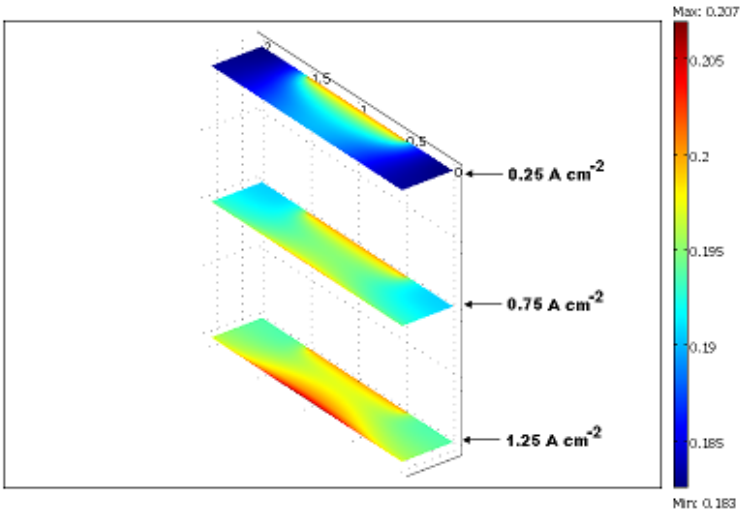


(a)

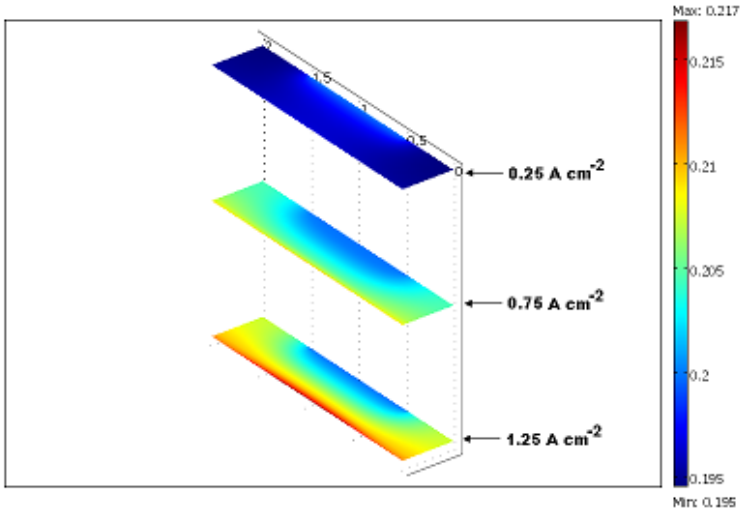


(b)

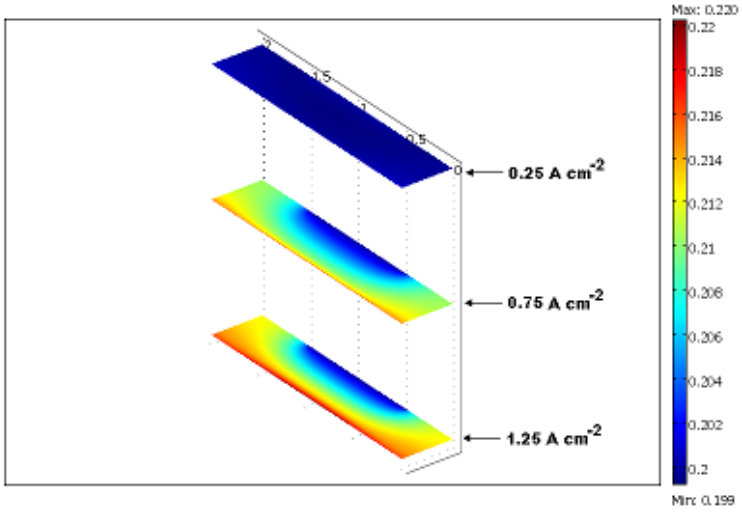


(c)

Figure 2: Liquid water saturation distribution for RH_in = 30% at three different operating temperatures of: (a) 80°C, (b) 60°C and (c) 40°C.

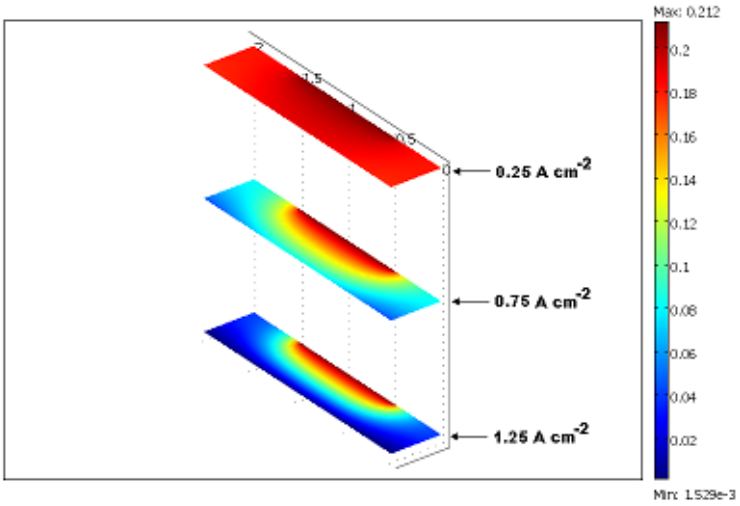


(a)

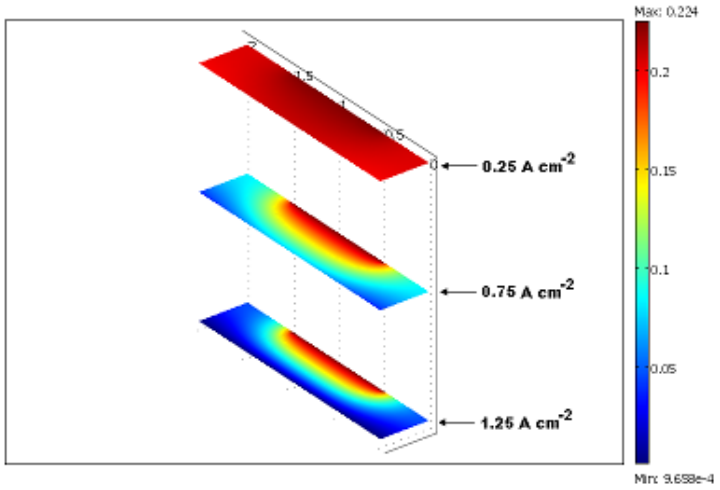


(b)

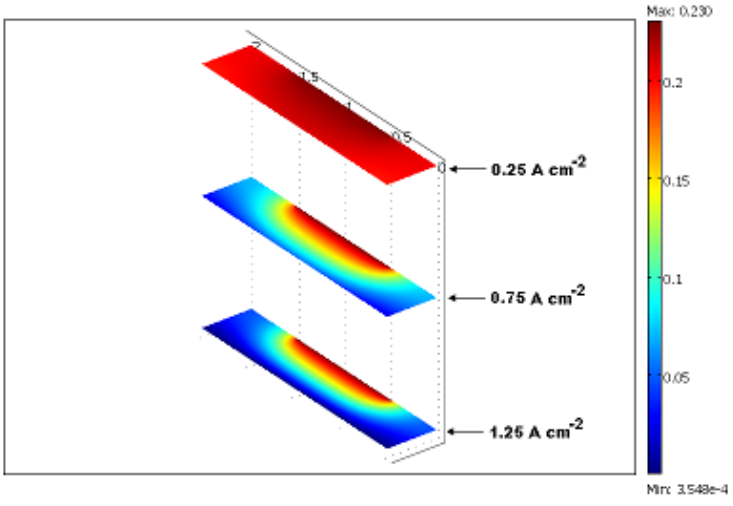


(c)

Figure 3: Oxygen distribution for RH_in = 30% at three different operating temperatures of: (a) 80°C, (b) 60°C and (c) 40°C.

- **Temperature distribution:**

Figure 4(a-c) shows the temperature distribution for three different operating temperatures of 80, 60 and 40°C, respectively. As can be seen, the local temperature is increasing with increase in operating current density. Furthermore, the evaporation phenomenon is taking place, which is strong at lower current densities. With increase in current density, heat is produced as a result of electrochemical water production. This addition of heat partially offset the evaporation and shrinks the evaporation zone. It should be noted that operation with under-humidified feed may result in cooling of the cell due to evaporation effect. This cooling will ultimately lower the cell performance due to reduced reaction rate. Another important observation to note is that with decrease in temperature, the maximum value of local temperature increases and its minimum value decrease. This is due to more condensation at lower operating temperatures which adds more heat into the porous

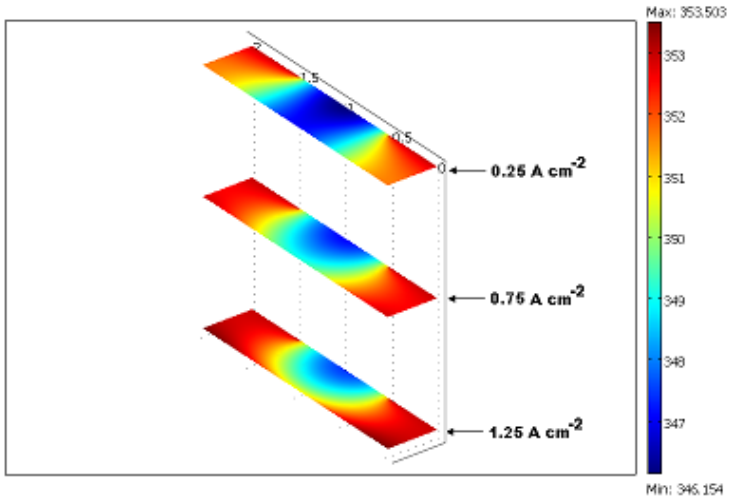


(a)

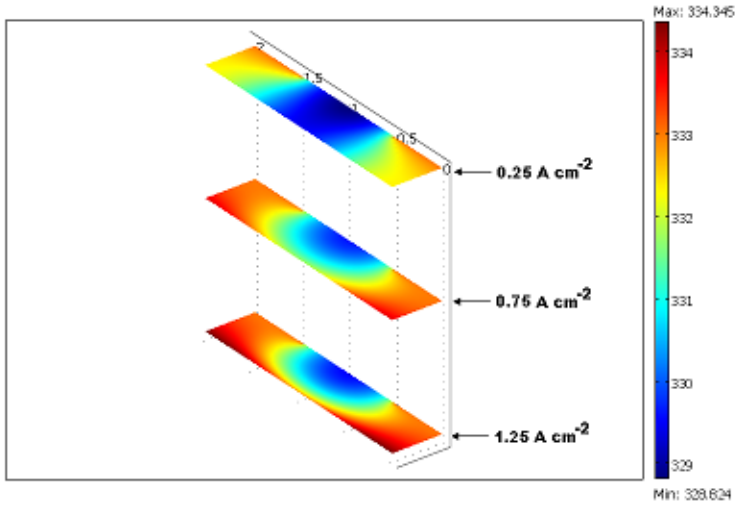


(b)

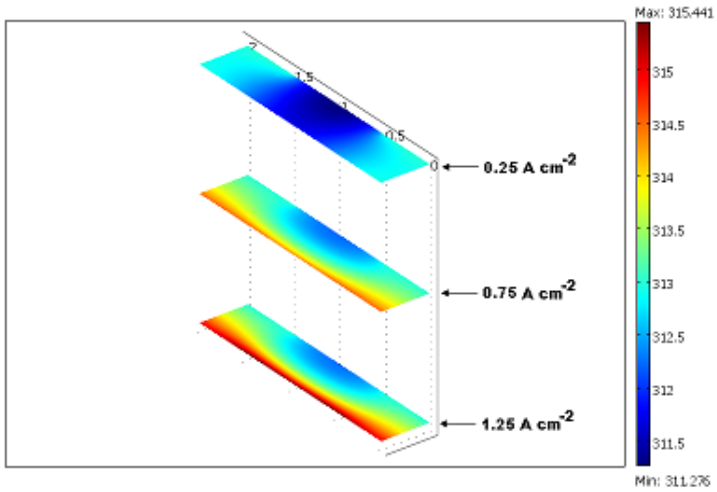


(c)

Figure 4: Temperature distribution for RH_in = 30% at three different operating temperatures of: (a) 80°C, (b) 60°C and (c) 40°C.

medium. The higher rates of cooling are shown in Figures 4(a) and 4(b), as compared to Figure 4(c). This cooling of the cell is due to evaporation at higher operating temperatures.

- **Relative humidity distribution:**

Figure 5 (a-c) shows the relative humidity distribution inside the cathode electrode for three different operating temperatures of 80, 60 and 40°C, respectively. As can be seen from Figure 5(a), with increase in temperature, the maximum value of relative humidity decreases. However, the land areas show an increase in relative humidity with increasing current density. The contradicting behavior of relative humidity under land and channel areas is due to local temperature distribution in those locations. A higher temperature inside the catalyst and near the land regions increases the relative humidity because of evaporative removal of water, whereas cooler zones at the channel entrance are subjected to condensation.

From the above discussion it is clear that when the operating temperature was reduced to 60°C, the liquid saturation was increased as compared to the value observed at 80°C. This increase in liquid saturation shows promotion of condensation effect at lower operating temperatures. A similar trend was observed for the liquid saturation with a further decrease in operating temperature down to 40°C. As explained earlier, the reduction in operating temperature offers more oxygen in the inlet feed. This higher amount of oxygen could be useful, as it could prevent oxidant starvation under certain conditions. However, reduced operating temperature is not desirable as it lowers the performance due to insufficient proton conduction through the membrane. Consequently, a trade-off between these parameters is essential for better functioning of the cell.

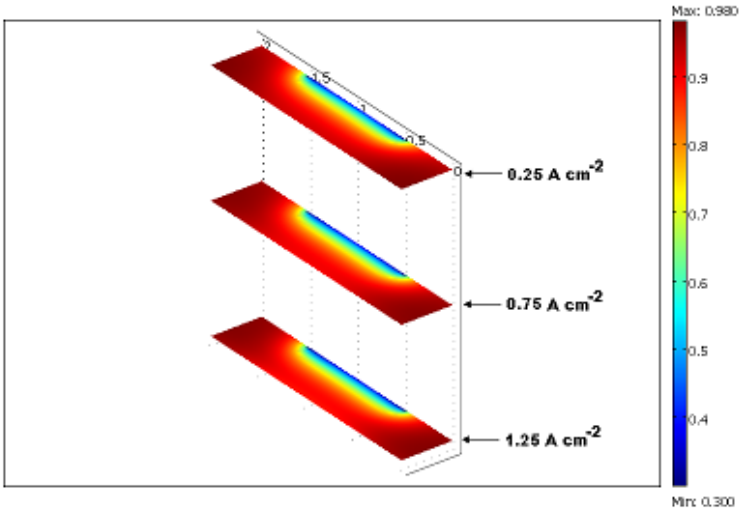


(a)

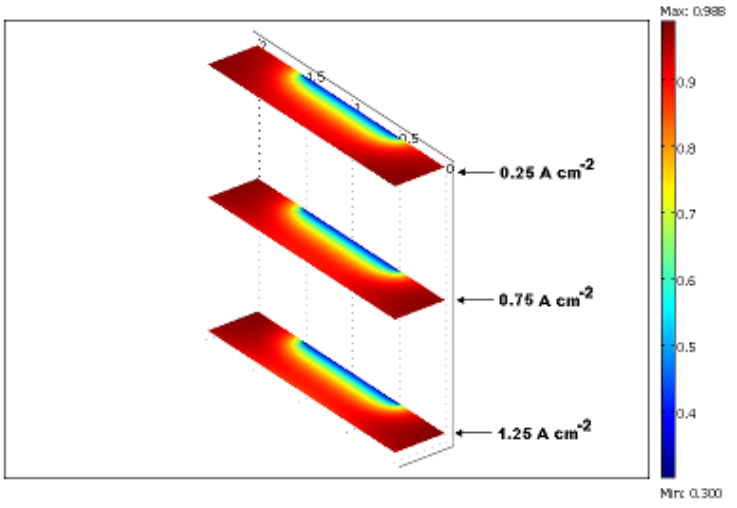


(b)

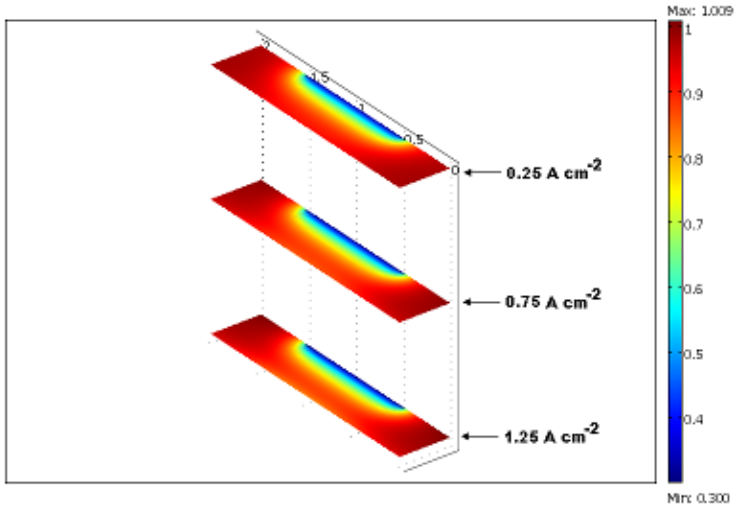


(c)

Figure 5: Relative humidity distribution for RH_in = 30% at three different operating temperatures of: (a) 80°C, (b) 60°C and (c) 40°C.

**Effect of Relative Humidity on Transport Phenomena:**

Figures 6(a-d), show the repetition of simulations with an increased value of relative humidity i.e. RH_in = 70%. Figure 6(a) shows the liquid saturation distribution within the porous cathode. Comparing with Figure 2(a), in which the inlet relative humidity was considered as RH_in = 30%, Figure 6(a) shows a slightly higher levels of liquid saturation. This increase in liquid saturation is due to the addition of more water vapors, which prevents membrane drying. It should be noted that adding more water vapors in the cathode feed improves the heat pipe effect and subsequently more condensation could take place, giving higher overall liquid saturation values.

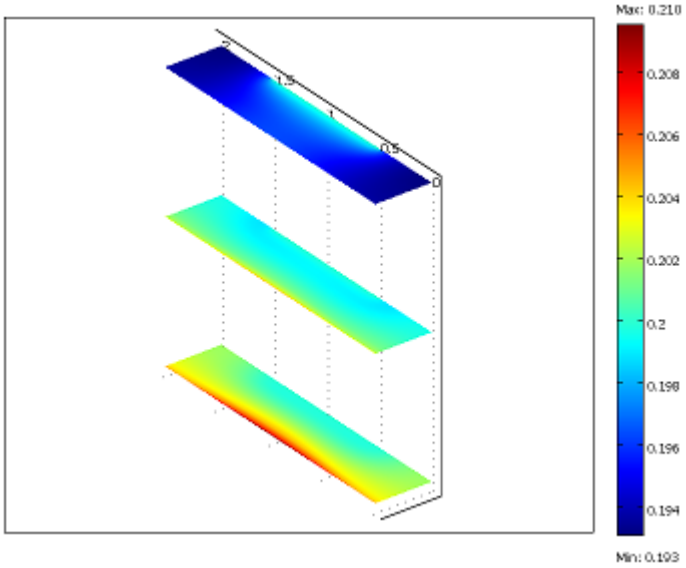


Figure 6(a): Distribution of liquid saturation for RH_in = 70% at an operating temperature of 80°C.

Figure 6(b) shows the oxygen distribution inside the porous cathode for an increased value of inlet relative humidity, i.e. RH_in = 70%. In comparison with Figure 3(a), Figure 6(b) shows a reduced value of oxygen mass fraction at the inlet.

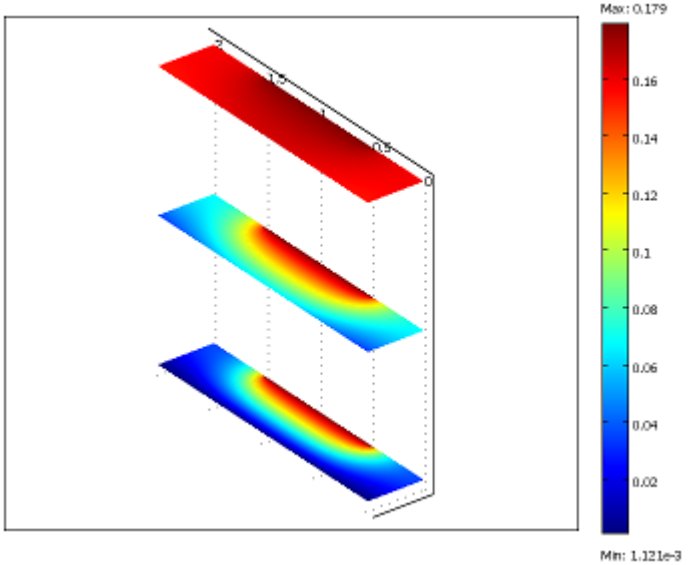


Figure 6(b): Distribution of oxygen mass fraction for RH_in = 70% at an operating temperature of 80°C.

As explained earlier that the addition of water vapors reduces the oxygen mass fraction. At a same operating current density, a lower inlet mass fraction of oxygen will result in more depletion of oxygen.

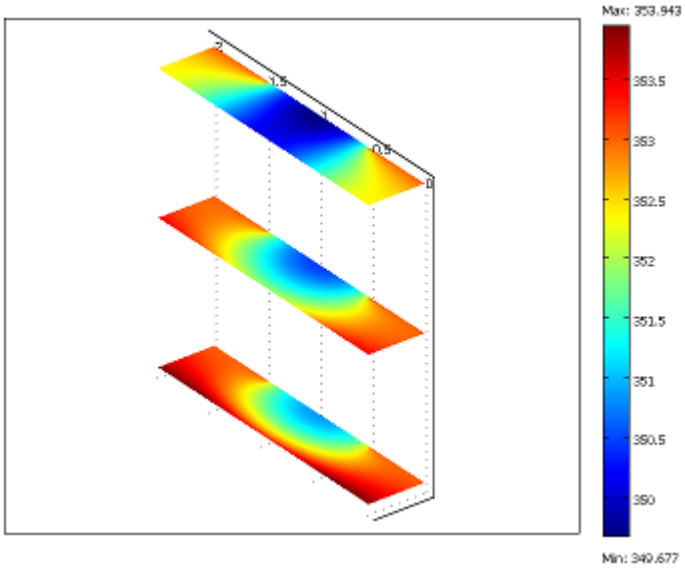


Figure 6(c): Distribution of local temperature for RH_in = 70% at an operating temperature of 80°C.

Figure 6(c) shows the temperature distribution within the porous cathode for an inlet relative humidity of 70%. As can be seen, increasing the inlet relative humidity results in less evaporative cooling of the porous medium as compared to what has been observed in Figure 4(a). By feeding more under-humidified reactants, and maintaining the operating temperature to 80°C, would immediately face an evaporative cooling as soon it enters the cell. The extent of under-cooling diminishes when higher inlet relative humidity feeds are used.

Figure 6(d) show the relative humidity distribution for the case when the inlet relative humidity, RH_in is 70%. As can be seen, the overall relative humidity is slightly higher than what has been observed in Figure 5(a).

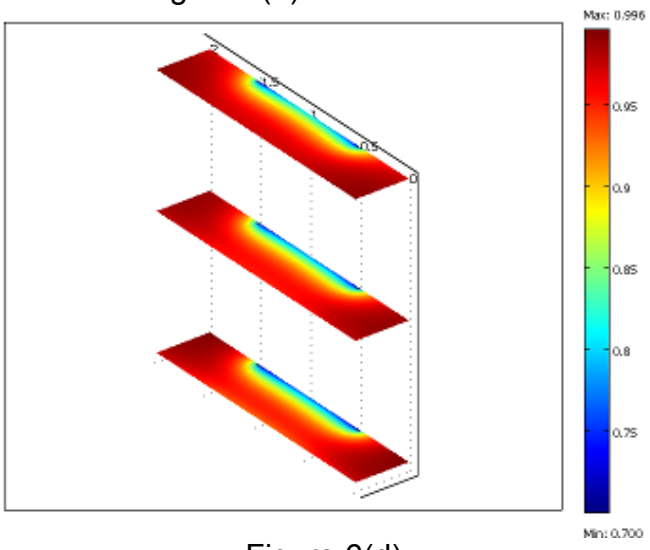


Figure 6(d)

Figure 6(d): Distribution of relative humidity for RH_in = 70% at an operating temperature of 80°C.

This relatively higher humidity value is due to the presence of more water vapors in a better humidified gas feed.

**Effect of Oxygen Flow Rate on Transport Phenomena:**

The oxygen flow rate was doubled in order to see its effect on transport properties within the porous medium. Figure 7(a) shows the liquid saturation distribution and has been compared with Figure 2(a). Increasing the inlet flow rate of oxygen improves the liquid saturation inside the porous medium. This trend is obvious, as higher flow rate of oxygen will improve the reaction rate via forced convection inside the porous electrode, thereby, enhancing the electrochemical production of liquid water.

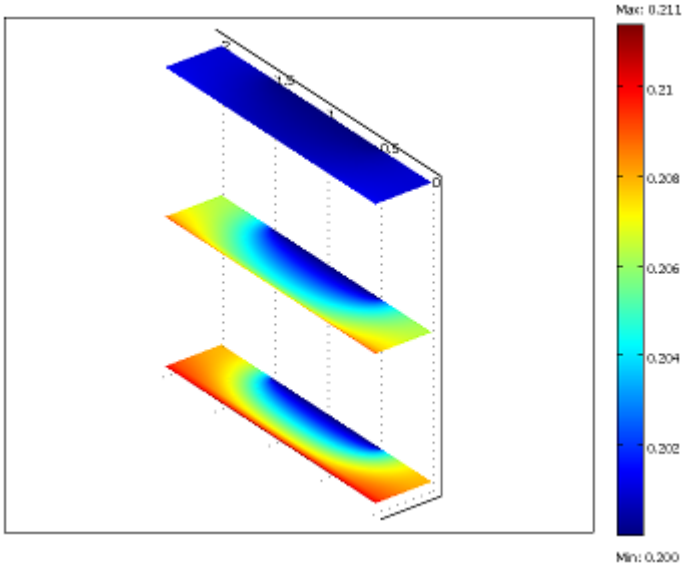


Figure 7(a): Distribution of liquid saturation for RH_in = 30% and T = 80°C with doubling the oxygen flow rate.

Figure 7(b) shows the oxygen mass fraction distribution for the case when the oxygen flow rate was doubled. As can be seen, the inlet mass fraction of oxygen remains unchanged.

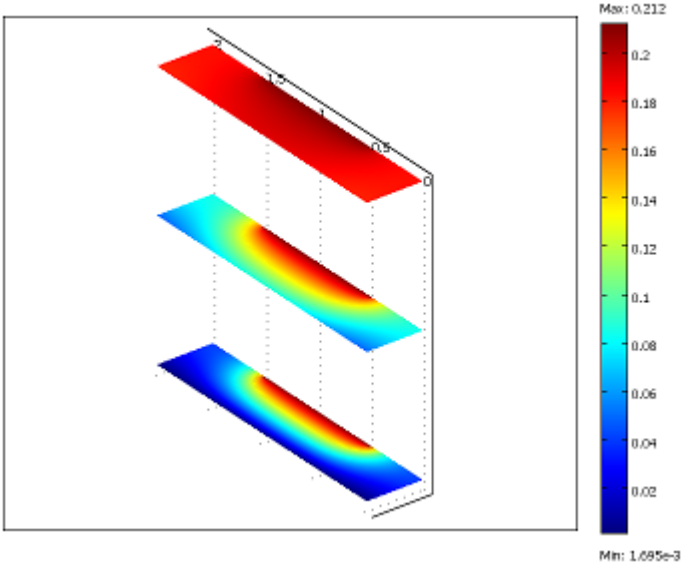


Figure 7(b): Distribution of oxygen mass fraction for RH_in = 30% and T = 80°C with doubling the oxygen flow rate.

However, a slightly lower utilization of oxygen has been observed in this case as compared with Figure 3(a). This is due to less residence time for the reaction with higher flow rates. Higher flow rates offer enough oxygen for the electrochemical reaction; therefore, avoid oxygen starvation inside the catalyst layer.

Figure 7(c) shows the temperature distribution for the case when the oxygen flow rate was doubled. As can be seen, doubling the oxygen flow rate shows a slight increase in temperature as compared to Figure 4(a). The increase in temperature, although minimal, is due to enhanced reaction rate at higher flow rate.

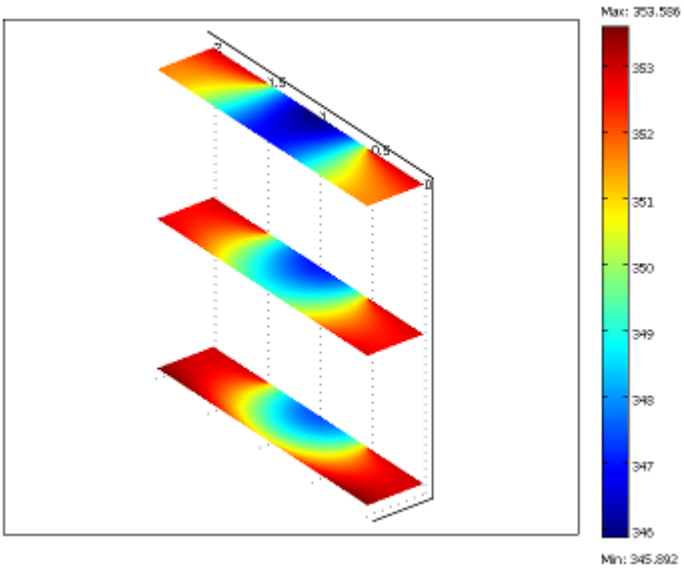


Figure 7(c): Distribution of local temperature for RH_in = 30% and T = 80°C with doubling the oxygen flow rate.

Figure 7(d) shows the relative humidity distribution for the case when the oxygen flow rate was doubled. As can be seen, the relative humidity is slightly reduced with increase in oxygen flow rate as compared to Figure 5(a). This reduction in the value of relative humidity is due to an increase in temperature as discussed above.

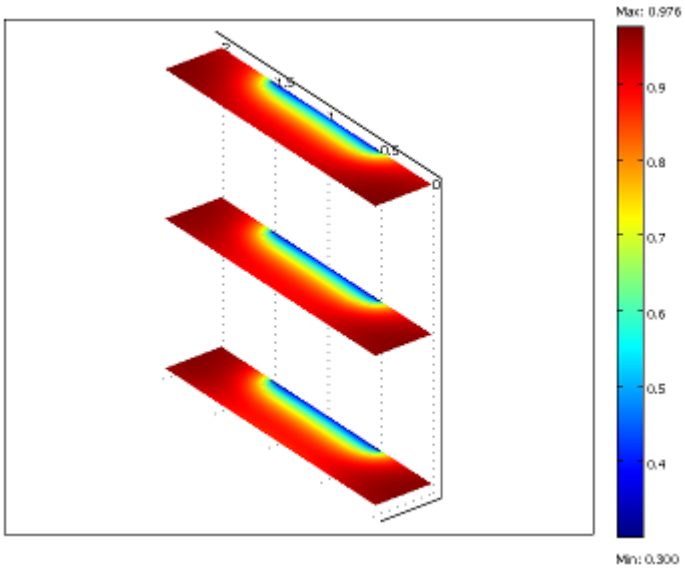


Figure 7(d): Distribution of relative humidity for RH_in = 30% and T = 80°C with doubling the oxygen flow rate.

## Conclusions

A two-dimensional half-cell model of a proton exchange membrane fuel cell has been developed. The model geometry consists of a gas-diffusion layer, a micro-porous layer and a catalyst layer. The model results show that feeding with under-humidified oxygen, the evaporation is taking place at lower current densities. This evaporation is reduced, with increase in current density because of water production via electrochemical route. With an increase in temperature, the electrochemical water production is again offset by increased vaporization rate, thereby, lowering the overall liquid saturation. Increasing the relative humidity is effective in improving the liquid saturation, however, the inlet oxygen mass fraction decreases due to more water vapors in the gas feed. Doubling the oxygen flow rate, increases the liquid water saturation, due to enhanced forced convection through the porous electrodes. However, the relative humidity is slightly reduced due to increased temperature because of higher flow rates. It is concluded that the predicting liquid saturation inside the cathode is a highly complex phenomenon that is interlinked with many variables, such as, local temperature, relative humidity, current density etc.

## References

[1] Mathias MF, Roth J, Fleming J, Lehnert W. Handbook of fuel cells, fundamentals, technology and applications. John Wiley & Sons, New York, 2003, vol. 3, pp.517-37.
[2] Sopian K, Daud WRW. Challenges and future developments in proton exchange membrane fuel cells. Renewable Energy 2006;31:719-27.
[3] Dalasm NKH, Fushinobu K. Phase change in the cathode side of a PEM fuel cell. J Power Sources 2010;195:7003-10.
[4] Akhtar N, Kerkhof PJAM. Effect of channel and rib width on transport phenomena within the cathode of a proton exchange membrane fuel cell. Int. J Hydrogen Energy doi:10.1016/j.ijhydene.2011.02.039.
[5] Liu J, Oshima N, Kurihara E, Saha LK. Transport phenomena within the porous cathode for a proton exchange membrane fuel cell. J Power Sources 2010;195:6342-48.
[6] Meng H. Numerical investigation of transient responses of a PEM fuel cell using a two-phase non-isothermal mixed-domain model. J Power Sources 2007;171:738-46.
[7] You L, Liu H. A two-phase flow and transport model for PEM fuel cells. J Power Sources 2006;155:219-30.
[8] Jung CY, Park CH, Lee YM, Kim WJ, Yi SC. Numerical analysis of catalyst agglomerates and liquid water transport in proton exchange membrane fuel cells. Int J Hydrogen Energy doi:10.1016/j.ijhydene.2010.05.035.
[9] Meng H. Numerical studies of liquid water behaviors in PEM fuel cell cathode considering transport across different porous layers. Int. J Hydrogen Energy 2010;35:5569-79.

A1304

# Aging mechanisms in Lithium-Ion-Battery and PEM-Fuel Cell and their influence on Hybrid-Systems

**Frieder Herb, Kavin Trivedi, Martin Wöhr and Stefan Reiff**
Daimler AG.
GR/AFS - Fuel Cell Power train System
HPC NAB
D-73230 Kirchheim/Teck
Tel.: +49-7021-89-2832
frieder.herb@daimler.com

## Abstract

As the dependency on the non-renewable energy sources are increased and the environmental concerns are illuminated, research on zero emission energy source PEM fuel cell has been intensified. One of the main hurdle to commercialize PEM fuel cell as a main energy source in automobile application is the degradation (aging) of the fuel cell. To accomplish the customer wishes, battery as a secondary energy source in automobile have been used. The aging (degradation) mechanism and aging failures of lithium-ion battery and PEM fuel cell have been investigated and stress factors have been identified focusing on specific aging test. Modeling and validation of aging mechanisms have been illustrated. Moreover, the hybridization phenomenon has been described and the effect of hybridization on aging of lithium ion battery and PEM fuel cell has been illuminated.

## Introduction

Increasing in energy demand, in the use of transportation, population growth, and awareness in climate change are driving demand for green energy sources. Daimler AG is working on several alternative power technologies such as optimized combustion vehicles, hybrid vehicles, battery vehicles and fuel cell vehicles. However the fuel cell provides one of the best and long term solutions to achieve global climate change targets and reduce the dependency on fossil fuel.The fuel cell as one of the zero emission power source have advantages to meet the extended power range and fast refueling desired by customer. On the other hand there are several problems need to be solved before the commercialization of a fuel cell powered vehicle. One of the main research topics is the degradation of PEM fuel cell. To accomplish customer's demands battery as a secondary power source has been used in a fuel cell powered vehicle as shown in Figure 1.

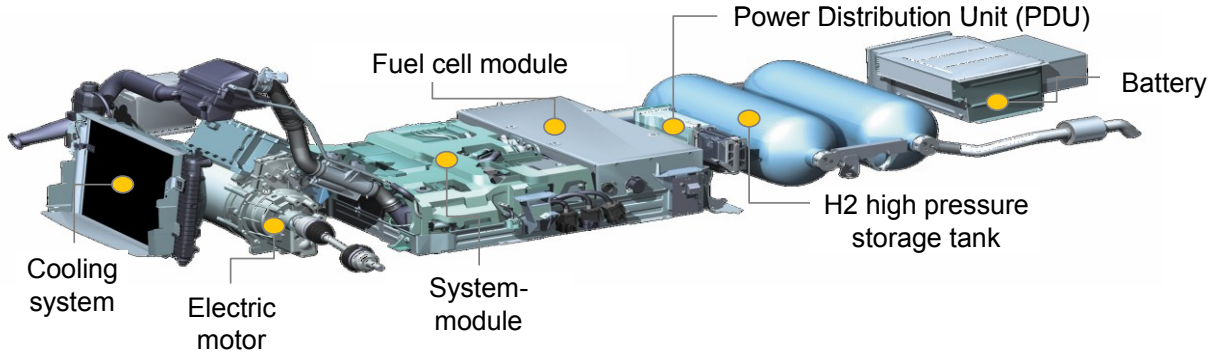


Figure 1: Power train of a fuel cell powered vehicle [10]

The power train of the fuel cell car consists of fuel cell stack as primary energy source, battery as a secondary energy source, power distribution unit which distribute the power between fuel cell stack and a battery and traction motor (electric motor) which runs on a power provided from battery and a fuel cell. High pressure hydrogen storage tank stores hydrogen at 700 bar pressure. Cooling system is responsible to maintain the temperature in fuel cell module, which consists of fuel cell stack and system component (Auxiliary components) like air compressor, humidifier etc. The life time of the power train depends mainly on the life time of fuel cell stack and battery.

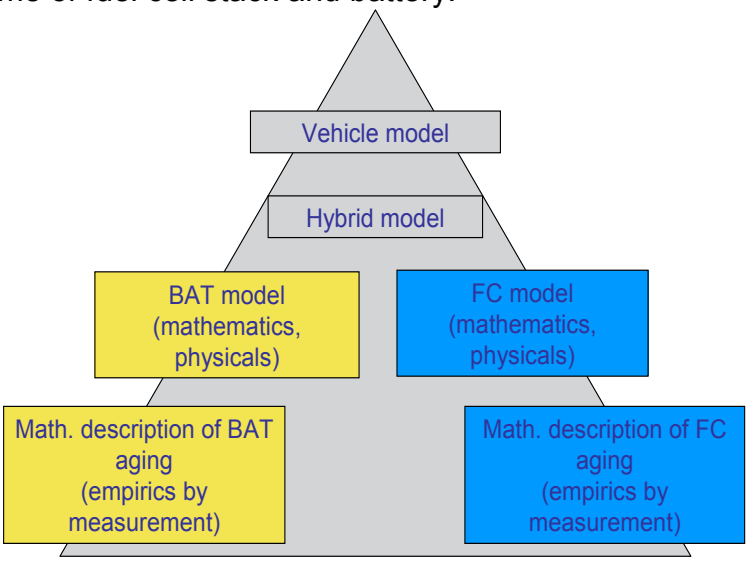


Figure 2: Structure of simulation models [6]

The Figure 2 describes about the structure of the PhD work of Frieder Herb. The goal of the work is to describe aging mechanism of Li-ion battery and PEM fuel cell and investigate the influence of hybridization on their aging. To achieve the desire, mathematical description of the aging mechanism of battery and fuel cell have been developed and implemented in to battery and fuel cell model respectively. The mathematical descriptions of the aging mechanism have been derived by comparing empirical measurement with the stress factors (parameters, that influence aging) of fuel cell and battery. The assumption on the aging mechanism is that the stress factors such as temperature or battery charge are independent of each other and can be linearly extrapolated. Only at fuel cell the effect of single stress factor on the other stress factors have been identified and elaborated. The hybrid model has been developed and effects of hybridization strategy on aging of fuel cell and battery have been investigated. The optimized hybrid model needs to be implemented in to vehicle model and investigate the effect of aging on battery and fuel cell in a real environment.

The description of the mathematical modeling of aging mechanism for Li-ion battery and PEM fuel cell can be found in section 'modeling approach'. Experimental results and validation of the developed models can be found in section 'simulation and validation'.

To develop a mathematical model of aging mechanism, it is very important to identify the main sources (stress factors) of aging problems in Li-ion battery and in PEM fuel cell. This is only possible when have an idea about aging problems in a battery and a fuel cell. The aging phenomenon of the LI-ion battery has been described as follows.

**Introduction of aging mechanism of the lithium ion battery:**

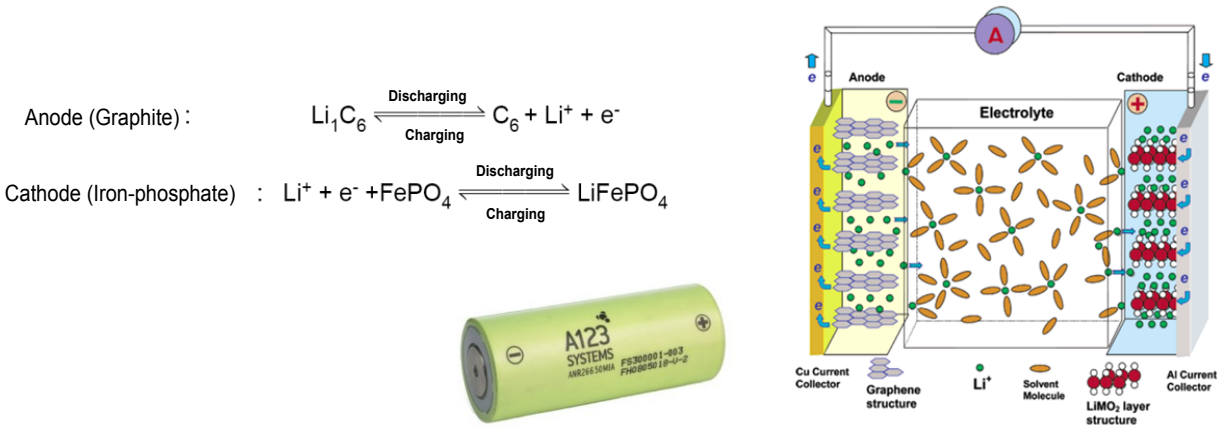


Figure 3 Li-$FePO_4$ Lithium Ion Battery [3]

The aging mechanism of Li-$FePO_4$ Lithium ion battery has been studied. Physically, Lithium ion battery consists of anode (negative electrode), cathode (positive electrode), electrolyte and a separator as shown in a Figure 3. "Both the anode and cathode are material into which, and from which lithium can migrate" [7]. During the discharging, lithium is extracted from anode in to the solvent, separator separates electron from lithium and allow lithium ion to move through the electrolyte, lithium ion moves through the electrolyte to the cathode where it meets with the electron coming through the external circuit from anode to cathode and deposited as Lithium in a cathode. The charging occurs exactly on a reverse mode as in discharging [11].

Theoretically, each component of Lithium ion battery can be aged. After the empirical and theoretical study on lithium ion battery following components of the battery have been detected, which have direct relationship with the aging of a battery. The details of the aging components and kind of aging problems can be found in the

Table 1

| Component | Numbering | Aging problem |
|---|---|---|
| Negative electrode | AF-1-1 | Changing morphology of anode electrode |
| | AF-1-2 | Reducing anode active electrode surface |
| | AF-1-3 | Anode bonding agent decomposition |
| | AF-1-4 | Irreversible intercalation(Li-accumulation in graphite |
| Positive electrode | AF-2-1 | Changing morphology of cathode electrode |
| | AF-2-2 | Reducing cathode active electrode surface |
| | AF-2-3 | Cathode bonding agent decomposition |
| Electrolyte | AF-3-1 | Conducting salt decomposition |
| | AF-3-2 | Electrolyte contamination |
| SEI-coating | AF-4-1 | Cathode electrolyte layer washed out |
| Current collector | AF-5-1 | Anode metal corrosion |
| Separator | AF-6-1 | Separator abrasion |
| | AF-6-2 | Decrease of porosity |

Table 1 Aging problems in a Lithium Ion battery [6]

In a battery different components have different kinds of aging problems for an example negative electrode has an aging problem such as morphology changing of anode electrode (graphite).The graphite exfoliation or break are more examples caused by a mechanical stress such as acceleration or temperature cycles, as well as dilation of lithium ion with surrounding solvent [11] and [12] . The charging and discharging also play a negotiable role. The stress factors for above mentioned aging problems have been analyzed. From 19 such a stress factors, four most influenced stress factors such as temperature, depth of discharge (DOD), state of charge (SOC) and current dynamic have been investigated to model an aging mechanism of the Li-ion battery.

**Introduction of aging mechanism of the PEM fuel cell:**

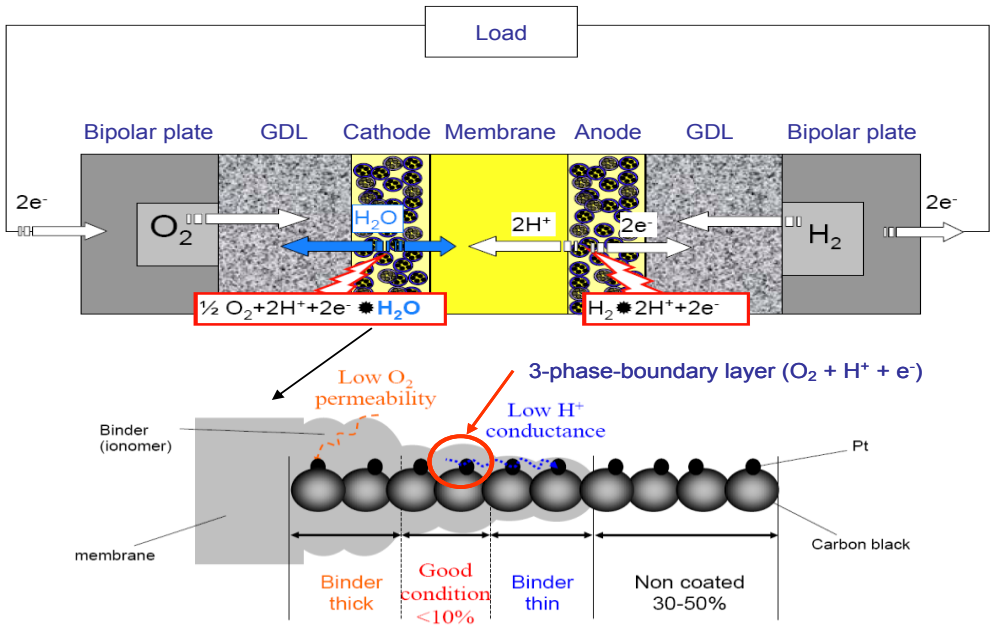


Figure 4 PEM Fuel cell [2]

Physically, PEM fuel cell consists of membrane electrode assembly (MEA). Anode (negative electrode), cathode (positive electrode) and electrolyte forms MEA. MEA, gas diffusion layer (GDL) and catalyst sandwiched between two flow field plates (bipolar plates). Hydrogen from the storage tank has been supplied through the bipolar plate to anode. Gas diffusion layer diffuse the hydrogen and separate the electron from hydrogen. The hydrogen ion is drawn through the electrolyte from anode to cathode by the reactive attraction of hydrogen to oxygen, while the electrons are forced through an external circuit. At cathode the hydrogen ions regain electron (coming from external circuits) and form hydrogen. The hydrogen reacts with oxygen at a cathode and form water at cathode. Reactions at anode and cathode have been illustrated in Equation 3

$$\text{Anode}: H_2 \rightarrow 2H^+ + 2e$$

$$\text{Cathode}: \frac{1}{2}O_2 + 2H^+ + 2e \rightarrow H_2O$$

**Equation 3**

Theoretically, each component of the PEM fuel cell can also be aged. The aging problems consist in each component of the PEM fuel cell have been illustrated in
Table 2

| Component | Numbering | Aging problem |
|---|---|---|
| Membrane | AF-1-1 | Membrane hole formation |
| | AF-1-2 | Membrane conductivity reducing |
| | AF-1-3 | Platinum delaminating |
| | AF-1-4 | Membrane humidity reducing |
| Catalyst coating | AF-2-1 | Catalyst collector decomposition |
| | AF-2-2 | Catalyst fracture |
| | AF-2-3 | Reducing conductivity of catalyst collector |
| | AF-2-4 | Air starvation |
| | AF-2-5 | Platinum decomposition |
| | AF-2-7 | Platinum particle clustering |
| | AF-2-8 | Platinum particle deactivation |
| Bipolar plate | AF-3-1 | Bipolar plate corrosion |
| | AF-3-2 | Contact resistance increases |
| GDL | AF-4-1 | PTFE- erosion |
| | AF-4-2 | GDL-fracture |
| | AF-4-3 | GDL- corrosion |
| Seal | AF-5-1 | Leakage failure |
| | AF-5-2 | End plate oxidisation |

Table 2 Aging problems in a PEM fuel cell [6]

In PEM fuel cell different components have different kind of aging problems. For an example component membrane have an aging problem such as hole formation in a membrane. Vibration, high temperature, lower pressure and lower humidity can accelerate the hole formation in a membrane [5]. The consequences of hole formation is that the electron will pass through the membrane which reduces the electron flow through external circuit, which eventually reduces power generation from the fuel cell. That is why the stress factors such as vibration, high temperature, lower pressure and lower humidity are responsible for aging problem like hole formation. In this way for all aging problems illustrated in a
Table 2, total 27 different stress factors have been determined. After the empirical and literature study, four most influenced stress factors such as stack inlet temperature, current dynamic, cathode humidity and idle current (max. voltage) have been investigated to model the mathematical function of aging mechanism in PEM fuel cell.

## Introduction of the hybridization control strategy

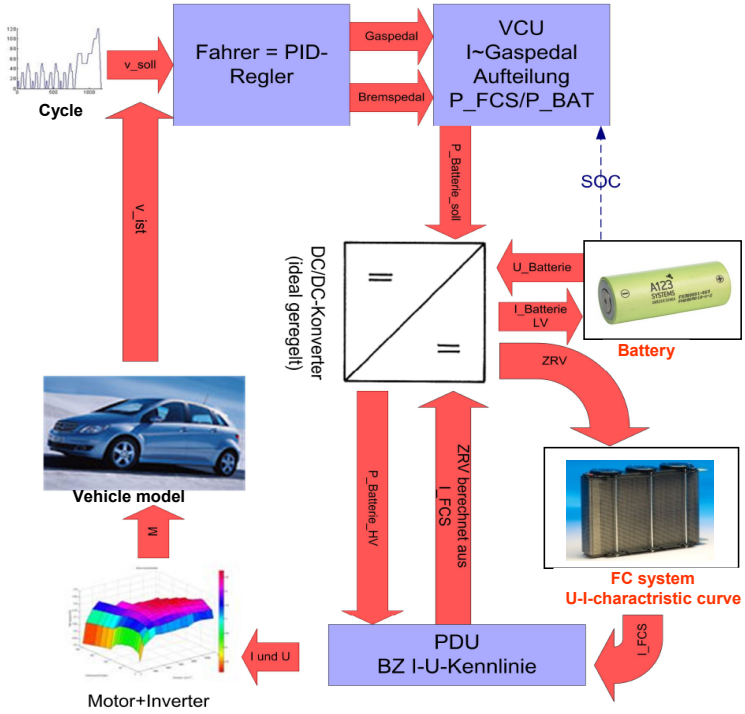


Figure 5 hybridization in a fuel cell vehicle[1]

If a vehicle uses more than one energy source to power a vehicle then its power train is called a hybrid power train. In a fuel cell powered automobile, two energy sources fuel cell stack (primary energy source) and battery (secondary energy source) have been used. The aim of both energy sources is to fulfil the required power from the electric motor. The control strategy decides about from which energy source the required power will be delivered. For an example as illustrated in a
Figure 5 the vehicle control unit (VCU) get the required power from the driver and state of charge (soc) of a battery as inputs and gives the controlled output as power required from battery and the rest of the power will be drawn from fuel cell to fulfil total required power from the driver. The aim of the work is to analyse the influence of different control strategy on aging of PEM fuel cell and Lithium ion battery.

# 1. Modeling Approach

In this chapter the mathematical modeling of the aging mechanism in Lithium ion battery and in PEM fuel cell have been described.

## Mathematical aging model of the lithium ion battery

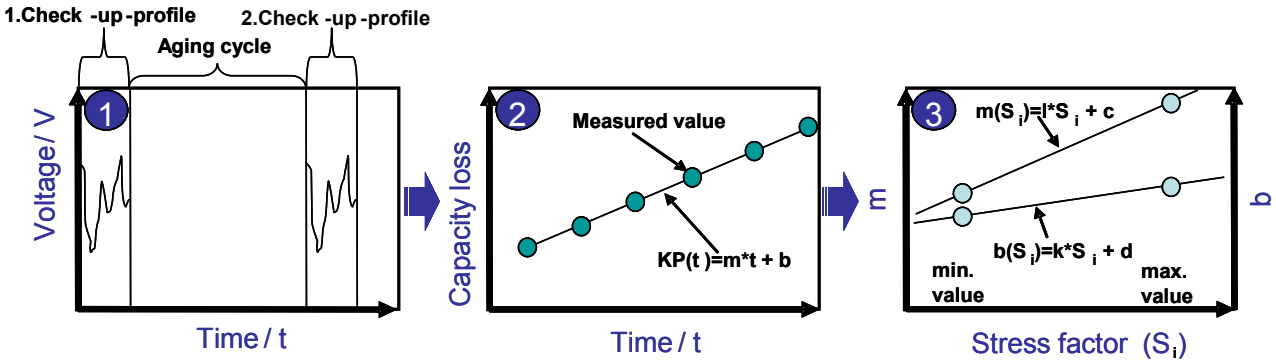


Figure 6 Determination of an aging model [6]

The determination of an aging model of the Li-ion battery has been achieved in a three steps as shown in Figure 6. In a first step determine the component parameters through time dependent cell voltage cycle. In a battery the component parameters are capacitance, inner resistance and time constant. Between the two check ups profile of the cell voltage, the battery with different stress factors has been aged. In a second step analyze the changing of the component parameter over time for each stress factor. The parameters changing have been approximated by a suitable mathematical function. The approximation is a numerical optimization procedure for solving linear programming problems, the simplex method carried out which will work in a finite number of iterations of the global minimum of objective function [9].As shown in the Figure 7 (second step) for different test matrix (p08, p10, p11) the graph of relative capacity loss(component parameter) over the cycle time has been plotted and with approximation method the mathematical functions of each test matrix (in a blue line) have been found. The mathematical function of the test matrix is

$$\text{Relative capacity loss } C_{V,DOD}(Z,\Delta DOD) = \alpha_3 * (DOD) * \exp(\alpha_4 (DOD) * Z)$$

**Equation 4**

In the third step the obtained parameters of the mathematical functions can be plotted over stress parameters, determine the function again with a simplex method. As shown in the Figure 7 (Third step) the parameters found in a mathematical function in a second steps ($\alpha_3$ and $\alpha_4$) have been plotted over different stress factors and approximated by mathematical function (in a blue line). The mathematical function of the parameter is

$$\alpha_3(\Delta DOD) = \alpha_{DOD,1} * \ln(\Delta DOD) + \alpha_{DOD,2}$$

**Equation 5**

$$\alpha_4(\Delta DOD) = \alpha_{DOD,3} * (\Delta DOD) + \alpha_{DOD,4}$$

**Equation 6**

By applying Equation 5 and Equation 6 in Equation 4

$$C_{V,DOD}(Z, \Delta DOD) = \alpha_{DOD,1} * \ln(\Delta n(\Delta D + \alpha_{DOD,2} * \exp((\alpha_{DOD,3} * (\Delta\Delta DOD + \alpha_{DOD,4}) * Z)$$

In this way for every stress factors of the battery mathematical function can be found. It can be concluded that with mathematical equation any kind of intermediate curve can be found.

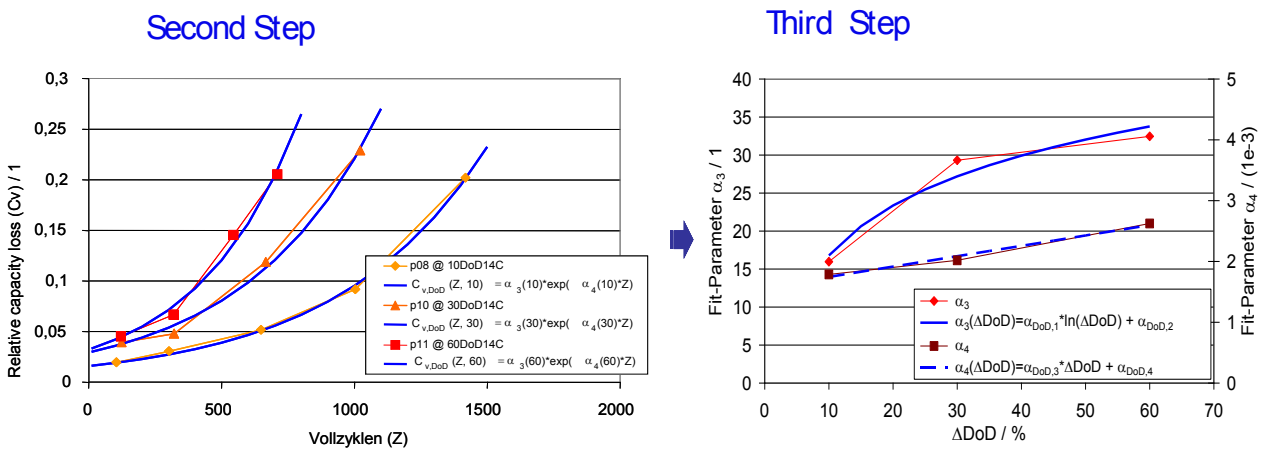


Figure 7 Examples of determination of aging model [6]

The mathematical function of the stress factors can be integrated in to the aging model as shown in Figure 8.

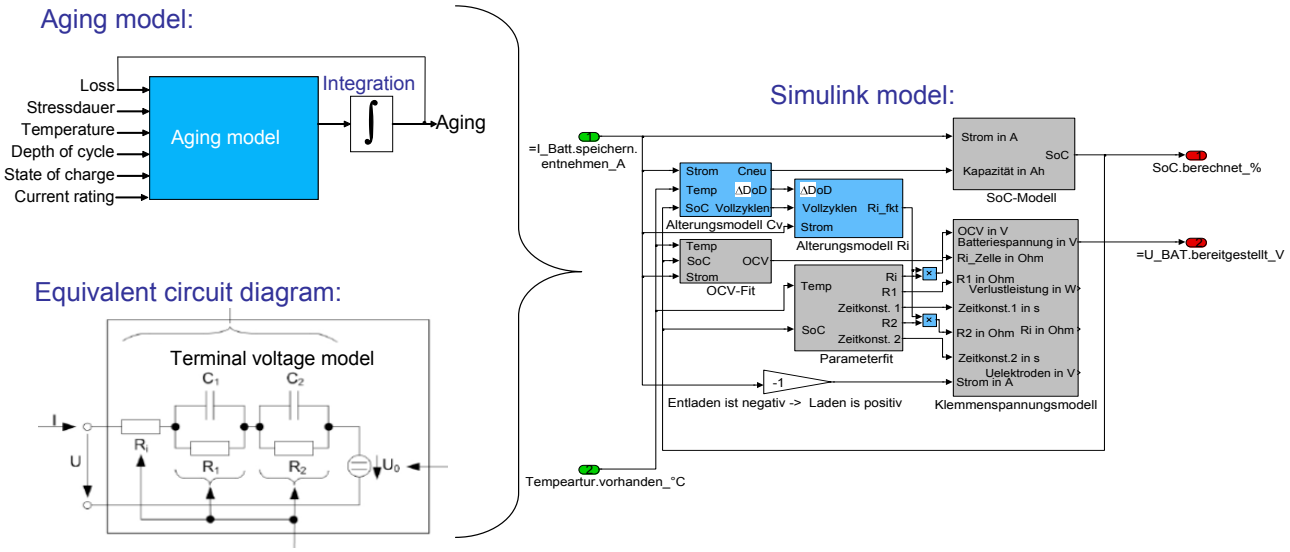


Figure 8 Aging model of Lithium Ion Battery [6], [12]

In the Simulink model inputs are (in green) the current and temperature, while the outputs are (in red) state of charge and voltage of the battery. The light blue are the aging model and gray are the battery model. Inputs of the aging model are loss, stress duration,

temperature, depth of charge, state of charge and current rating, while the output is integrated and feed back as a loss in the input of the aging model. The combination of aging model and equivalent circuit diagram is the Simulink model.

## Mathematical aging model of the PEM fuel cell

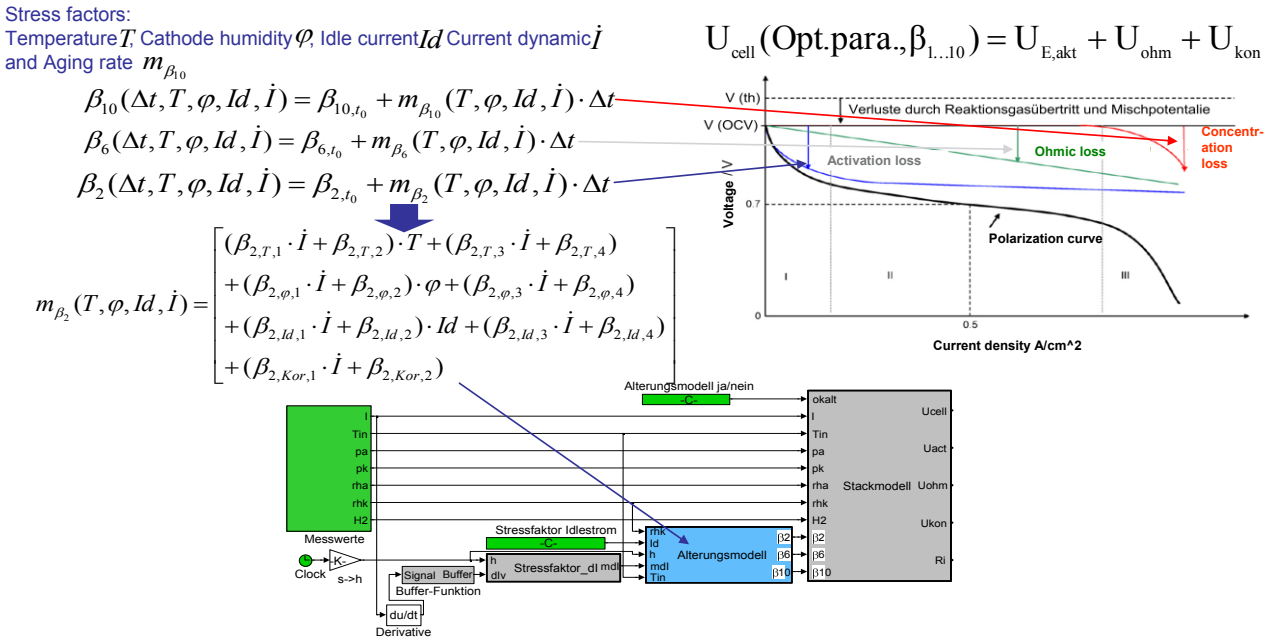


Figure 9 Mathematical aging model of PEM fuel cell [6]

The determination process for the aging mechanism of the PEM fuel cell goes also in a similar way as it has been illustrated in

Figure 6. As shown in a Figure 9 total cell voltage of the fuel cell has been divided in to three phase such as activation loss, ohmic loss and concentration loss. The stress factors for aging of PEM fuel cell are Inlet temperature, cathode humidity, idle current and current dynamic. The mathematical model of fuel cell stack consists of 10 parameters $\beta_{1...10}$ but from the literature it has been found that not all 10 parameters influenced the aging of the fuel cell. From Fowler [8] is determined that parameter $\beta_2$ has influence on activation loss, parameter $\beta_6$ has impact on ohmic loss and parameter $\beta_{10}$ is responsible for concentration loss. Aging of a fuel cell can be detected via decreasing of its cell voltage or stack power at a different aging rate. The idea is to determine the aging rate at which the parameters $\beta_2$, $\beta_6$ and $\beta_{10}$ are changing during the operating time of a fuel cell. It means that

The actual value of the parameter at time $t_1$ = value of the parameter at time $t_0$ + aging rate * change of time

$$\beta_2(\Delta t,T,\ ,Id,\dot{I}) = \beta_{2,t_0} + m_{\beta_2}(T,\ ,Id,\dot{I})\quad\Delta t$$

The aging rate $m$ is a function of four stress factors Inlet temperature, cathode humidity, idle current and current dynamic as illustrated in a Figure 9 . In this way at every time step the actual value of the parameter can be determined. As shown in a Figure 9 inputs of the aging model are changing in time, inlet temperature, cathode humidity, Idle current and current dynamic while the outputs of the aging model are the actual values of parameters $\beta_2$, $\beta_6$ and $\beta_{10}$. The aging model gives the actual value of the $\beta_2$, $\beta_6$ and $\beta_{10}$ parameters to the fuel cell stack model.

## 2. Simulation and Validation

The effect of different current and temperature profile on the component parameters of Lithium ion battery and PEM fuel cell, and validation of the aging model have been described in this chapter. Moreover the effects of different hybrid strategy on PEM fuel cell current dynamics and on aging mechanism of lithium ion battery and PEM fuel cell have been illustrated.

### Simulation results of the lithium ion battery

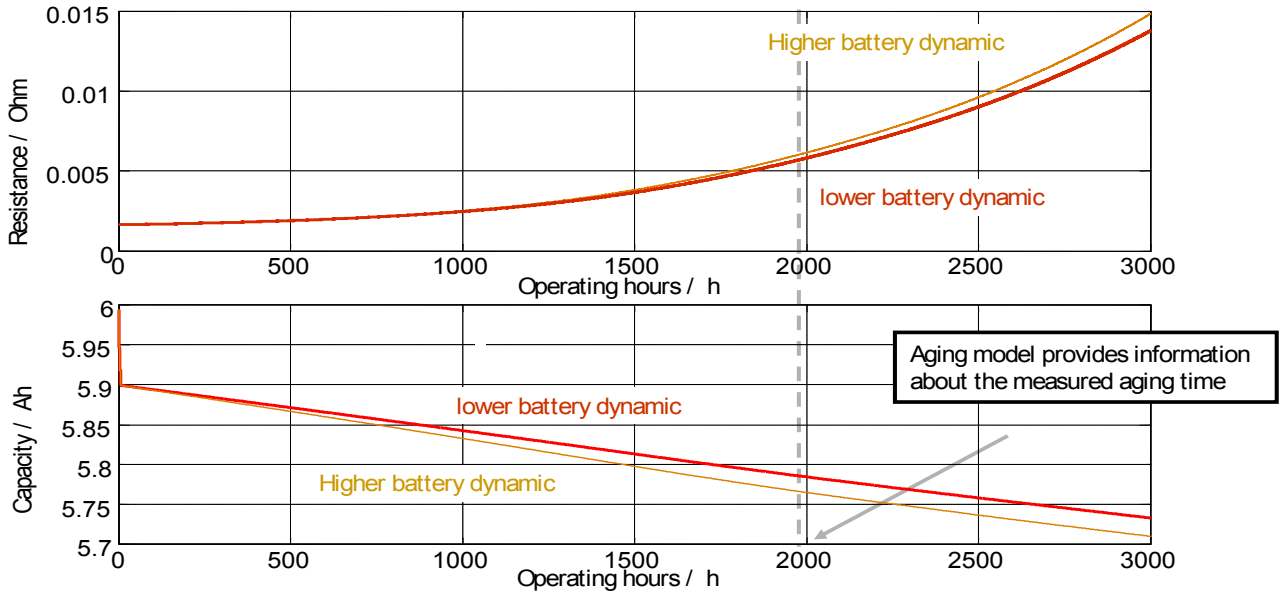


Figure 10 Simulation of aging of Lithium ion battery with different current profile [6]

It can be seen from Figure 10 that current dynamic plays a role in the battery aging mechanism, higher current dynamic increases the resistance around 6.5 times the initial value and lowering the capacity of the battery around 3% at the end of 3000 operating hours.

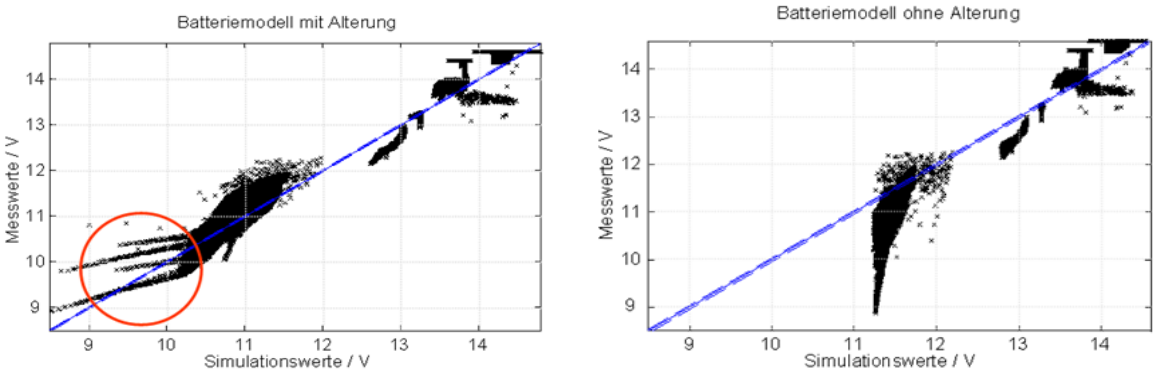


Figure 11 Validation of Lithium ion battery aging model [6]

The improvement in simulation with aging model has been described in the Figure 11. The measured data of a four cell (220 hours at 50°C temperature, 15% DOD, 60%soc and 30C current) has been compared with the simulation data with and without aging model. At a lower voltage range simulation data with aging model fits with the measured data very well. It can be concluded that at a lower voltage range aging model improves the simulation.

**Simulation results of the PEM fuel cell**

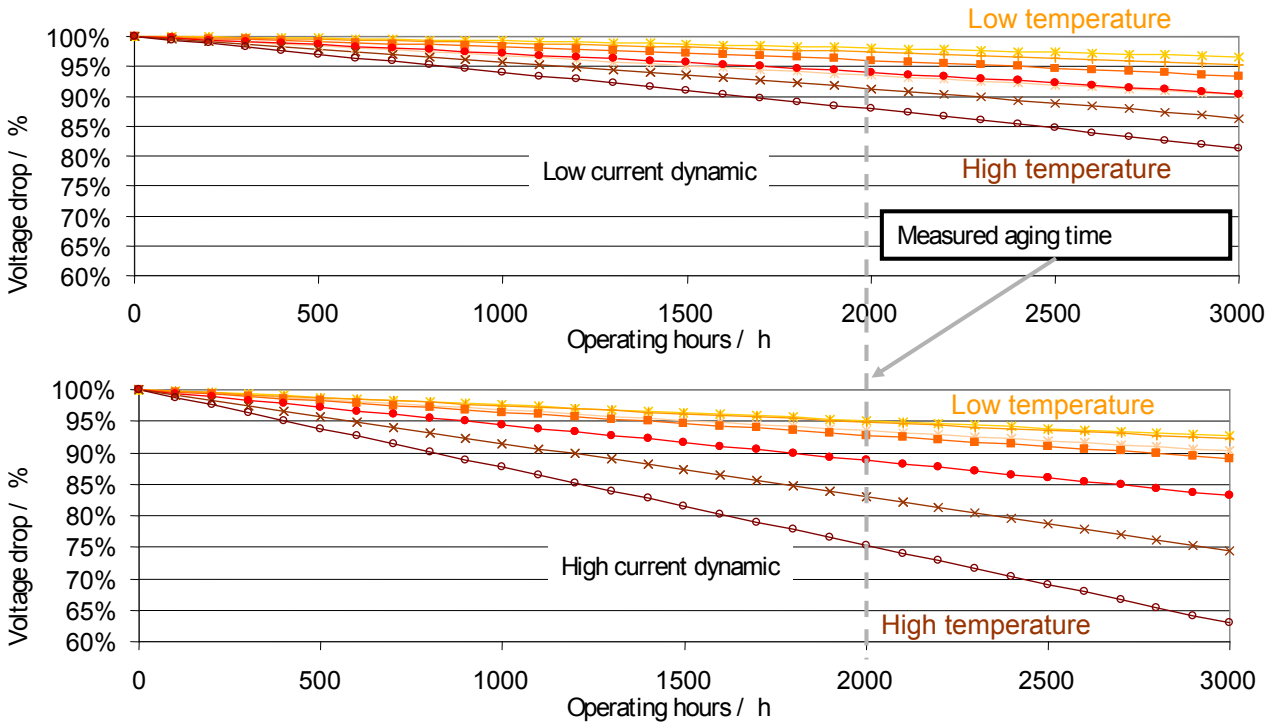


Figure 12 Simulation result of PEM fuel cell aging by different temperature and current cycles [6]

The Figure 12 describes the aging of a PEM fuel cell in terms of voltage drops over operating hours by different current and temperature cycles. It can be seen that current dynamic has a major influence on the aging of a PEM fuel cell. Lower current dynamic and low temperature has a voltage drop around 5% over 3000 operating hours, while low current dynamic and high temperature has maximum voltage drop around 20% over 3000 operating hours. While high current dynamic and low temperature can drop the voltage minimum up to 7% and high current dynamic and high temperature can decrease the voltage maximum up to 40%.It can be seen that the combination of high current dynamics and high temperature cycle accelerate aging in a quick manner.

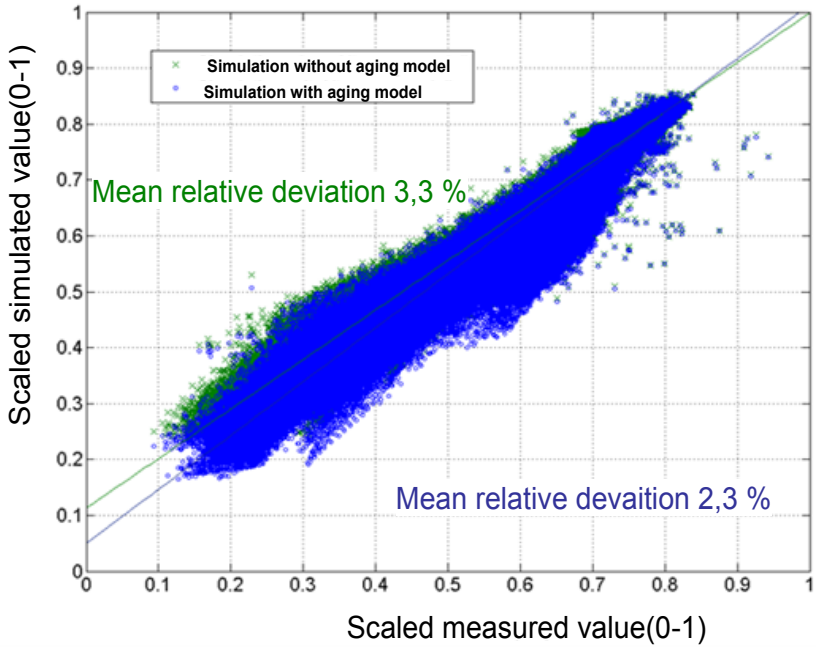


Figure 13 Validation of PEM fuel cell aging model [6]

The Figure 13 describes the graph between measured value and simulated value at high temperature and high current dynamic over 1000 operating hours. The simulated value without aging model have mean relative deviation of 3.3% with the measured value while the simulated value with aging model improves the mean relative deviation by 1%, means simulated value with aging model is closer to the measured value compare to simulated value without aging model. From the above result the aging model of the fuel cell can be validated.

## Hybridization

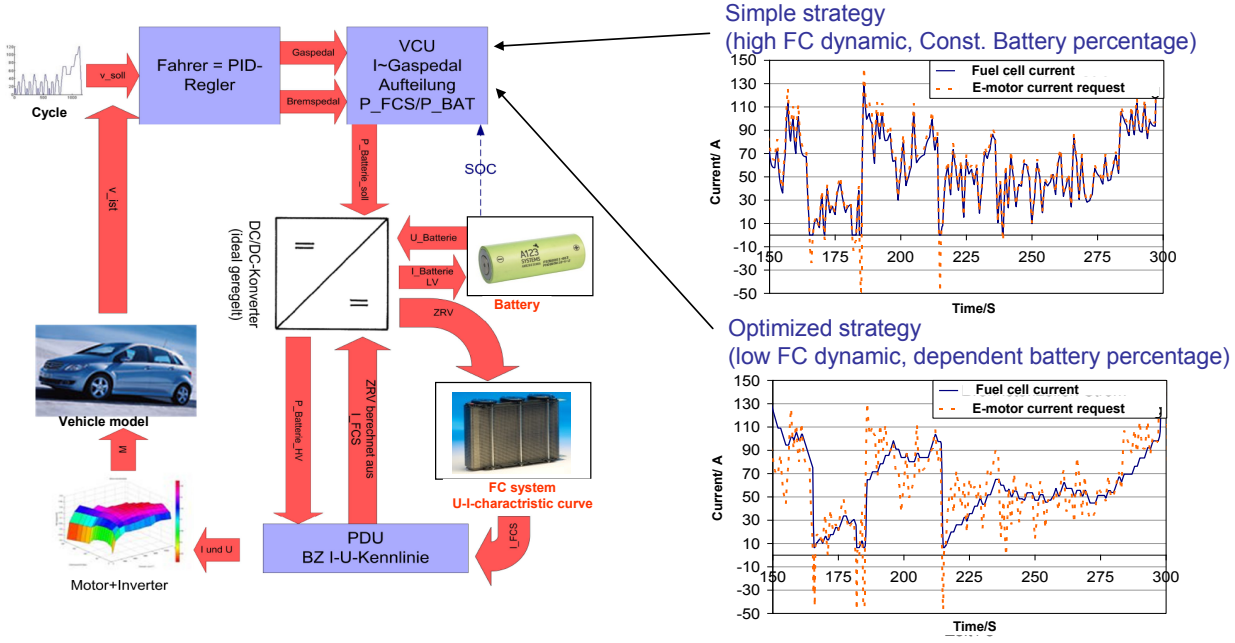


Figure 14 Effect of hybridization on PEM fuel cell current dynamic [1]

The effect of the vehicle control strategy on fuel cell current dynamic has been illustrated in Figure 14. It can be seen that optimized strategy significantly reduces fuel cell current dynamic at same vehicle request as in simple strategy.

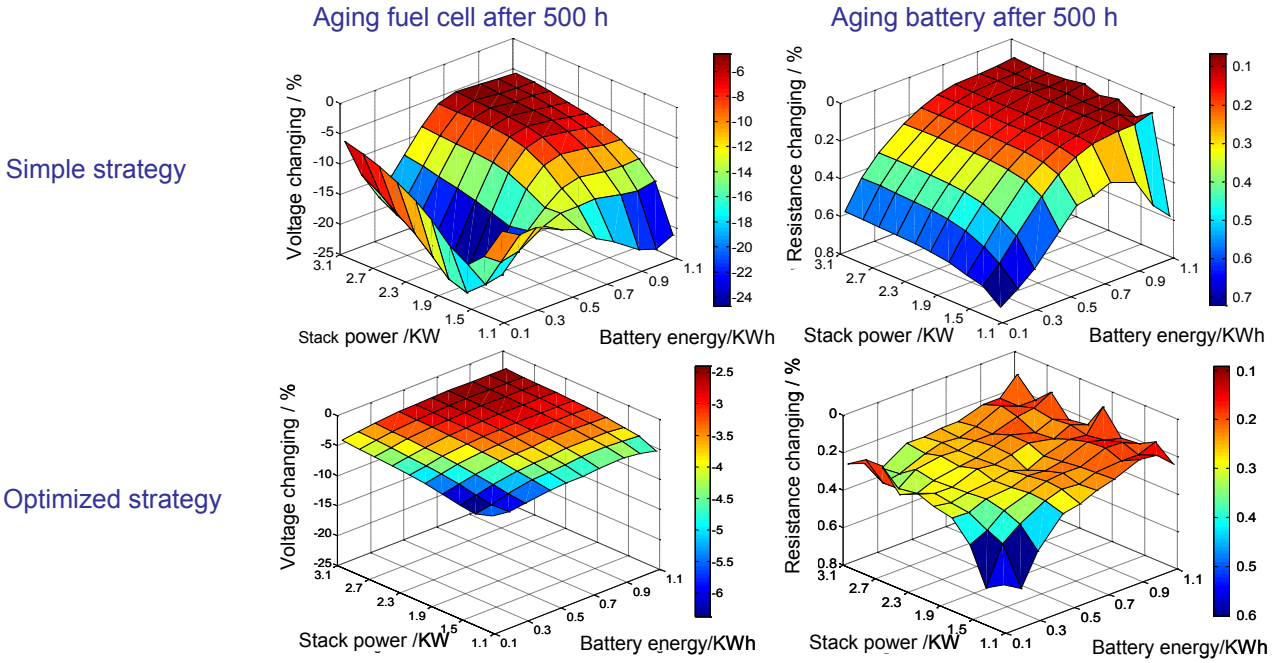


Figure 15: Effect of hybridization on aging of Lithium ion battery and PEM fuel cell [6]

The effect of the control strategy on aging of lithium ion battery and PEM fuel cell has been illustrated in Figure 15 . The aging of the fuel cell and battery have examined over 500 operating hours. The voltage changing regards to stack power and battery energy plotted for fuel cell and resistance changing regards stack power and battery energy plotted for Lithium ion battery. It can be seen that with the control strategy have a great influence on aging rate. Optimised strategy can be used to lower the aging rate both in battery and in fuel cell. It can be judged that optimized strategy allows for smaller fuel cell and battery at a same aging rate.

## 3. Conclusion

Lithium ion battery and PEM fuel cell aging mechanisms have been studied. Aging phenomenon has been described as mathematical equations and the equations have been integrated in a Simulink model and validated. An optimized hybrid strategy improves aging in a PEM fuel cell and Lithium ion Battery.This approach shows that the method to develop mathematical aging model works reliable and with the aging model in a hybrid system, sizing of components (depending on aging requirement) is possible.

## Figures



## Tables

# References


[1]. ACHIM FRANK: Simulation der Dynamikreduzierung einer Brennstoffzelle durch angepasste Batterieregelung. Diplomarbeit, Universität Ulm, Institut für Energie-Wandlung und -speicherung, Ulm, 2007

[2]. Cutting Edge Technologies for PEM Fuel Cells New Evaluation Method for Effectiveness of Platinum/Carbon Electro catalysts under PEFC Operation Conditions, Makoto Uchida, f-cell 2010, Stuttgart 27-28.Sep., 2010

[3]. KANG XU: Nonaqueous Liquid Electrolytes for Lithium-Based Rechargeable Batteries. In: Chemical Reviews, Vol. 104 (2004), Nr. 10, S. 4303-4417

[4]. Jack Sample, Time Response of Solid Oxide Fuel Cell Anodes. Proceedings of the Annual Meeting of the SOFC Society, Kyoto, Japan, July 1999

[5]. S. Besse, et al: General Durability Issues and Requirements Related to back up Power Applications. In: INTERNATIONAL WORKSHOP ON DEGRADATION ISSUES OF FUEL CELLS, Hersonessos,Crete,Greece,2007

[6]. Frieder Herb: Alterungsmechanismen in Li-ion-Batterie und PEM– Brennstoffzellen und deren Einfluss auf die Eigenschaften von daraus bestehenden Hybrid-Systemen. Doktorarbeit, Universität Ulm Mai 2010

[7]. Wikipedia: Lithium ion battery [online]. Internet site http://en.wikipedia.org/wiki/Lithium_ion_battery [13.04.2011]

[8]. Michael W. Fowler, et al.: Incorporation of voltage degradation in to generalised steady state electrochemical model for a PEM fuel cell. In: Journal of Power Sources, Vol.106 (2002), S.274-283.

[9]. Wikipedia: Simplex-Verfahren[online] Internet site: http://de.wikipedia.org/wiki/Simplex-Verfahren [26.12.2008]

[10]. Henning Wallentowitz, Konrad Reif. Hand buch Kraftfahrzeugelektronik, 1.Auflage. Vieweg & Sohn Verlag, GWV fachverlage GmbH, Wiesbaden, September 2006.

[11]. Andreas Jossen, Wolfgang Weydanz: Moderne Akkumulatoren richtige einsetzen. Jossen, Weydanz(Hrsg.) 1. Aufl., Leipheim : Ubooks Verlag, 2006

[12]. Martin Beißwenger: Anpassung eines Funktionsmodells für LiFePO4-Batterien und Ansatz zur Berücksichtigung der kalendarischen und betrieblichen Alterung. Diplomarbeit, Universität Ulm, Institute für Energiewandlung und-speicherung,Ulm,2008

A1305

# Numerical study on the water distribution in GDL and channels of PEMFC applying microchannel bipolar plate

**Bosung Kim[1], Ahyoung Woo[1], Yongtaek Lee[2], and Yongchan Kim[1,*]**
[1]Department of Mechanical Engineering, Korea Univ.
5-ga, Anam-dong, Sungbuk-gu, Seoul 136-716 /KOREA
[2]Department of Mechanical and Mechatronics Engineering, Waterloo Univ.
200 University Ave. W., Waterloo, ON, N2L 3G1, CANADA
*Tel.: +82-2-32903366
Fax: +82-2-9215439
yongckim@korea.ac.kr

## Abstract

Water management is an important factor in the implementation of proton exchange membrane fuel cells (PEMFCs). The ionic conductivity of a membrane is dependent on the properties of membrane and water content. However, excessive water amount causes flooding, which disturbs transport of reactant gases. Many researchers have studied proper water management and methods to prevent flooding. Especially, understanding two-phase flow in porous gas diffusion layer (GDL) is needed to prevent flooding. In this study, the effects of operating conditions on the cell performance and water content were studied by a three-dimensional fuel cell model. In addition, the water removal effect of a microchannel manufactured in the bipolar plate was investigated. The active cell area was 10.2 $cm^2$ and flow fields in anode and cathode were parallel channels. The operating temperature was 50 $^oC$ at atmospheric pressure. Stoichiometries of anode and cathode were 1 and 2, respectively. Water content in GDL increased with an increase in the cell temperature. At high stoichiometry condition, total amount of air decreased due to water removal by excessive air. The humidity of air had significant effect on amount of water. The water removal using the microchannel bipolar plate was more effective than that using the conventional bipolar plate. In addition, the water content in GDL using the microchannel bipolar plate was more evenly distributed.

# Introduction

The proton exchange membrane fuel cells (PEMFCs) are expected to be a candidate for the new power sources. PEMFCs have attractive advantages, such as fast start-up, moderate operating temperature, and compactness. Water management is very important in the performance and reliability of PEMFCs. Water flooding and dehydration are major issues of water management. Flooding and drying may occur due to uneven conditions in the fuel cell.

Water transport phenomena across membrane are well described in [1]. Electrochemical reaction produces water on the cathode side. Water in the anode side is dragged to the cathode by protons moving through the electrolyte. This is called electro-osmotic drag. Water generation and electro-osmotic drag would create a large concentration gradient across the membrane, resulting in water diffusion from the cathode to the anode.

Water generated in the cathode must be transported from the catalyst layer to the outlet of gas flow channels. If the water removal is not sufficient, excess water blocks the pores of gas diffusion layer (GDL) and reduces active area of cathode catalyst layer. This phenomenon is called flooding. Water flooding will cause a reduction in the performance and reliability of PEMFC.

The water distribution and flooding in PEMFCs have been investigated extensively. Dawes et al. [2] analyzed the effects of water flooding on the performance of PEMFCs. A three dimensional model was developed to predict the effects of operating conditions, such as operating pressure, temperature, relative humidity of the reactant gases, and stoichiometry of air and hydrogen. These operating conditions interactively affect the water balance in the fuel cell and ultimately the cell performance. Sun et al. [3] developed a model to measure pressure distribution and flow cross over through the GDL in PEMFC flow channel.

Visualization and pressure drop measurement have been conducted to investigate water flooding qualitatively. Gao et al. [4] analyzed water flow pattern in GDL. Pore scale visualization was performed to investigate two-phase flow in different types of GDL. Lu et al. [5] investigated two-phase flow in cathode channels in various air stoichiometries and superficial water velocities. Park et al. [6] measured the cell performance based on the effect of liquid water accumulation by neutron radiography.

Efforts to reduce water flooding include the addition of micro porous layer (MPL) in the MEA, GDL treatment with PTFE, and the modified flow filed design. Jeon et al. [7] studied the effect of serpentine flow field design on water content in PEMFC. Park et al. [8] studied the effect of PTFE treatment and PTFE content of GDLs. Qi et al. [9] experimentally investigated the cell performance with and without MPLs on water flooding.

In this paper, the water distribution in GDL and channels was numerically investigated by a using a three-dimensional CFD model. The conventional bipolar plate was modified by applying microchannel. The microchannel manufactured in the center of ribs of the bipolar plate allowed effective water removal from GDL due to the capillary effect, resulting in the reduction of water flooding. The operating conditions included cell temperature, inlet humidity of reactant gases, and air stoichiometry.

# 1. Modeling Approach

## 1.1 Numerical method

This work establishes a three-dimensional model using the CFD-ACE package tool. The surface reaction equations were set up at catalyst layers of two electrodes to analyze its heat transfer and electrochemical reaction. The conservation equations include,
Continuity equation:

$$\frac{\partial \rho}{\partial t} + \nabla \bullet (\rho \vec{v}) = 0 \quad (1)$$

Momentum equation:

$$\frac{\partial (\rho \vec{v})}{\partial t} + \nabla \bullet (\rho \vec{v} \vec{v}) = -\nabla p + \nabla \bullet (\bar{\bar{\tau}}) + \rho \vec{g} + \vec{F} \quad (2)$$

Darcy's law that describes porosity and permeability was applied to set thermal, chemical, and flow resistivity through porous media layers. Bruggman and Dagan model were applied in diffusion phenomenon through porous media. Temperature and water content of Nafion membrane was calculated by Springer model under constant electrical conductivity condition. It considers electro-osmotic drag and back diffusion of productive water. The numbers of cells, nodes, and volume were 328878, 337700, and 23, respectively. The calculation was repeated 500 times to obtain converging results.

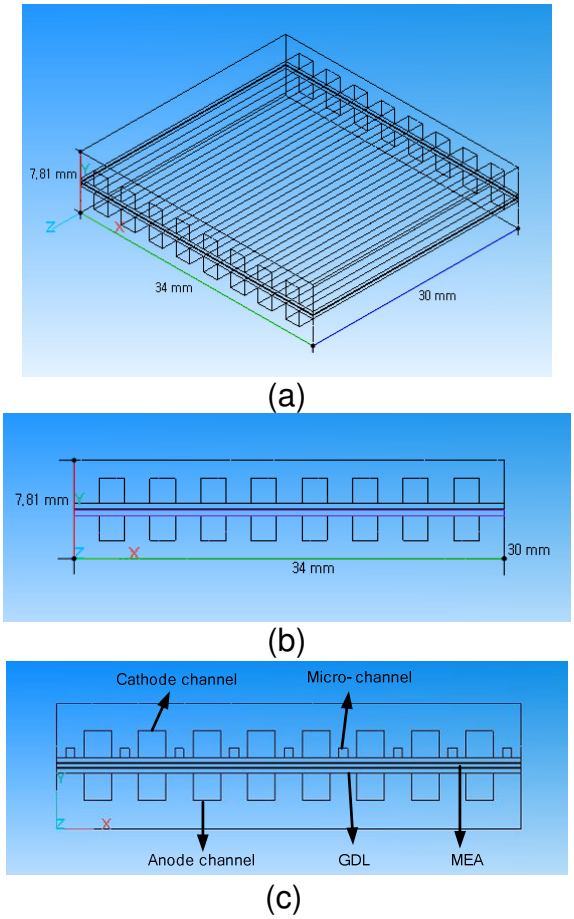


Fig. 1. Three-dimensional PEMFC model (a) Isometric view, (b) Frontal view of conventional model, (c) Frontal view of microchannel model

### 1.2 Model

A three dimensional PEM fuel cell model was developed with CFD-GEOM as shown in Fig. 1. The model consisted of a cathode bipolar plate, cathode GDL, membrane electrode assembly, anode GDL, and anode bipolar plate. Both of cathode and anode had 8 straight channels. As shown in Fig. 1(c), the cathode bipolar plate was modified by applying microchannel in the centre of the ribs. The active area of the single cell was 10.2 $cm^2$. Tables 1 and 2 summarize the specifications of the cell and the properties of the bipolar plate, gas diffusion layer, catalyst layer, and Nafion membrane.

### 1.3 Boundary conditions

Air and hydrogen velocity was set at the inlet of the gas channels with direction normal to the inlet boundary for constant mass flow rate, and the outlet of the channels was fixed at atmospheric pressure.

Table 1. Specification of PEMFC model

| Description | Value | Description | Value |
|---|---|---|---|
| GDL thickness (mm) | 0.4 | Channel width (mm) | 2.0 |
| Catalyst thickness (mm) | 0.05 | Microchannel width (mm) | 0.67 |
| Membrane thickness (mm) | 0.25 | Thermal conductivity | 0.707 |
| Bipolar plate thickness (mm) | 3.33 | Thermal conductivity of bipolar plate (W/mK) | 20.5 |

Table 2. Properties of MEA and GDL

| | Electrical conductivity (S/cm) | Porosity (%) | Permeability ($m^2$) |
|---|---|---|---|
| GDL | $1*10^{-20}$ | 0.8 | $1*10^{-11}$ |
| Catalyst | 4.2 | 0.78 | $1*10^{-11}$ |
| Membrane | 1 | 0.4 | $1*10^{-18}$ |

## 2. Simulations

### 2.1 Effects of operating conditions

The effects of operating conditions on water content and distribution in GDL and channels were simulated by using three dimensional CFD. Table 1 shows the operating conditions used in this study. Simulations were conducted by varying the cell temperature from 50 $^oC$ to 70 $^oC$, and inlet relative humidity of air from 0% to 100%. Air flow rate was changed by stoichiometries from 1 to 3. Anode was maintained at an air stoichiometry of 1 and an inlet RH of 80%. Fig. 2 shows the polarization curve for model validation. The simulation results were closely agreed with the experimental data at the same operating conditions.
The optimal conditions for water management depend on properties of MEA. The effect of operating conditions should be considered with component specifications.

Table 3. Operating conditions in simulation

| Description | Value |
|---|---|
| Cell temperature | 50, 60, 70, 80 ℃ |
| Inlet relative humidity of air | 0, 40, 60, 80, 100 % |
| Stoichiometry of air | 1, 2, 3 |

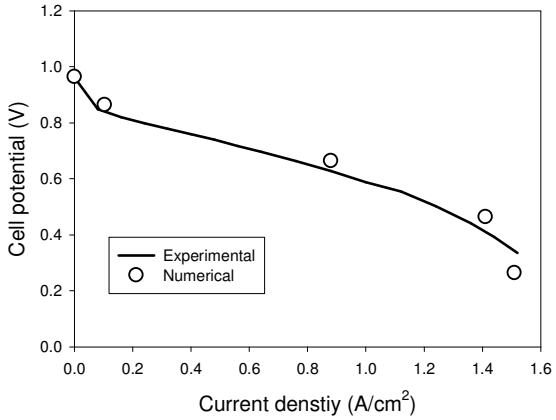


Fig. 2 Validation of results of Numerical analysis

In general, when the humidification temperature of reactant gases is higher than the cell temperature, some of the water in that stream condenses.
Fig. 3(a) shows the water distribution in GDL at the basic conditions: the cell temperature of 50 $^{o}$C, inlet air RH of 80%, air stoichiometry of 2, and operating cell potential of 0.5V. The water distribution was different in the rib region and channel region. In the channel region, the amount of water increased along the channel due to the accumulation of the product water. In the rib region, the amount of water was larger than that in the channel region. Flooding occurred easily in the rib region. As comparing with the center region, the edge region had more water content. Because the temperature in the center region was higher than that in the edge region, more water was evaporated.
Fig. 3(b) shows the results at the cell temperature of 70 $^{o}$C. In higher temperature, the water content in GDL increased, because the cell temperature determined the water saturation level of the reactant gases. The water content in the inlet region was larger than that in other regions. Evaporation increased along the channel due to the higher temperature. Fig. 3(c) shows the results at higher air stoichiometry. The water content in GDL decreased because the supplied excess air pushed the water to the outlet of the channel. On the other hands, water content became higher with a decrease in air flow rate, and the water content increased along the channel. Fig. 3(d) shows the results at low inlet air RH. The water distribution was similar to that at higher inlet humidity of air, but the amount of water decreased. The humidity of air did not affect the water distribution in GDL.
Fig. 4 shows the variation of water content in GDL and cathode channels. As the air flow rate increased, the water content in GDL changed very little. In the channel, excess air pushed the water to the outlet of channel.
Water flooding was highly affected by an erratic cell potential behavior and a pressure drop. On the contrary, when the cell temperature was higher than the humidification temperature, the pressure drop decreased and the cell performance became relatively stable. However, in the low current region, the tendency of water content will be changed. Supplying water may be evaporated easily at high cell temperatures in low current region.

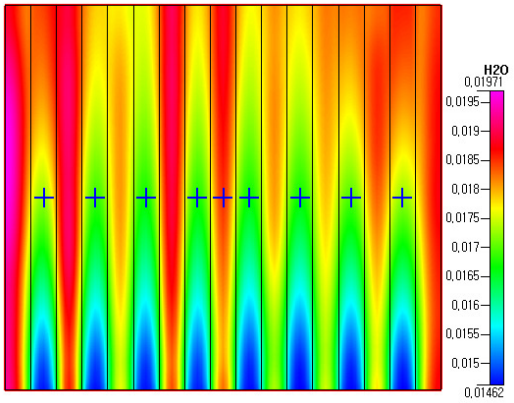


(a) $T_{cell}$=50 °C, $S_{air}$=2, $RH_{air}$=80%

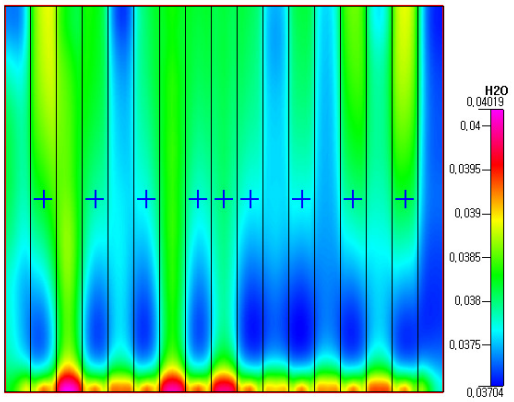


(b) $T_{cell}$=70 °C, $S_{air}$=2, $RH_{air}$=80%

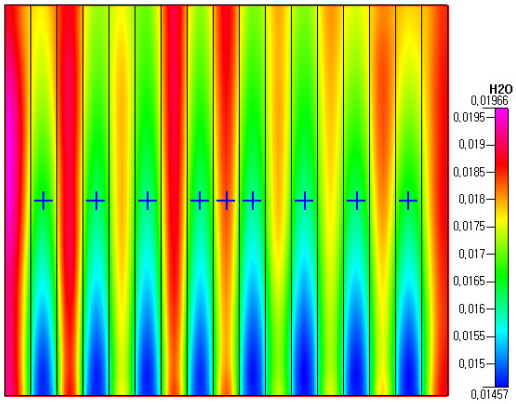


(c) $T_{cell}$=50 °C, $S_{air}$=3, $RH_{air}$=80%

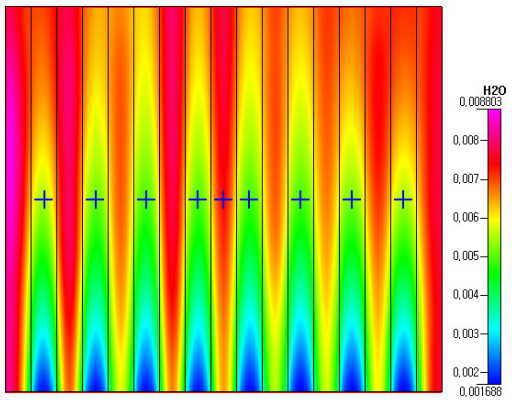


(d) $T_{cell}$=50 °C, $S_{air}$=2, $RH_{air}$=0%

Fig. 3 Water distribution of GDL in various operating conditions

In Fig. 4(c), water content increased linearly when the inlet air RH increased. Fuel and oxidant (air) streams were fully or partially humidified before entering the fuel cell. However, under certain operating conditions, especially at low cell temperatures, high humidified levels, and high current densities, the gases inside the fuel cell became oversaturated with water vapor, and condensation occurred at the cathode side, resulting in the reduction of the cell performance.

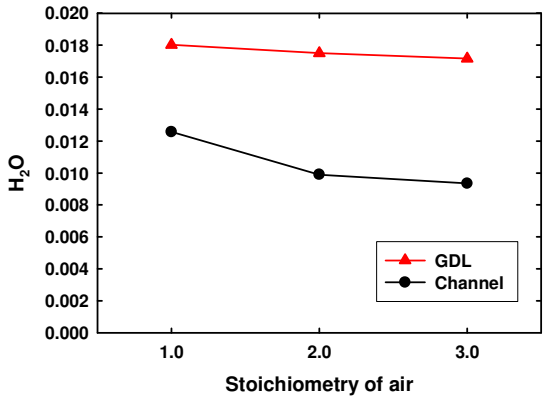


(a)

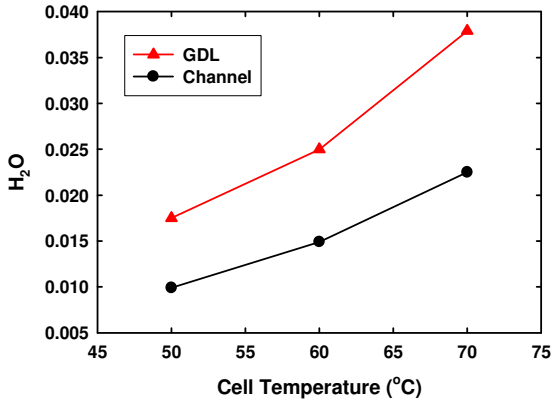


(b)

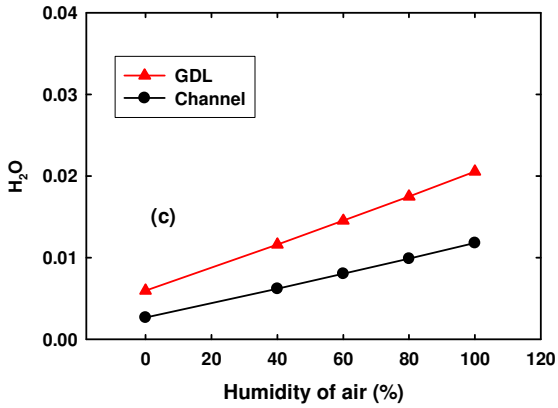


(c)

Fig. 4 Amount of water in GDL and channels according to (a) stoichiometry of air, (b) cell temperature, (c) inlet RH of air

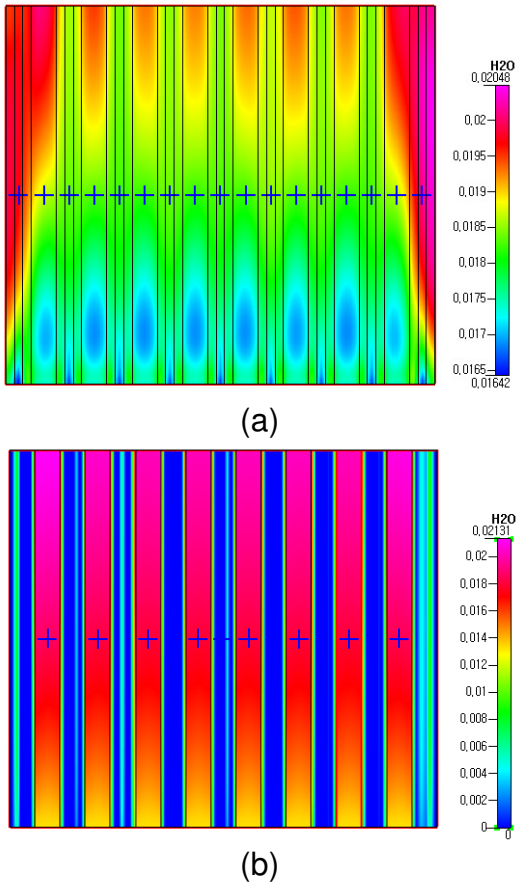


Fig. 5 Water distribution in (a) GDL, (b) flow channel using microchannel bipolar plate

## 2.2 Effects of modified channel design

The water transported from GDL to the channels should be discharged to the outlet of the flow channels. In addition, the two-phase flow governed by capillary force, evaporation, and shear force should be addressed to investigate complex process of water transport in GDL. Flow field design affects the water removal capability related with operating conditions. In this study, the modified bipolar plate was simulated to observe the variation of water distribution.

Fig. 5 shows the water distribution in GDL and channels using the microchannel bipolar plate. The difference in water content between the rib region and channel region was decreased by applying the microchannel bipolar plate, as shown in Fig. 5(a). The microchannel leaded to more water removal in the rib region and yielded even water distribution in the channels. However, total amount of water did not change significantly in the channels.

Figs. 6(a) and (b) show the pressure drop in the cathode channel with/without microchannel. The pressure drop was due to the friction within the passages or reactant gases through the cell. Liquid water may exist inside the channel either in the form of small droplets or thin film. Formation of water droplets reduces the cross sectional area in channel, resulting in the increase in the pressure drop. As shown in Fig. 6, the microchannel bipolar plate showed lower pressure drop. The pressure drop in the cathode channel applying the microchannel bipolar plate was 58% of that in the conventional one.

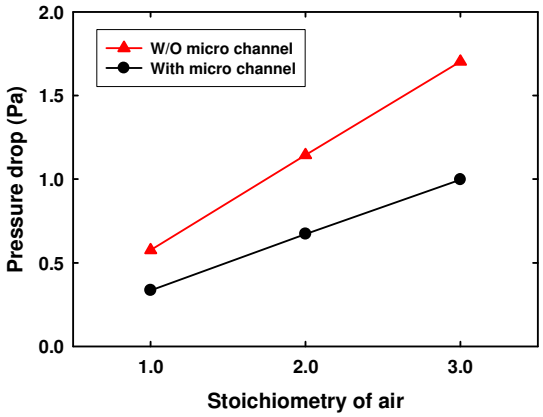


(a)

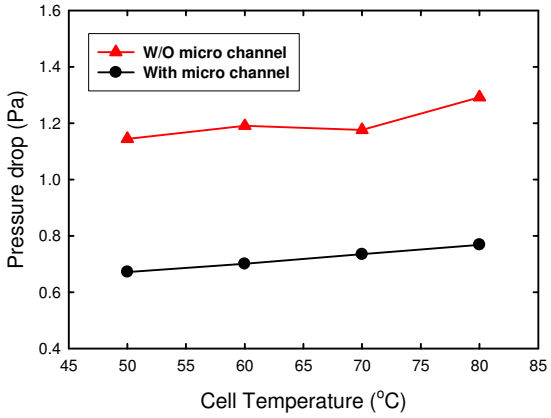


(b)

Fig. 6 Variation of pressure drop according to (a) stoichiometry of air, (b) cell temperature

As shown in Fig. 6(a), the air stoichiometry had significant effect on the pressure drop. However, the RH of air did not affect the pressure drop significantly. As shown in Fig. 6(b), the pressure drop slightly increased with an increase in the cell temperature.

## 3. Conclusions

In this study, the flooding in GDL of PEMFC with various operating conditions was investigated by CFD. The effects of the microchannel bipolar plate on the water distribution in GDL and channels were investigated.

(1) The water distribution was different in the rib region and channel region of GDL. The amount of water increased along the channel in the channel region due to accumulation of product water along the channel. In the rib region, the amount of water was larger than that in the channel region.

(2) When the fuel cell operated at high operating temperature, the water saturation level of reactant gases increased. Therefore, water content in GDL increased. The stoichiometry of air affected the amount of water. Excessive air pushed product water to the outlet of the channel. The humidity of air did not affect the water distribution, but had significant effect on amount of water.

(3) The microchannel bipolar plate was effective on the water removal from GDL and also provided more even water distribution in GDL.

## Acknowledgement

This work was supported by Mid-career Researcher Program through NRF grant funded by the MEST (No. 2009-0086642).

## References

[1] F. Barbir, PEM fuel cells: Theory and Practice, Elsevier, 2005
[2] J. E. Dawes, N. S. Hanspal, O. A. Family, A. Turan, Three-dimensional CFD modeling of PEM fuel cells: An investigation into the effects of water flooding, Chemical Engineering Sciences 64 (2009) 2781-2784
[3] L. Sun, P. H. Oosthuizen, K. B. McAuley, A number of channel to channel flow cross over through the gas diffusion layer in a PEM-fuel-cell flow system using a serpentine channel with a trapezoidal cross-sectional shape, International Journal of Thermal Sciences 45 (2006) 1021-1026
[4] B. Gao, T. S. Steenhuis, Y. Zevi, J. Y. Parlange, R. N. Carter, T. A. Trabold, Visualization of unstable water flow in a fuel cell gas diffusion layer, Journal of Power Sources 190 (2009) 493-498
[5] Z. Lu, S. G. Kandlikar, C. Rath, M. Grimm, W. Domigan, A. D. White, M. Hardbarger, J. P. Owejan, T. A. Trabold, Water management studies in PEM fuel cells, Part2: Ex situ investigation of flow maldistribution, pressure drop and two-phase flow pattern in gas channels, International journal of hydrogen energy 34 (2009) 3445-3456
[6] J. Park, X. Li, D. Tran, T. Abdel-Baser, D. S. Hussey, D. L. Jacobson, M. Arif, Neutron imaging investigation of liquid water distribution in and the performance of a PEM fuel cell, International journal of hydrogen energy 33 (2008) 3373-3384
[7] D. H. Jeon, S. Greenway, S. Shimpalee, J. W. Van Zee, The effect of serpentine flow-field designs on PEM fuel cell performance, International Journal of Hydrogen Energy 33 (2008) 1052-1066
[8] G. G. Park, Y. J. Sohn, T. H. Yang, Y. G. Yoon, W. Y. Lee, C. S. Kim, Effect of PTFE contents in the gas diffusion media on the performance of PEMFC, Journal of power sources 131 (2004) 182-187
[9] Z. Qi, A. Kaufman, Improvement of water management by a microsublayer for PEM fuel cell, Journal of power sources 109 (2002) 38-46

A1306

# Influence of nature and concentration of iron ions on the degradation of PEMFCs: a modeling study

**Romain Coulon[1,2], Alejandro A. Franco[1] and Wolfgang G. Bessler[2]**
[1]Atomic and Alternative Energies Commission of France (CEA)/LITEN/ DEHT/Laboratory of Components for Fuel Cells and Electrolyzers, and of Modeling (LCPEM), 17, Rue des Martyrs, F-38054 Grenoble Cedex 9, France
[2]German Aerospace Center (DLR), Institute of Technical Thermodynamics, Pfaffenwaldring 38-40, 70569 Stuttgart, Germany
romain.coulon1@cea.fr
alejandro.franco@cea.fr

## Abstract

Polymer Electrolyte Membrane (PEM) Fuel Cells represent a promising technology for high-efficiency energy conversion as an alternative to fossil energies. However, under practical operating conditions, the durability of the current technology is not high enough yet to be economically viable. Modeling is becoming a more and more important tool for understanding degradation mechanisms and predicting the lifetime of fuel cells. For this goal, we apply multiphysics elementary kinetic models that describe electrochemical reactions and transport processes in a highly detailed way [1-4]. This allows a reliable prediction of the long-time behavior of the cell, which always involves temporal extrapolation away from short-term measurements [5-7].

This presentation deals with a 1D model of the PEM chemical aging, which represents one of the major mechanisms inducing irreversible PEMFC performance decay. The model describes water, gas and ion transport across the PEM, production of hydrogen peroxide in the anode CL, transport of peroxide into the PEM, its decomposition, and chemical degradation of the PEM through radicals attack. Parameter identification and model validation is performed using published experimental work from several groups.

It has been observed experimentally by Kodama *et al.* that the degradation rate depends nonlinearly on the concentration of iron ions in the membrane [8]. Particularly, under very aggressive conditions the membrane degradation is not as high as expected. This study shows a model-based analysis of the influence of ion concentration on the degradation rate. The different effects of $Fe^{2+}$ and $Fe^{3+}$ are quantified.

# Introduction

One of the last hurdle to pass before commercialization of the fuel cell outside its current niche market lies in the improvement of its durability. Beside physical degradation (for example, mechanical stresses due to water management), chemical degradation is a severe source of the performance decay and cell failure [9-13]. Because of this and the high cost inferred to the cell material (Platinum, Nafion®…), the durability of the cell has to be as high as possible and must correspond to the requirement of its use (ten thousands of hours under constant load for stationary applications, thousands of hours under variable load for automotive applications).

One of the causes for the chemical degradation of the membrane is the attack of the membrane by high reactive radicals such as HO·. Those radicals are decomposition products of hydrogen peroxide. This decomposition occurs only in presence of so-called Fenton ions, such as $Fe^{2+}$, whose origin may be the oxidation of end-plate at the high potential at the cathode side [14]. Thus the concentration and occurrence of appearance of iron ions is random. However on a modeling point of view, the influence of iron ions on the degradation has not yet been analyzed in detail. This paper proposes to better understand the effect of iron ions on the degradation by studying the influence of concentration and $Fe^{2+}/Fe^{3+}$ ratio on performance degradation.

# Modeling approach

Our model can be separated in two parts, the electrode model in which is included the $H_2O_2$ production and the membrane model which includes the degradation model. Each part of the model takes into account the physical and chemical phenomena occurring in the cell.

## The electrode model

The chosen electrode morphology is that presented in [3, 15]. Carbon support (and Pt) networks are considered embedded in a hydrated ionomer medium (Nafion® phase). These structures also include nano/micropores, allowing the gas transport to the active site of the electrode. This is certainly a simple representation of the multi-scale complexity of an electrode, but it allows to capture the elementary processes taking place in the MEA and to describe, on a physical basis, the coupling between them.

The models of cathode and anode used in this work are based on the work of Franco et al. and have been described in detail previously [3, 15]. In summary, within a continuum framework, each electrode submodel is designed to describe coupled physicochemical phenomena at different geometrical scales: a microscale transport phenomena description of reactants ($H_2$ and $O_2$) and charges (protons and electrons) through the electrode and the membrane thickness and a spatially distributed microscale model of the reactant diffusion through the hydrated Nafion® ionomer layer covering the Pt/C networks, coupled to a 1D nanoscale mechanistic description of the catalyst/electrolyte interface at the electrode. The nanoscale models consist of a compact layer submodel describing in a detailed way the competitive adsorption of the intermediate reaction species and the parasite water molecules on the catalyst surface, and of a diffuse layer submodel in the electrolyte, constituted of protons and spatially fixed counter-ions (sulfonate sites) [3, 15].

Concerning the electrochemical reactions, we assume for the Oxygen Reduction Reaction (ORR) a three-step mechanism as used in the modeling work of Franco et al. [3]. On the anode side, we extend the work already done to get a precise description of production of hydrogen peroxide. The following mechanism is used for the description of hydrogen peroxide production at the anode side. The adsorbed hydrogen atom is produced by the Tafel step during the HOR,

$$O_2 + H(s) \rightleftharpoons HO_2 + (s)$$
$$HO_2 + H(s) \rightleftharpoons H_2O_2 + (s)$$

where (s) represents a sorption free-site of the catalyst surface. The kinetic coefficients related to these reactions are not known; therefore, they had to be estimated through fitting on experimental work. According to mass-action kinetics, the reaction rate is a function of the coverage of the reaction intermediates and the concentration of adsorbed species.

## The membrane model

The polymer electrolyte membrane in the cell has an important function in the cell. Indeed, it is an electrical insulator, so that produced electrons move through the outer circuit from the anode to the cathode. It should have high proton conductivity and should be gas-proof. The latter point has been shown to be a problem: The presence of oxygen at the anode and hydrogen at the cathode has been observed experimentally. The mechanism for gas permeation through the membrane is widely discussed and may depend on the hydration level in the membrane.

We model the polymer membrane in one dimension consideration transport processes of protons, water and dissolved gas species. Figure 16 presents the transport phenomena in the membrane which we describe in the model.

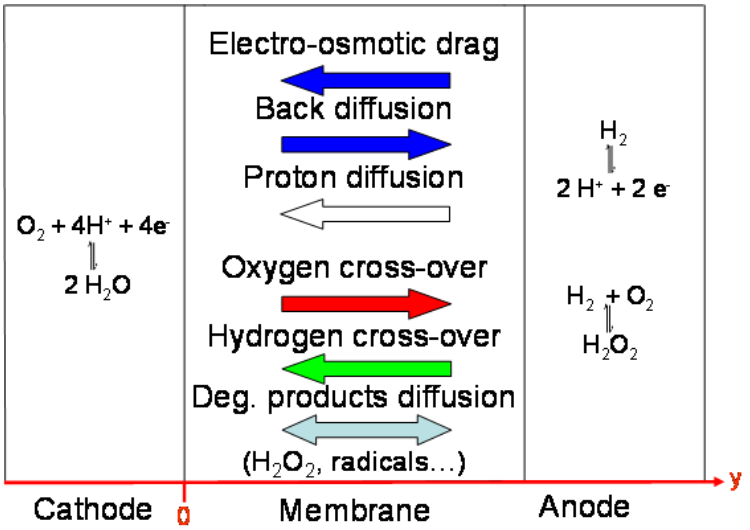


Figure 16: Transport phenomena inside the membrane

Two mechanisms are considered for the water transport:

- Electro-osmotic drag from the anode to the cathode, due to the solvatation of proton. This flux is driven by the protonic current when the cell is polarized.
- Back-diffusion from the cathode to the anode: The drag of water with proton and the production of water during the ORR induce a water gradient at the cathode side. The membrane tries to relax to a homogenous humidification, modeled by the second law of Fick for the diffusion.

No convective transport is taken into account. Our simulations are performed in an isobar environment. For more details on the transport model see Eschenbach et al [16]. The model used in this study is an extension of the previous model through the consideration of gas diffusion in the membrane and the degradation of produced $H_2O_2$ [2].

**The degradation model**

The simultaneous presence of iron ions and hydrogen peroxide induces chemical reactions leading to the decomposition of the latter into highly reactive and unstable radicals. The reactions we consider are given as

$$H_2O_2 + Fe^{2+} \rightleftharpoons Fe^{3+} + HO\cdot + HO^-$$
$$H_2O_2 + Fe^{3+} \rightleftharpoons Fe^{2+} + HOO\cdot + H^+$$
$$HOO\cdot + Fe^{3+} \rightleftharpoons Fe^{2+} + O_2 + H^+$$
$$H_2O_2 + HO \rightleftharpoons H_2O + HOO$$
$$HO\cdot + Fe^{2+} \rightleftharpoons Fe^{3+} + HO^-$$

The expression of the different reaction rates and the solving of the balance equations system permit to calculate the amount of produced radicals according to

$$v_{F1} = k_{F1} \cdot C_{H_2O_2} \cdot C_{Fe^{2+}}$$
$$v_{F2} = k_{F2} \cdot C_{H_2O_2} \cdot C_{Fe^{2+}}$$
$$v_{F3} = k_{F3} \cdot C_{HOO\cdot} \cdot C_{Fe^{3+}}$$
$$v_{F4} = k_{F4} \cdot C_{H_2O_2} \cdot C_{HO\cdot}$$
$$v_{F5} = k_{F5} \cdot C_{HO\cdot} \cdot C_{Fe^{2+}}$$

Mechanisms of chemical degradation of the membrane have been proposed previously. We use the one presented by Xie and Hayden [17]. In our kinetic model, we consider the side chain cleavage as the rate-determining step. Therefore we use this reaction in order to describe the degradation of the whole membrane. Figure 17 shows the first step of the side chain cleavage. We see that this cleavage will cause the loss of a sulphonic acid group which confers the membrane its proton conductive behavior. Thus we can expect that during the chemical aging of the membrane, the proton conductivity will decrease and thus the membrane resistance will increase.

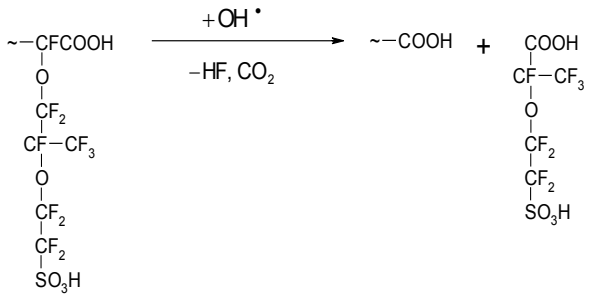


Figure 17: Side chain cleavage reaction

In order to get the evolution of the local concentration of side chain group in the membrane, we solve the equation.[1].

$$\frac{dC_{SO_3}}{dt} = -k_{DEG} \cdot C_{SO_3}.C_{HO\bullet} \qquad [1]$$

A general structure for Nafion is represented in Figure 18. Taking a value $m$ = 7 and $n$ = 1, we get a relative ratio between $SO_3$ groups and F atoms of 1 to 41. We then use the equation [2] to estimate the value of released fluoride during the degradation.

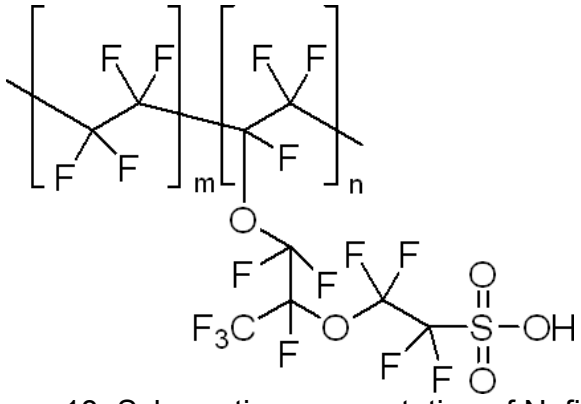


Figure 18: Schematic representation of Nafion

$$\frac{dC_{SO_3}}{dt} = 41 \cdot \frac{dC_F}{dt} \qquad [2]$$

## Simulations results

In the simulations presented here, the following assumptions have been made concerning the state and the behavior of iron ions:

- At the beginning of the simulations, the concentration distribution of iron ions along the thickness of the membrane is homogeneous. The study does not focus on the origin and the kinetics of the production of iron ions.
- We neglect any electrostatic interaction of iron ions with the negatively loaded side chain.
- The iron ions are present the forms of either $Fe^{2+}$ or $Fe^{3+}$. We consider neither complexation reaction nor crystallization of iron in the fuel cell.

The membrane model was integrated in the MEMEPhys® simulation package (containing the electrodes, GDL and channels models [18]) within Matlab/Simulink [3, 15]. The membrane model is programmed in C language and was coupled to Simulink through an S-Function. The 1D transport in the membrane uses the finite-volume discretization method. The simulations were performed on an Intel Core 2 Duo processor 2.4 GHz with 3 GB RAM.

Table 1 presents the main parameters used for the simulations.

Table 1: Model parameters

| Parameters | Value | Ref |
|---|---|---|
| $P_a$ | 1 atm | - |
| $P_c$ | 1 atm | - |
| $RH_a$ | 80 % | - |
| $RH_c$ | 80 % | - |
| $T$ | 333 K | - |
| $\lambda_a$ | 1.2 | - |
| $\lambda_c$ | 2 | - |
| $k_{F1}$ | $63 \cdot 10^{-3}$ $m^3 \cdot mol^{-1} \cdot s^{-1}$ | [19] |
| $k_{F2}$ | $2 \cdot 10^{-6}$ $m^3 \cdot mol^{-1} \cdot s^{-1}$ | [20] |
| $k_{F3}$ | $3.3 \cdot 10^{2}$ $m^3 \cdot mol^{-1} \cdot s^{-1}$ | [21] |
| $k_{F4}$ | $3.3 \cdot 10^{4}$ $m^3 \cdot mol^{-1} \cdot s^{-1}$ | [22] |
| $k_{F5}$ | $3.3 \cdot 10^{5}$ $m^3 \cdot mol^{-1} \cdot s^{-1}$ | [23] |
| $k_{DEG}$ | $3.3 \cdot 10^{4}$ $m^3 \cdot mol^{-1} \cdot s^{-1}$ | fitted |

**Influence of the global iron ions concentration on the degradation**

The first parameter we propose to study is the global concentration of iron ions. We do not consider a dynamic production of iron ions in the cell. We rather assume that the ions are uniformly distributed in the membrane volume. For that purpose, we set as start condition several concentrations of iron ions, either pure ferrous ions ($Fe^{2+}$) or pure ferric ions ($Fe^{3+}$). We follow over time the global quantity of fluoride released by the cell.

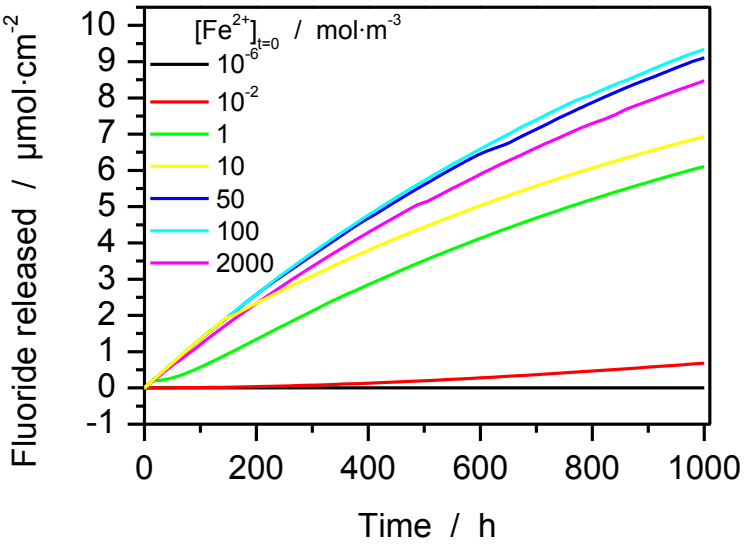


Figure 19: Evolution of produced fluoride with different $Fe^{2+}$ concentrations

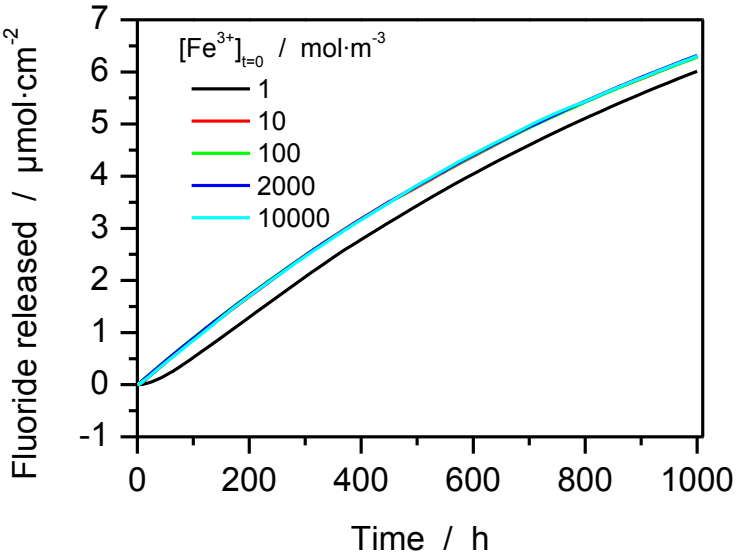


Figure 20: Evolution of produced fluoride with different $Fe^{3+}$ concentrations

Figure 19 and Figure 20 present the simulations results for these cases. We see a different impact on the fluoride release depending if ferrous or ferric ions are present at the beginning of the simulation. Degradation in a cell with only ferrous ions at the beginning will be worse than in a cell with ferric ions. Moreover, we notice than from a concentration in $Fe^{3+}$ of about 10 $mol \cdot m^{-3}$, there is no significant impact of the concentration on the degradation. On the contrast, in a system with ferrous ions, the quantity of produced fluoride increases with increasing iron concentration, but then, under very aggressive conditions, the quantity of produced fluoride decrease.

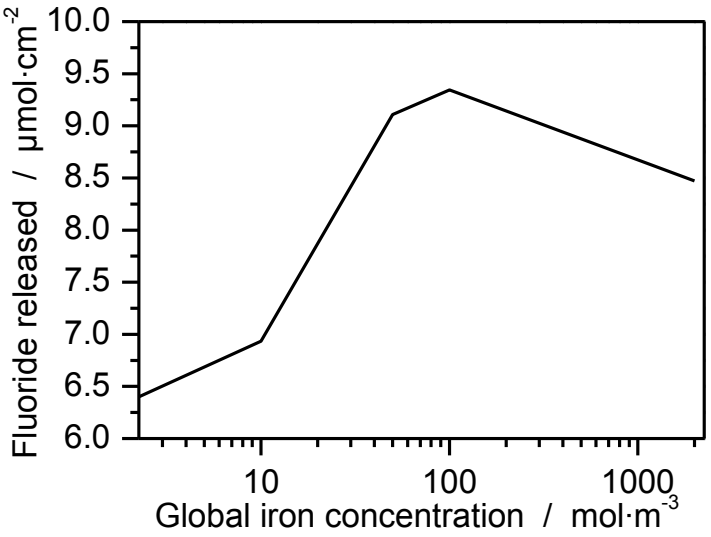


Figure 21: Evolution of the produced fluoride with iron concentration (only $Fe^{2+}$ at start)

Figure 21 shows a logarithmic plot of the quantity of produced fluoride versus ferrous iron concentration. On this plot, the maximum value is to see for a ferrous ion concentration between 100 and 1000 $mol \cdot m^{-3}$. Such a behavior has been experimentally observed [8].

A closer look at the curve for a concentration of 10 $mol \cdot m^{-3}$ in Figure 19 reveals a change in the slope of the fluoride production. This phenomenon can be explained regarding Figure 22. It appears that during the degradation, ferrous ions are not stable and its end state will be ferric ions. At the point when equilibrium is reached, we observe the change in the slope and the degradation is slower. This confirms the observation that ferrous ions are more aggressive than ferric ions for the membrane.

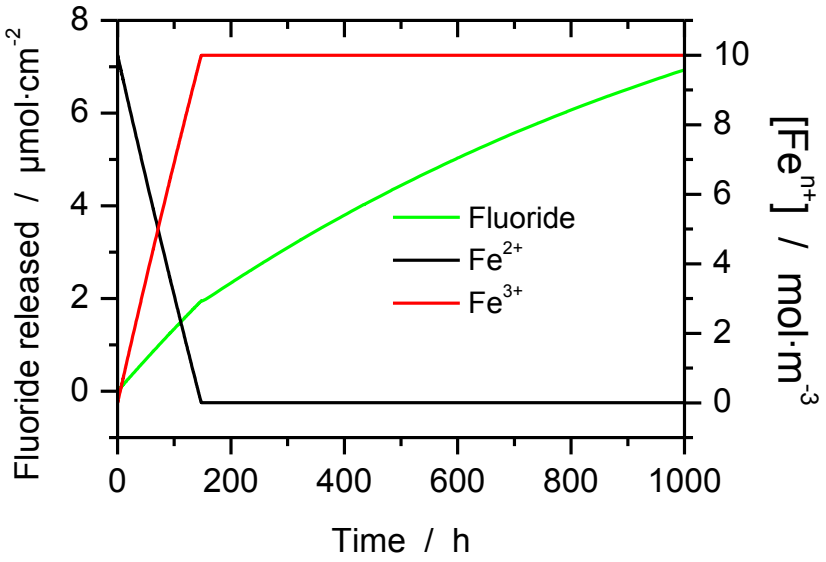


Figure 22: Evolution iron and fluoride concentration for a total initial concentration of 10 $mol \cdot m^{-3}$.

### Influence of the $Fe^{2+}/Fe^{3+}$ ration on the degradation

In the next section, we test the influence of the type of iron ions at the beginning of the simulation. We simulate for a global concentration of 1, 10 and 100 $mol \cdot m^{-3}$ and study three different cases:

- Only ferrous ions
- Only ferric ions
- Equivalent concentration of ferrous and ferric ions

Figure 23, Figure 24 and Figure 25 show the simulation results for all the cases. We notice that the ratio has an influence only for high concentration of iron. At lower concentration, the steady-state of iron is reached faster, thus the whole simulation correspond to the case where we only have ferric ions in the cell. For higher concentration, the transient time is longer and thus the degradation profile is similar to that one we get for a simulation with only ferrous ions from the beginning.

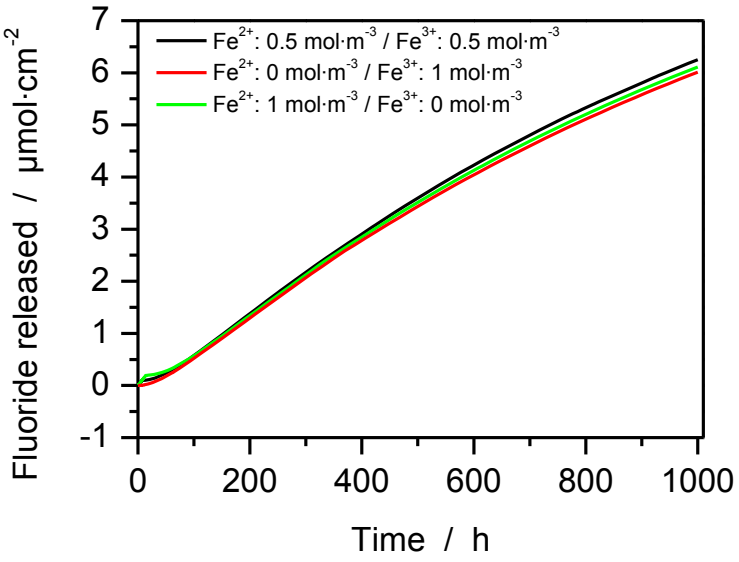


Figure 23: Degradation with different iron repartition (1 $mol \cdot m^{-3}$)

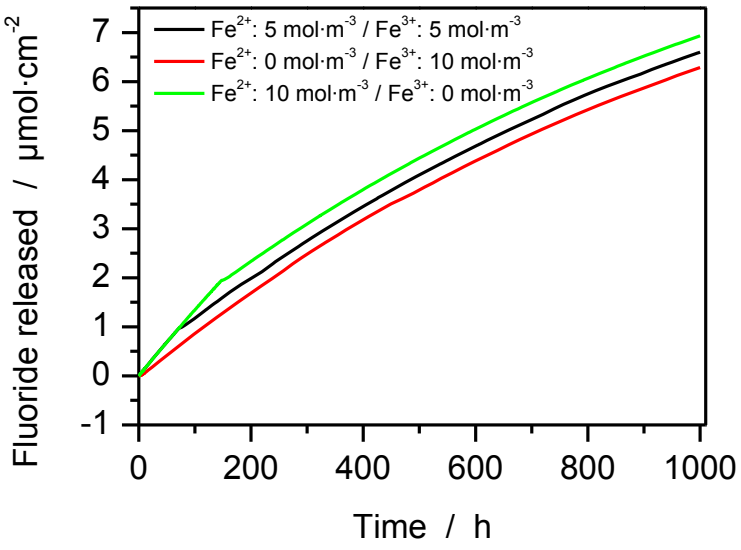


Figure 24: Degradation with different iron repartition (10 $mol \cdot m^{-3}$)

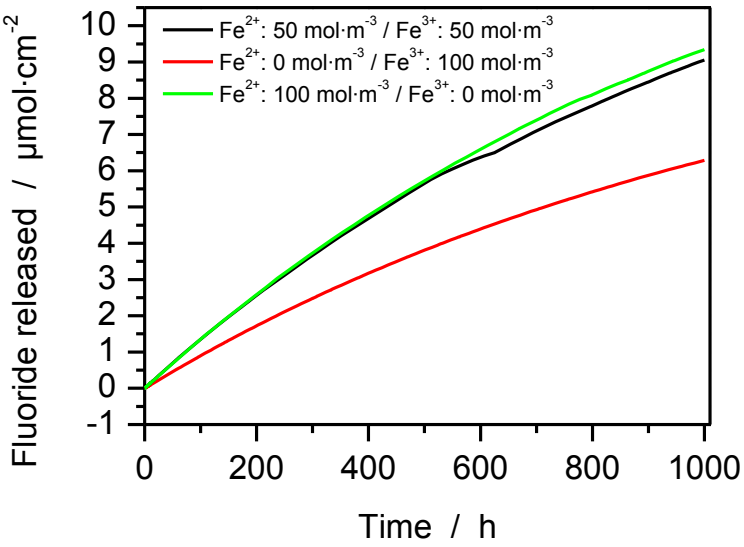


Figure 25: Degradation with different iron repartition (100 mol·m$^{-3}$)

## Conclusions

In this study we have presented an electrochemical model to investigate the impact of iron ions on the chemical degradation of perfluorosulfonated acid membranes like Nafion® during operation of a single-cell PEFC. Iron ions are one of the key parameters in the degradation process because they initiate the production of highly reactive radicals in the membrane through the decomposition of hydrogen peroxide, product of a reaction involving the parasitic presence of oxygen at the anode due to crossover.

The simulation predictions indicate a higher degradation rate in presence of ferrous ($Fe^{2+}$) ions as compared to ferric ($Fe^{3+}$) ions. The concentration of iron ions shows a volcano-type influence on degradation: the membrane is not more severely degraded at high concentration of ferrous ions. It seems that with increasing ferrous ions concentration, a maximum is reached and then the degradation becomes less.

## References

[1] W.G. Bessler, S. Gewies, M. Vogler, Electrochimica Acta, 53 (2007) 1782-1800.
[2] R. Coulon, W. Bessler, A.A. Franco, ECS Transactions, 25 (2010) 259-273.
[3] A.A. Franco, P. Schott, C. Jallut, B. Maschke, Fuel Cells, 7 (2007) 99-117.
[4] A.A. Franco, S. Passot, P. Fugier, C. Anglade, E. Billy, L. Guetaz, N. Guillet, E. De Vito, S. Mailley, Journal of The Electrochemical Society, 156 (2009) B410-B424.
[5] A.A. Franco, M. Tembely, Journal of The Electrochemical Society, 154 (2007) B712-B723.
[6] A.A. Franco, M. Guinard, B. Barthe, O. Lemaire, Electrochimica Acta, 54 (2009) 5267-5279.
[7] A.A. Franco, PEMFC degradation modeling and analysis, in: C. Hartnig, C. Roth (Eds.) Polymer electrolyte membrane and direct methanol fuel cell technology (PEMFCs and DMFCs), Woodhead, Cambridge, UK, (in press) 2011.
[8] K. Kodama, F. Miura, N. Hasegawa, M. Kawasumi, Y. Morimoto, ECS Meeting Abstracts, 502 (2006) 1185-1185.

[9] J. Healy, C. Hayden, T. Xie, K. Olson, R. Waldo, M. Brundage, H. Gasteiger, J. Abbott, Fuel Cells, 5 (2005) 302-308.
[10] H. Tang, S. Peikang, S.P. Jiang, F. Wang, M. Pan, Journal of Power Sources, 170 (2007) 85-92.
[11] X. Huang, R. Solasi, Y. Zou, M. Feshler, K. Reifsnider, D. Condit, S. Burlatsky, T. Madden, Journal of Polymer Science Part B: Polymer Physics, 44 (2006) 2346-2357.
[12] A. Kusoglu, A.M. Karlsson, M.H. Santare, S. Cleghorn, W.B. Johnson, Journal of Power Sources, 161 (2006) 987-996.
[13] R. Borup, J. Meyers, B. Pivovar, Y.S. Kim, R. Mukundan, N. Garland, D. Myers, M. Wilson, F. Garzon, D. Wood, P. Zelenay, K. More, K. Stroh, T. Zawodzinski, J. Boncella, J.E. McGrath, M. Inaba, K. Miyatake, M. Hori, K. Ota, Z. Ogumi, S. Miyata, A. Nishikata, Z. Siroma, Y. Uchimoto, K. Yasuda, K.-i. Kimijima, N. Iwashita, Chemical Reviews, 107 (2007) 3904-3951.
[14] A. Pozio, R.F. Silva, M. De Francesco, L. Giorgi, Electrochimica Acta, 48 (2003) 1543-1549.
[15] A.A. Franco, P. Schott, C. Jallut, B. Maschke, Journal of The Electrochemical Society, 153 (2006) A1053-A1061.
[16] M.P. Eschenbach, R. Coulon, A.A. Franco, J. Kallo, W.G. Bessler, Solid State Ionics, In Press, Corrected Proof (2010).
[17] T. Xie, C.A. Hayden, Polymer, 48 (2007) 5497-5506.
[18] R. Ferreira de Morais, D. Loffreda, P. Sautet, A.A. Franco, Electrochimica Acta, accepted (2011).
[19] J. De Laat, H. Gallard, Environmental Science & Technology, 33 (1999) 2726-2732.
[20] S.-S. Lin, M.D. Gurol, Environmental Science & Technology, 32 (1998) 1417-1423.
[21] F. Haber, J. Weiss, The Catalytic Decomposition of Hydrogen Peroxide by Iron Salts, in, 1934, pp. 332-351.
[22] H. Christensen, K. Sehested, H. Corfitzen, The Journal of Physical Chemistry, 86 (1982) 1588-1590.
[23] G.V. Buxton, L. Clive, W. Greenstock, P. Helman, A.B. Ross, J. Phys. Chem. Ref. Data, 17 (1988) 513-886.

A1307

# Numerical Simulation of Solid Oxide Fuel Cell for Impedance Analysis

**Rafat Mohammadi, Majid Ghassemi, M. Hossein Hamedi and Y. Mollayi Barzi**
K.N. Toosi University of Technology
Mechanical Engineering Department
No. 15, Pardis Street, MolaSadra Avenue, Vanak Sq.,
Tehran/Iran
Tel.: +98-21-84063414
Fax: +98-21-84063414
rmohammadi@dena.kntu.ac.ir

## Abstract

The purpose of the current study is to model and simulate the impedance of a solid oxide fuel cell (SOFC) anode. The electrochemical impedance spectroscopy (EIS) is a powerful non-destructive method for obtaining the individual losses, characterization of materials, investigation of transport properties and the performance optimization of SOFCs. Efforts are devoted to develop tools that numerically evaluate the EIS experimental results.
In this study a planar SOFC anode is modeled and the electrochemical spectra at the anode are obtained. The simulation is based on transient model of the anode when a periodic voltage is imposed. The model fully couples electrochemical kinetics with gas phase diffusion. The electrochemistry at the anode is modeled using Butler-Volmer equation, and gas diffusion model is based on the species equations. An in-house finite difference based code is used to solve the system of nonlinear equations. It is found that the Nyquist plot shows a capacitive semicircle which is identical to the gas conversion impedance as reported in literatures. A parametric study is also carried out by changing parameters, such as supplied gas compositions and cell dimensions, and the results are discussed. Furthermore, it is shown that the simulation results are in good agreement with published results.

## Introduction

A fuel cell generates electrical power through an electrochemical reaction by converting chemical energy of a fuel into electrical energy. fuel cells have higher efficiency compared to conventional combustion engines due to the fact that their efficiency avoid the limitations of Carnot cycle. In addition, the fuel cell itself has no moving parts that makes it quiet and reliable. Furthermore, they have lower pollutant emissions, lower equipment maintenance, and higher power density [1]. Solid oxide fuel cells (SOFCs) are one of the fuel cell types that operate between 800 and 1100°C due to the low ionic conductivity of electrolytes such as yttria-stabilized zirconia (YSZ) at lower temperatures. In this type of fuel cell oxidation of hydrogen and reduction of oxygen produces the electricity, water and heat. SOFCs can be used in a wide range of applications. They appear suitable for stationary electricity generation, both for power plant scales, and for small residential applications (combined heat and power generation) [2].

The electrochemical impedance spectroscopy (EIS) is a non-destructive test that emerges as an effective approach for performance optimization, failure mode diagnosis, revealing dynamic properties and for obtaining information on individual losses in the SOFCs [3]. In order to analyzing the experimental results of EIS, simulation of electrochemical impedance spectra is essential. Several researchers have developed SOFC impedance models. Initially EIS measurements were mainly used to determine the conductivity of the SOFC components such as electrolyte and electrode materials [4].
Wagner et al. presented the EIS measurements of polymer electrolyte fuel cells (PEFCs) as well as SOFCs [5]. In this experimental study the anode and cathode behavior was determined independent of a reference electrode using a symmetric gas supply of hydrogen or oxygen on both electrodes at open circuit voltage. The measured EIS was simulated with an equivalent circuit which enabled the calculation of the individual voltage losses in the fuel cell. The experiment not only determined the charge transfer resistances but also the diffusion term of the low frequency region of the cells. A gas conversion impedance model for SOFC anodes was derived by Primdahl and Mogensen [6]. In this study a simple continuously stirred tank reactor (CSTR) model was utilized. The model illustrated the anodes measurement with the reference electrode. The results were compared to the actual EIS measurements. In another study Primdahl and Mogensen measured the gas conversion impedance in different setups to analyze and compare the correlation between the gas conversion impedance and geometry parameters [7]. Their results showed an extra arc in impedance spectra which is called gas conversion or gas diffusion impedance. The experimental and numerical EIS study for anode reaction mechanisms was presented by Bieberle and Gauckler [8]. In this study a series of steps for the overall electrochemical oxidation of hydrogen were proposed. Bessler [9] presented a new computational method for impedance simulations of SOFCs based on the Bieberle and Gauckler proposed mechanisms [8]. The suggested method was based on transient numerical simulations. In two other studies [10,11] Bessler used the previous proposed model [9] for two different SOFC geometries.

Kato et al. also presented experimental results for SOFC impedance [12]. In their study the cell impedance was measured by varying the fuel utilization and gas flow rate. In another study by Takano et al. a theoretical simulation based on an electrical circuit presented that studied the electrochemical impedance of commercially available SOFCs under practical power generation conditions [13].

The purpose of the current study is to numerically investigate the electrochemical impedance of a SOFC anode. As known gas phase transport of reactants and products have a strong effect on the performance of SOFC. These phenomena influence the electrochemical impedance spectra. Indeed the experimental SOFC impedance spectra show two dominant features, a high-frequency process (1-10 kHz) associated with electrochemistry and a low-frequency process (~10 Hz) associated with gas conversion in the channels[6,7] that result in a capacitive semicircle in Nyquist plot. The present study investigates the SOFC anode performance by analyzing the latter feature.

## 1. MODEL DESCRIPTION

The schematic of the planar SOFC is depicted by Figure 1. In addition, tables 1 and 2 list the numerical values used for simulation. As shown by the Figure 1 hydrogen as the fuel passes through anode channel. In the present model it is assumed that gases behave as ideal gases and the total pressure and temperature are assumed to be constant through the entire electrode. There is no net change in the number of moles in gas phase due to the electrochemical reaction (Eq.1), so, this assumption is quite reasonable. In addition, the overvoltage from electrolyte and cathode are neglected. Furthermore, anode ohmic overvoltage and concentration overvoltage within the porous anode is ignored. So the obtained results present anodic losses including both channel transport and electrochemistry.

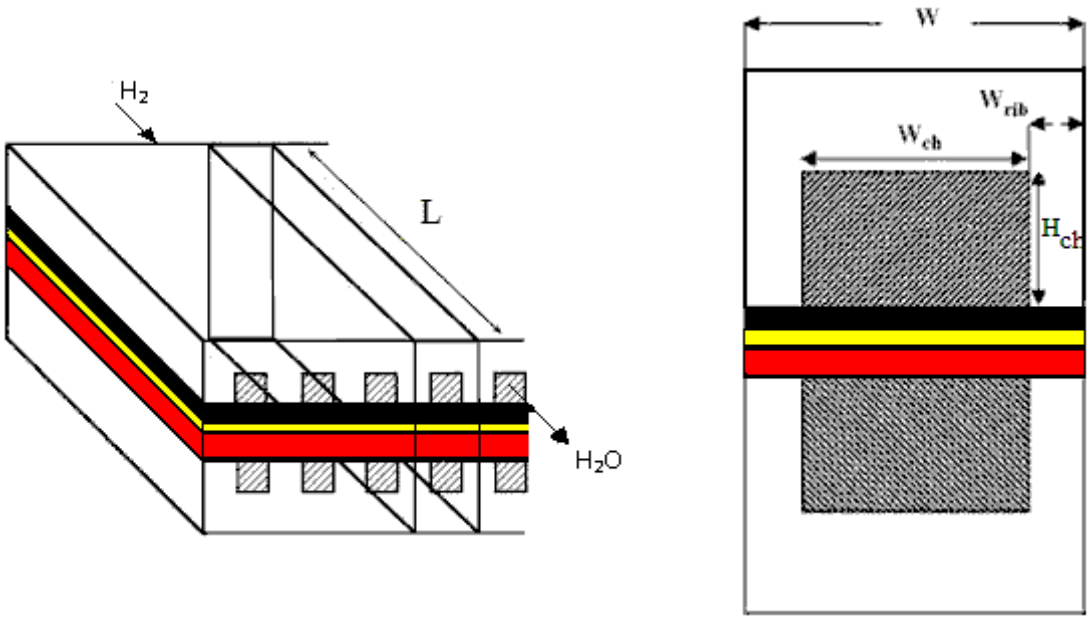


Figure 1: Schematic of the planar SOFC

Table 1: Dimensions of a typical solid oxide fuel cell [14]

| Element | Size (mm) |
|---|---|
| Cell length (L) | 19 |
| Unit cell width (W) | 2 |
| Channel width ($W_{ch}$) | 1 |
| Channel height ($H_{ch}$) | 1 |
| Rib width ($W_{rib}$) | 0.5 |

Table 2: The operating conditions, electrochemical and transport properties of the typical solid oxide fuel cell [14]

| Description | Value |
|---|---|
| Anode inlet pressure | 1 (atm) |
| Cell temperature | 750 °C |
| Faraday's constant | 96484.56 (C/mole) |
| Hydrogen diffusivity | $9\times10^{-4}$ ($m^2$/s) |
| Anode exchange current density | $4.834\times10^{-3}$ (A/$m^2$) |
| Universal gas constant | 8.314 ($m^3$.kpa/kmol.K) |

## 1.1 Electrochemical Model

For hydrogen fuel the electrochemical oxidation reactions of the SOFC at the anode is as follows:

$$H_2 + 1/2O_2 \rightarrow H_2O \qquad (1)$$

For determination of the total voltage (electromotive force (EMF)) for an electrochemical reaction the Nernst equation can be used. In SOFC the Nernst voltage ($V_{nernst}$) is as follows [2]:

$$V_{nernst} = \frac{-\Delta g_f^{\circ}}{2F} + \frac{RT}{2F} \ln\left(\frac{p^*_{H_2}\, p^{*\,1/2}_{O_2}}{p^*_{H_2O}}\right) \qquad (2)$$

Where $\Delta g_f^{\circ}$ is the Gibbs free energy change at standard state, $p^*_i$ denotes the partial pressure of reactants and products in the bulk anodic and cathodic flows, F is Faraday's constant, R represents universal gas constant, and T is temperature.

The actual SOFC voltage is decreased from its open circuit voltage due to the irreversibility called overvoltage or polarization (η). In the present study the anode overvoltage ($\eta_{anode}$) of an SOFC is analyzed while the electrolyte and cathode overvoltage is ignored. Moreover, anode ohmic overvoltage is neglected. Therefore the anode overvoltage is made up of concentration overvoltage ($\eta_{conc}$) and activation overvoltage ($\eta_{act}$).

In proximity of the reacting sites in the electrode, the concentration of reactants and products of the electrochemical reaction is different from the concentration in the bulk flow of the gases, and this is related to a phenomenon of mass transport by diffusion. Therefore, the true theoretical reversible voltage of the cell must be calculated by taking into account the reactant/product concentration occurring in proximity of the reaction sites:

$$V_{nernst} = \frac{-\Delta g_f^{\circ}}{2F} + \frac{RT}{2F} \ln\left(\frac{p_{H_2} p^{1/2}_{O_2}}{p_{H_2O}}\right) \qquad (3)$$

Where $p_i$ denotes the reactant and product partial pressure at the reaction sites. The difference between Eqs.(2) and (3) gives the departure from the theoretical thermodynamic voltage occurring due to diffusion effect, i.e. the concentration loss:

$$\eta_{conc} = \frac{RT}{2F} \ln\left(\frac{p^*_{H_2} p_{H_2O}}{p_{H_2} p^*_{H_2O}}\right) + \frac{RT}{2F} \ln\left(\frac{p^*_{O_2}}{p_{O_2}}\right)^{1/2} \qquad (4)$$

Where the first term of Eq. (4) represents the anodic concentration overvoltage and the second term is the cathodic one. Therefore the anodic concentration overvoltage in terms of the mass fraction of the gases ($y_i$) becomes as follows:

$$\eta_{conc} = \frac{RT}{2F}\ln\left(\frac{y^{*}_{H_2} y_{H_2O}}{y_{H_2} y^{*}_{H_2O}}\right) \qquad (5)$$

The activation overvoltage is determined from the Butler–Volmer equation that relates the activation overvoltage to the faradic current density (i). The Butler-Volmer equation in implicit form for a symmetric two electron transfer is as follows [2]:

$$i = i^{o}\left\{\exp\left(\frac{F}{RT}\eta_{act}\right) - \exp\left(-\frac{F}{RT}\eta_{act}\right)\right\} \qquad (6)$$

Where $i^{\circ}$ is exchange current density.

## 1.2 Mass Transfer Model

The mass transfer along anode channel is simulated using species conservation equation. In EIS experiments the impedance of SOFCs often obtained by single chamber setups and symmetrical cells. So, there is no convection flow and there is only diffusion transport in anode channel. The one-dimensional species conservation equation is given by:

$$\frac{\partial(\rho y_i)}{\partial t} = -\frac{\partial J_i}{\partial x} + W_i \qquad (7)$$

Where ρ is gas density, $J_i$ represents the diffusive mass flux and $W_i$ is volume-specific mass production rates of species i. The diffusive mass flux is given by Fick's law. Therefore, the species equation becomes as follows:

$$\frac{\partial(\rho y_i)}{\partial t} = \frac{\partial}{\partial x}\left(\rho D_{i,j}\frac{\partial y_i}{\partial x}\right) + W_i \qquad (8)$$

Where $D_{i,j}$ is binary diffusivity between species i and j. The area-specific mass production rates of species i ($w_i$) is given by the faradic current due to the electrochemical reaction of fuel as follow:

$$w_{H_2} = -\frac{iM_{H_2}}{2F} \qquad (9)$$

$$w_{H_2O} = \frac{iM_{H_2O}}{2F} \qquad (10)$$

Where $M_i$ is $i^{th}$ species molecular mass. At high temperature all the gaseous components are assumed to behave as ideal gases:

$$p = \frac{\rho RT}{M_m} = \rho RT\sum_i y_i/M_i \qquad (11)$$

Mentioned equations form a system of coupled partial differential equations. The proper boundary conditions are required to solve these equations. At the channel inlet the species concentrations are set as boundary condition, and at the outlet the fully developed assumption is considered.

## 2. SIMULATION PROCEDURE

In order to solve the coupled nonlinear mass transfer and electrochemical equations a code based on finite difference method is developed and utilized. The computational domain is discretized by a 50 uniform grid (nx) in longitudinal direction. The grid independency of the results is examined and insured, see Figure 4. The Impedance simulation is in time domain as proposed by Bessler [9]. In this method a harmonically varying overvoltage is imposed to the anode overvoltage as follows:

$$\eta_{anode} = \eta_{steady} + \eta_{excitation} \sin(2\pi ft) \qquad (12)$$

Where $\eta_{steady}$ is time-invariant contribution and represents the steady-state overvoltage, $\eta_{excitation}$ denotes ac excitation amplitude and f is the excitation frequency. The initial steady state is achieved by setting the $\eta_{excitation}$ equal to zero. The obtained results are set as initial values for the transient analysis. Then at a specified frequency the governing equations are time integrated to determine the transient current i(t) of the system. Then the electrochemical impedance of assumed frequency is obtained by these equations:

$$Y' = \frac{2}{T.\eta_{exitation}} \int_{t=0}^{T} i(t) \sin(2\pi ft)\, dt \quad (13)$$

$$Y'' = \frac{2}{T.\eta_{exitation}} \int_{t=0}^{T} i(t) \cos(2\pi ft)\, dt \quad (14)$$

Where Y' is real part of admittance, Y'' is its imaginary part of admittance, and T denotes period (T=1/f). Finally the impedance could be determined as follows:

$$Z=Y^{-1} \qquad (15)$$

This process is repeated for a range of frequency to obtain an impedance spectrum. In present paper the impedance is calculated for a frequency range of $10^{-4}$ to $10^{4}$ Hz with 10 impedance points per frequency decades. Relaxation frequencies ($f_g$) are determined with 100 points/decade resolution. The developed simulation code has the capability to be used in studying the effects of various parameters on forecasting the electrochemical impedance of SOFC and can be used as a suitable tool to optimize the behavior and operation of the fuel cell. Therefore, a parametric study is carried out and discussed in the following section.

## 3. Results

For verification purposes the electrochemical impedance spectrum is obtained and compared using the same parameters as Bessler and Gewies [11]. As shown by Figure 2 the impedance spectra shows a similar trend for both studies. The slight difference is due to relaxation frequency that is 26 Hz in this study.

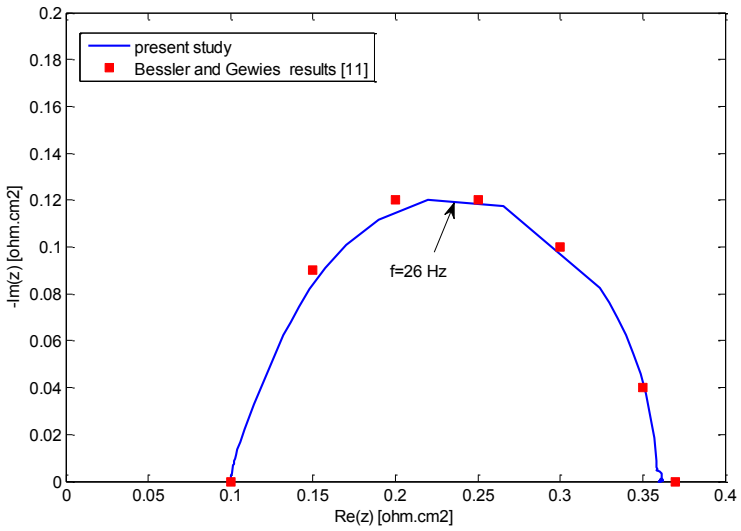


Figure 2: Electrochemical impedance spectrum

All presented results in the following section are obtained using the parameters given in Tables 1 and 2. In addition, the excitation amplitude is considered to be 1 mV, the inflow hydrogen concentration is assumed to be at 99%, and the electrode charge-transfer resistance sets to 0.1 ohm.cm2 at open-circuit conditions as observed in experiments [6]. Figure 3 depicts the impedance spectra for $\eta_{steady}$ =0V. The nyquist plot consist of a semicircle with a relaxation frequency of 6 Hz. The observed impedance feature is for anodic gas-phase concentration variations which is due to our initial assumptions. Primdahl and Mogensen called this feature gas conversion or gas diffusion impedance [6,7] and Bessler used the term gas concentration impedance for this feature [10]. This impedance feature is related to concentration polarization. The gas conversion resistance ($R_g$)is calculated from the intersections of the arc with the real axis, see Figure 3-a. Also the electrode charge-transfer resistance appears as high frequency real part.
Moreover, simulation results show that when excitation amplitude changes from 1mV to 50mV the impedance spectra don't change. Consequently the coupled electrochemistry and gas diffusion phenomena simulated in this work behave linearly for excitation amplitudes up to 50 mV.

(a) (b)

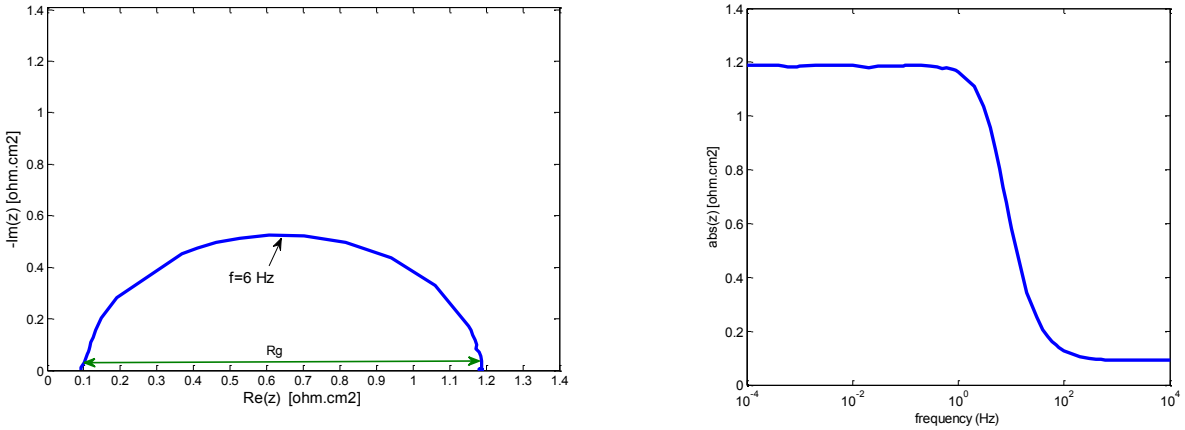


Figure 3: Electrochemical impedance spectra (a) Nyquist plot (b) Bode plot

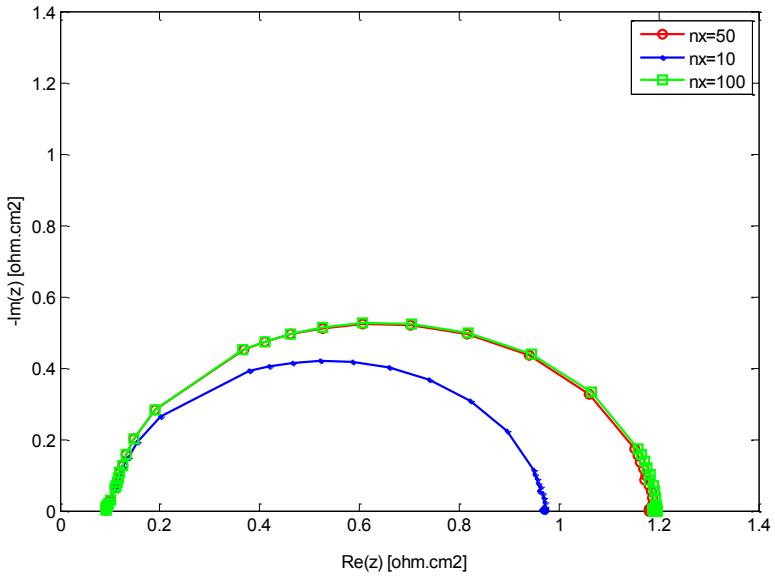


Figure 4: Electrochemical impedance spectra for different grid numbers

## 3.1. Effect of steady state overvoltage

Figure 5 shows the simulated impedance spectra at steady state overvoltage of $\eta_{steady}$ = 0, 0.1, 0.2, and 0.3 volt. At each steady state overvoltage, only one arc appears in the nyquist plot. The shape of the arc is independent of overvoltage. Electrode charge-transfer resistance of the electrochemical reaction decreases when overvoltage increases.

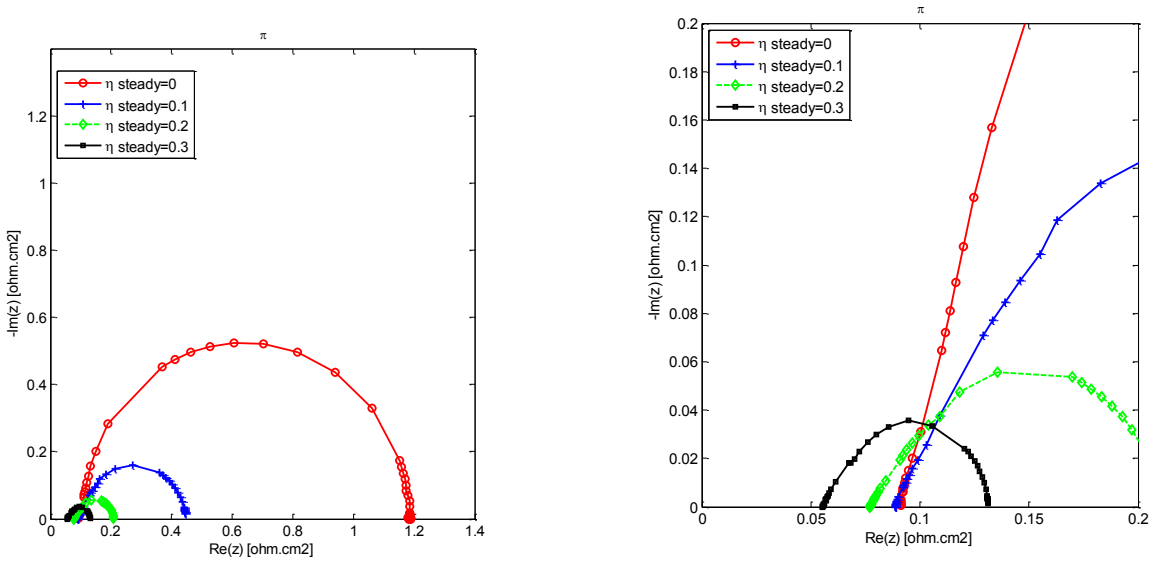


Figure 5: Electrochemical impedance spectra for different steady state overvoltage (The right figure is an expanded view of the high-frequency region)

## 3.2 Effect of cell dimensions

The variations of the calculated impedance versus the fuel cell length of 19mm (base dimension), 10mm, and 40mm, and channel height of 1mm (base dimension), 0.1mm, and 10 mm are shown in Figure 6. This Figure shows that variation of fuel cell dimensions has a strong influence on the gas conversion impedance. Increasing the cell length and decreasing the channel height cause a decrease in diffusive transport inside of the channel. consequently gas conversion resistance (the diameter of the semicircles) increases.

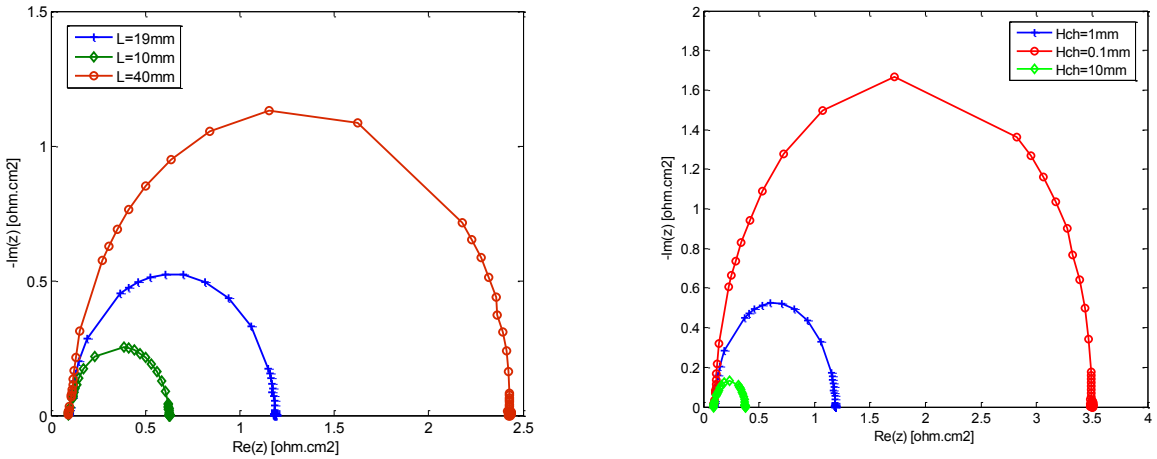


Figure 6: Electrochemical impedance spectra for different cell dimensions

## 3.3. Effect of inlet fuel concentration

Figure 7 depicts the impedance spectra at different inlet hydrogen concentrations. As shown by the Figure the gas conversion resistance ($R_g$) changes with inlet hydrogen

concentration variations. It is shown that minimum value of $R_g$ is at 50% of inlet hydrogen concentration. This is due to the fact that the gas concentration overvoltage (Eq. 5) is minimum at 50% inlet hydrogen concentration.

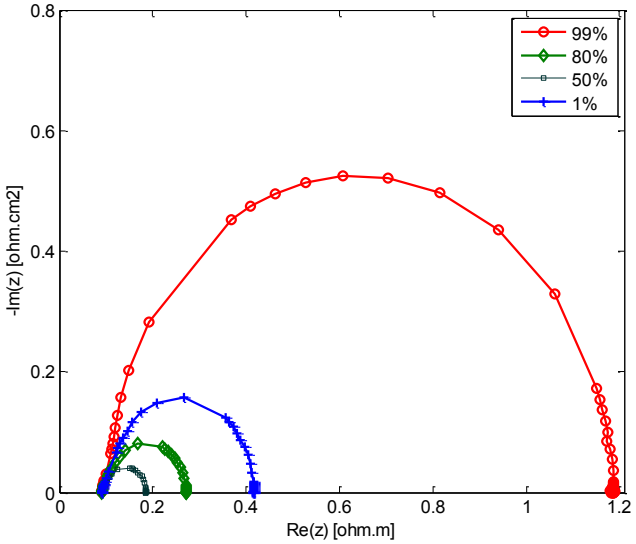


Figure 7: Electrochemical impedance spectra for different inlet fuel concentration

## 4. CONCLUSIONS

In this paper simulation and analyzing the electrochemical impedance spectra of a SOFC anode is considered. The electrochemical impedance spectra are obtained and it is found that the channel diffusion causes a capacitive behavior in the form of a RC-type semicircle in the nyquist diagram. This feature is related to concentration polarization. The simulations are in full qualitative and reasonable quantitative agreement with published data. Moreover, the developed code can be used as a suitable tool to optimize the operation of the fuel cell. Therefore, a parametric simulation study is also carried out and the effect of various parameters such as steady sate overvoltage, cell dimensions, and inlet fuel concentration on the gas conversion impedance is investigated and the results are discussed.

## References

[1] J. Larminie and A. Dicks, Fuel Cell Systems Explained, second ed., John Wiley & Sons, West Sussex, England, (2003).

[2] S.C. Singhal and K. Kendall, High-temperature solid oxide fuel cells: Fundamentals, design and application, Editors, Elsevier Science, Oxford, (2003).

[3] J.R. Macdonald, Impedance Spectroscopy - Theory Experiment and Application, John Wiley & Sons, New York, (2005).

[4] M. J. Verkerk and A. J. Burggraaf , Oxygen Transfer on Substituted ZrO2, Bi2O3, and CeO2 Electrolytes with Platinum Electrodes, J. Electrochem. Soc.130, 78–84, (1983)

[5] N. Wagner, W. Schnurnberger, B. Muller and M. Lang, Electrochemical impedance spectra of solid-oxide fuel cells and polymer membrane fuel cells, Electrochimica Acta, Vol. 43, No. 24, 3785-3793, (1998).

[6] S. Primdahl and M. Mogensen, Gas Conversion Impedance: A Test Geometry Effect in Characterization of Solid Oxide Fuel Cell Anodes, J. Electrochem. Soc. 145-7-2431, (1998).
[7] S. Primdahl and M. Mogensen, Gas Diffusion Impedance in Characterization of Solid Oxide Fuel Cell Anodes, J. Electrochem. Soc. 146-8-2827, (1999).
[8] A. Bieberle and L. Gauckler, State-space modeling of the anodic SOFC system Ni,H2–H2OYSZ, Solid State Ionics,146, 1-2, 23-41, (2002).
[9] W. Bessler, A new computational approach for SOFC impedance based on detailed electrochemical reaction-diffusion models, Solid State Ionics 176, 997-1011, (2005).
[10] W. Bessler, Gas concentration impedance of solid oxide fuel cell anodes. I. Stagnation point flow geometry, J. Electrochem. Soc. 153, A1492-A1504, (2006).
[11] W. G. Bessler and S. Gewies, Gas concentration impedance of solid oxide fuel cell anodes. II. Channel geometry, J. Electrochem. Soc. 154, B548-B559, (2007).
[12] T. Kato, K. Nozaki, et al., Impedance analysis of a disk-type SOFC using doped lanthanum gallate under power generation, J. Power Sources 133-169, (2004).
[13] K. Takano, S. Nagata, et al., Numerical simulation of a disk-type SOFC for impedance analysis under power generation, J. Power Sources 132 -42, (2004).
[14] A. Chaisantikulwat, C. Diaz-Goano, and E.S. Meadows, Dynamic modelling and control of planar anode-supported solid oxide fuel cell, J. Computers and Chemical Engineering 32, 2365–2381, (2008)

A1309 (Abstract)

# Kinetic Monte Carlo Simulation of Ion Conduction in Ydoped Barium Zirconate

**Rojana Pornprasertsuk, Onthida Kosasang, Kittichai Somroop and Friedrich B. Prinz**
Chulalongkorn University
Department of Materials Science, Faculty of Science
Phayathai Rd. Patumwan
Bangkok, 10330
Thailand
Tel.: +66-2-218-5547
Fax: +66-2-218-5561
rojana.p@chula.ac.th

## Abstract

Y-doped Barium Zirconate (BYZ) has been extensively studied for the proton-conducting ceramic fuel cell (PCFC) application due to its high proton conductivity and high chemical stability. However, most studies were performed experimentally with only few studies focusing on the ionic conduction mechanisms in atomic scale. Therefore, in this study, the quantum simulation complemented with kinetic Monte Carlo (KMC) method was employed to understand the ionic conduction and defect association mechanisms in BYZ. The quantum simulation based on density functional theory (DFT) was first used to create the migration energy barrier database and explore possible pathways for ion transport. The DFT calculation results reveal the effect of defect association among proton ($H_+$) oxide ion vacancy (V) and Y atom. The highest binding energy was -0.18 eV, corresponding to the attractive interaction of H and the first nearest neighbor Y atom. The defect association also affects both proton and oxide ion migration barriers causing the difference in the migration energy at different Y arrangements around the diffusion centers. The KMC simulations were then performed using Boltzmann probabilities based on the calculated DFT barriers to determine the effect of the doping concentration and the water uptake on the ionic conductivity of $Ba(Y_x,Zr_{1-x})O_{3-\square}$ supercell with x increasing from 0.08 to 0.4.The KMC simulation results show that proton conductivity is at least 2-3 orders of magnitude higher than oxide ion conductivity at all doping concentrations. The optimum doping concentration for the highest proton conductivity depends strongly on the amount of the water uptake. The results will be subsequently compared with the experimental results.

A1310

# A Parameter Estimation Method for Fuel Cell Diagnostics

**Leonidas Tsikonis, Stefan Diethelm, Arata Nakajo and Jan Van herle**
École Polytechnique Fédérale de Lausanne
Industrial Energy Systems Laboratory (LENI)
EPFL-STI-IGM-LENI
ME A2, Station 9
CH-1015 Lausanne,
Switzerland
Tel.: +41-21-693-3521
Fax: +41-21-693-3502
leonidas.tsikonis@epfl.ch

## Abstract

Researchers and developers typically use I-V curves (current vs. potential) as a means to demonstrate good data fitting of a model under experimental validation. Despite the popularity of this method, assessment of the results can be intuitive rather than mathematical, and usually, when such a demonstration occurs, information on the quality of the parameter estimation is not given. On the contrary, it has been shown that simple model fitting on I–V curves cannot give statistically reliable results on the values of the model parameters since the confidence intervals are quite high.

In previous work we used a model-based Design of Experiments method to establish optimal measurements on SOFC's, in order to improve the parameter estimation's reliability. Based on this theoretical analysis we proceeded to experimental validation with measurements on SOFC button cells. This work led to the development of a different method for sampling and treatment of data taken from I-V curves. This method facilitates production of histograms for each parameter –instead of simple values– allowing the researcher to observe their stochastic behaviour and assess the discrepancies of the calculated parameters. Furthermore the calculation of their variances and covariances are based on experimental data instead of the theoretical linear approach of the output model's partial derivatives with respect to the parameters.

In this work we present part of the produced results from this method using an advanced electrochemical and mass transport model for the cell.

The proposed method can be used as a tool to improve model validation procedures, for fuel cell diagnostic applications, research on degradation etc.

## Introduction

Polarisation (I–V) curves are used extensively to assess the performance of fuel cells. Their measurements are also used to calibrate electrochemical models ([1], [2]). The calibration process comprises the adaptation of parameters of mathematical models so that the models in question fit best the available data according to certain criteria such as least squares, maximum likelihood etc. However this approach does not allow the calculation of statistical measures –e.g. the parameters' standard deviations– because it is not repetitive. Thus for their calculation, approximate methods are employed based on the partial derivatives of the systems' outputs with respect to the parameters. Furthermore it has been shown that simple model fitting on I–V curves cannot give statistically reliable results on the values of the model parameters since the confidence intervals –calculated as above– are quite high [3].

Previous work on model-based Design of Experiments ([4], [5]) showed that repetitive measurements contribute to the improvement of the covariance matrices (matrices of which the diagonal elements are the parameters' variances and the off-diagonal are their covariances). After this theoretical investigation we pursued its experimental validation with measurements on button cells. The effort ended in the development of a sampling method which allows repetitive calculations of the model's parameters and consequently the calculation of statistics based on multiple parameter estimations rather than the model's derivatives. In this paper we present the method and a part of the relevant results.

The next Section 1 describes the proposed sampling method. In Section 2 we describe the experimental setup as well as the results from two experiments. We conclude with Section 3 with a summary and proposals for future work.

## 1. The Method

Let us assume that we want to take 12 measurements from a fuel cell, not necessarily optimal. By measurement we mean in this text the measurement of the cell's potential for a specific combination of gas inputs (in anode and cathode), temperature and current. One way to do it is by specifying 12 different conditions –after for example a Design of Experiments study– and apply them in the lab. However, this can be technically demanding. One other way to do it is by making 4 I–V measurements and selecting 3 points from each. The green arrows (pointing upwards) in Figure 26 are one example. If we suppose an error in the current or the voltage measurement (e.g. ±2mA, ±5mV etc.) then we can define zones on the polarisation curves where we can assume that points from the specific zones are repetitions of the same measurement. The vertical bars in Figure 26 define such zones. Therefore, another set of points, like the ones noted by the red arrows (pointing downwards) can be assumed that are repetition of the first set.

In a similar manner, using random number generators we can define a series of different combinations of points from the same curves, thus producing "pseudo-repetitive" measurements. Every individual measurement may be used for a different estimation of the fuel cell's parameters. Therefore, a set of repeated measurements leads to a set of repeated parameter estimations and consequently to the production of statistics for the parameters. The advantage of these statistics is that they are produced directly from the experimental data and not from linearization based on partial derivatives as it is usually done.

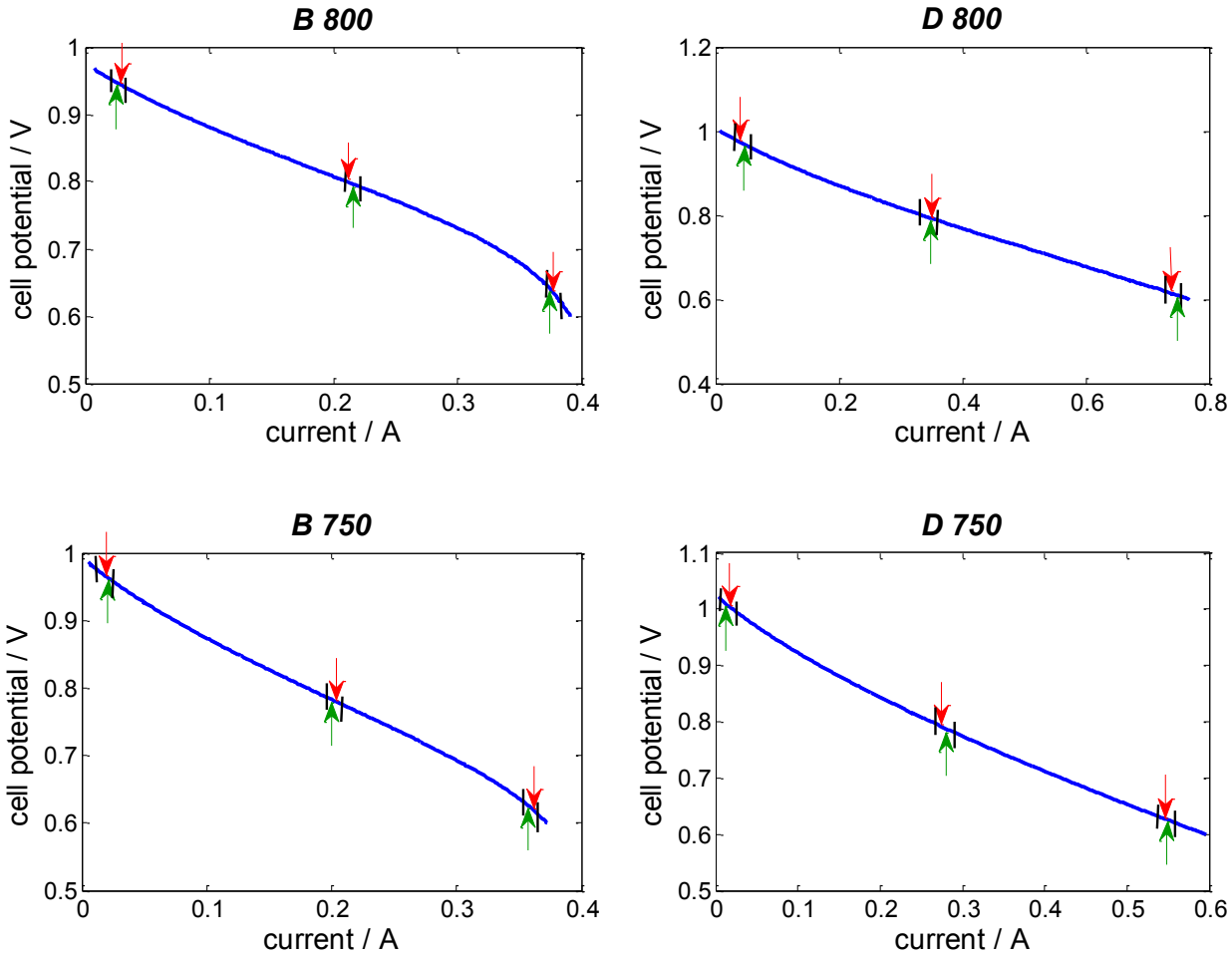


Figure 26. Four I–V (current vs. potential) curves, for different gas and temperature combinations. The data are real and the letters on the charts' titles refer to the gas compositions of Table 3. The numbers refer to the furnace temperature in ºC during the corresponding measurements. For two parameter estimations, twelve points from these curves have been selected twice (red, pointing downwards and green, pointing upwards). If a certain maximum error of measurement on the current is hypothesized (vertical bars) it may be assumed that the two colours correspond to the same set of measurements, repeated twice.

## 2. Application

In this paper we present an application of this method with measurements and parameter estimations from two different experiments. In the first case (experiment 0430, §2.2) 9 parameters were calculated after one series of measurements. In the second (experiments 0812-0813, §2.3) 6 parameters were calculated after two series of measurements, before and after an accidental fast degradation of a button cell.

The parameter estimation model was the same in both cases and it is presented in [1] and [2]. A short description is given in the Appendix of this article.

### 2.1. Experimental setup and measurements

The measurements were effectuated on button cells of 1.13 $cm^2$ active area, with LSM-YSZ cathode ([6], [7]), screen printed on a Ni-YSZ anode supported electrolyte provided by HTceramix. Each time, the cell is clamped on a Probostat™ setup (NorECs, Norway, Figure 27) and enclosed in a furnace. All electrochemical measurements were performed with an IM6 electrochemical workstation (Zahner, Germany) using a two electrodes configuration with four wires. I–V measurements were done under potentiostatic control (varying the potential and measuring the current) from OCV to 0.6 V with scans at a speed of 2 mV $s^{-1}$.

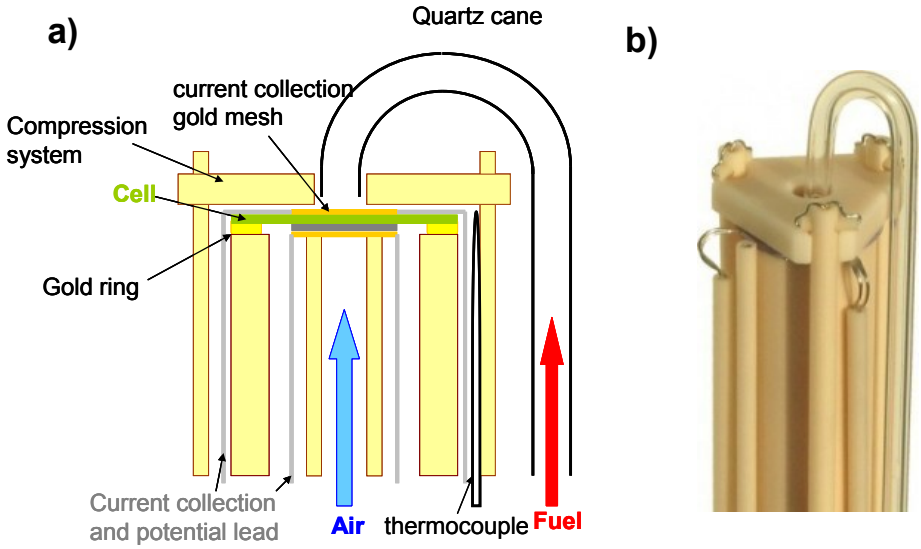


Figure 27. a) Schematic representation of the cell assembly in the Probostat™. b) Picture of the upper part of the assembly (courtesy of NorECs) [7].

Table 3 summarises the gas flow combinations used during the experiments. An effort was made to obtain a variety in hydrogen molar fraction and air ratios for a richer set of data. The measurements took place at three furnace temperatures: 800ºC, 750ºC and 700ºC.

Table 3. Anode gas compositions used during the experiments. The flow rate on the cathode was kept constant at 6.81e-5 mol $s^{-1}$ (100 ml $min^{-1}$).

| Gas mode | Flow rates / mol $s^{-1}$ (ml $min^{-1}$) | | air ratio | $x_{H_2}$ |
|---|---|---|---|---|
| | $H_2$ | $Ar$ | | |
| A | 6.81e-6 (10) | 3.41e-5 (50) | ~3 | 20 % |
| B | 1.43e-5 (21) | 3.34e-5 (49) | 2 | 30 % |
| C | 2.86e-5 (42) | 1.91e-5 (28) | 1 | 60 % |
| D | 2.86e-5 (42) | 6.81e-6 (10) | 1 | 80 % |
| E | 4.68e-5 (70) | 0 | 0.6 | 100 % |

### 2.2. Experiment 0430 – estimation of 9 parameters

We present in Table 4 the mean and best parameter values after 184 repeated parameter estimations effectuated for the first experiment. For the fit the least squares method was used and it was based on q = 80 points on the I–V curves, i.e. the total number of measurements was:

N = 80 x 5(gas combinations) x 3(temperatures) = 1200

The "mean" values are the arithmetic means of the 184 parameter values produced from the parameter estimations. "Best" are the sets of parameters that gave the best fit on the experimental data. As regards the results, the geometric active area was approached with an error of about 2.2%. Generally, the results are close to the reference values (taken from [2]) except for the pre-exponential factor for the activation overpotential on the cathode $k_{o,ca}$, and the ratio of porosity/tortuosity$^2$ ($\varepsilon/\xi^2$) on the anode. Especially for the second, assuming a porosity of 25.3% (after relevant measurements) leads to a tortuosity of about 5.6, a higher value than what is found in literature ($\xi \approx 1.5–4$, [1], [9]). With the available data we cannot infer whether the anode's tortuosity is indeed so high, or this parameter is adapted in order to cover phenomena that the mathematical model does not predict.

Table 4. Comparison of reference values with the calculated "mean" and "best" parameter values for experiment 0430.

| Calculated parameters | Values of reference | "Mean" values | "Best" values | units |
|---|---|---|---|---|
| $A_{cell}$ | 1.13e-4 (geometric) | 1.154e-4 | 1.163e-4 | $m^2$ |
| $E_{act,an}$ | 1.3111e5 | 1.311e5 | 1.311e5 | J $mol^{-1}$ |
| $k_{o,an}$ | 13.4572 | 12.99 | 13.09 | A $m^{-2}$ $K^{-1}$ |
| $E^*_{act,an}$ | 9.6e4 | 9.617e4 | 9.617e4 | J $mol^{-1}$ |
| $k^*_{o,an}$ | 2.1362e5 | 2.136e5 | 2.136e5 | – |
| $E_{act,ca}$ | 1.4019e5 | 1.399e5 | 1.399e5 | J $mol^{-1}$ |
| $k_{o,ca}$ | 0.149221 | 0.03359 | 0.03285 | A $m^{-2}$ $K^{-1}$ |
| $\varepsilon_{an}/\xi^2_{an}$ | 0.02315 | 0.008050 | 0.007999 | – |
| $E_{ion}$ | 1.1e5 | 1.096e5 | 1.096e5 | J $mol^{-1}$ |

The values of reference were used as initial values for the optimisations.

Figure 28 depicts the histograms of the estimated parameters. The reader may see that they do not follow a Normal distribution as it is usually assumed.

Figure 29 depicts the fit obtained with the mean parameter values. Higher deviations are observed for low hydrogen concentrations demonstrating the need to correct the part of the model related to gas diffusion. This is also evident in the last two rows where the concentration losses are not well followed either.

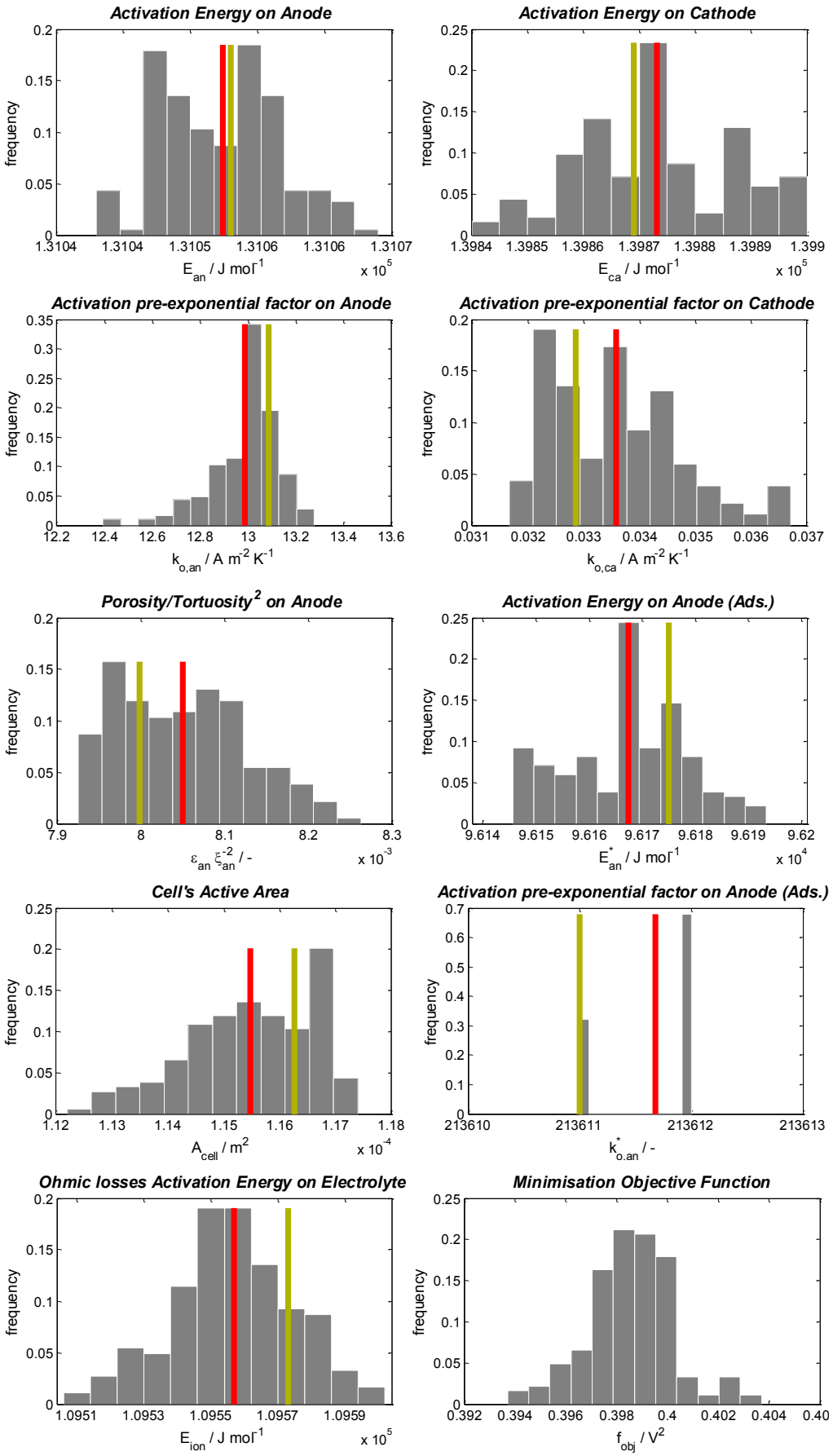


Figure 28. Histograms of identified parameters and the objective function from *r = 184* parameter estimations of *N = 1200* measurement points (*q = 80* points on the I–V curves) from experiment 0430. The red bar corresponds to the mean value of the parameter and the green to the "best" estimation.

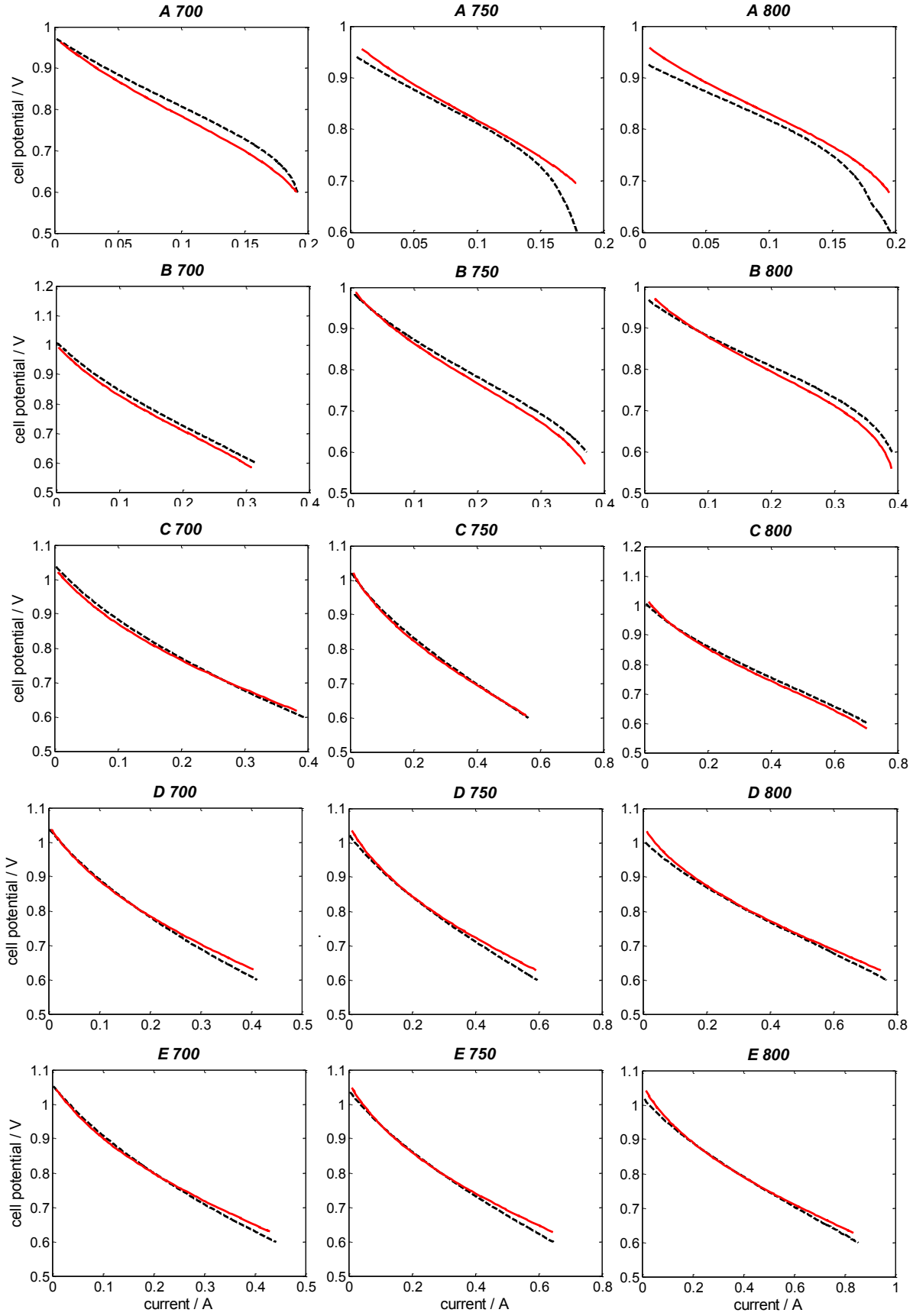


Figure 29. Experimental polarisation curves (black-dashed) for all gas compositions (Table 3) and all furnace temperatures vs. simulations with “mean” parameters (red-continuous) for the first experiment.

### 2.3. Experiment 0812-0813 – comparison of 6 parameters before and after degradation

For the data fit of the second experiment we did not use least squares method but the least modulus method (also known as L1 method), that is, we minimised the sum of the absolute differences between measurements and simulation instead of their squares. This is a considerably slower approach but has the advantage of being less affected by outliers in the available data [10]. Such a choice was necessary due to high oscillations in the measurements after the cell's degradation (Figure 31). The number of repetitions were this time $r = 25$, because of the slow convergence of the applied method.

The degradation occurred within 12 hours, under constant polarisation at 0.6 V at 800°C, and 20 ml $min^{-1}$ hydrogen and 30 ml $min^{-1}$ argon to the anode. The cathode was fed with 100 ml $min^{-1}$ air like in all cases.

Figure 30 depicts the fit of the model on the first series of measurements before degradation. There seems to be a better fit than the first experiment (Figure 29). In all diagrams, there is a deviation at low currents, showing a possible inability of the model to reproduce the activation losses.

Similar conclusions may be made for the curves after degradation (Figure 31). In addition to them, the oscillations on the current show a malfunction of the cell that the used model does not predict. Using the L1 method we managed to reduce the influence of the outliers (points away from the main curve) and follow the principal trend of the measurements.

The results in Table 5 enhance the doubts as to whether the model reproduces correctly the behaviour of the cell. Even before degradation the pre-exponential factor for the anode's activation overpotential $k_{o,an}$, is two orders of magnitudes higher than the reference value, and the activation energy for the cathode's activation overpotential $E_{act,ca}$, is half of it.

Table 5. Comparison of reference values with the calculated mean parameter values for experiments 0812-0813.

| Calculated parameters | Values of reference | Parameters before degradation (st. deviation) | Parameters after degradation (st. deviation) | units |
|---|---|---|---|---|
| $E_{act,an}$ | 1.3111e5 | 1.2306e5 (1.157e3) | 1.265e5 (242.5) | J $mol^{-1}$ |
| $k_{o,an}$ | 13.4572 | 2324 (458,2) | 4122 (61.24) | A $m^{-2}$ $K^{-1}$ |
| $E_{act,ca}$ | 1.4019e5 | 72695 (339,3) | 216.89 (107.92) | J $mol^{-1}$ |
| $k_{o,ca}$ | 0.1492 | 0.2264 (0.0019) | 0.4644 (0.0029) | A $m^{-2}$ $K^{-1}$ |
| $\varepsilon_{an}/\xi^2_{an}$ | 0.02315 | 0.0611 (0.0004) | 0.0762 (0.0008) | – |
| $E_{ion}$ | 1.1e5 | 1.1788e5 (18.2) | 1.2016e5 (23.8) | J $mol^{-1}$ |

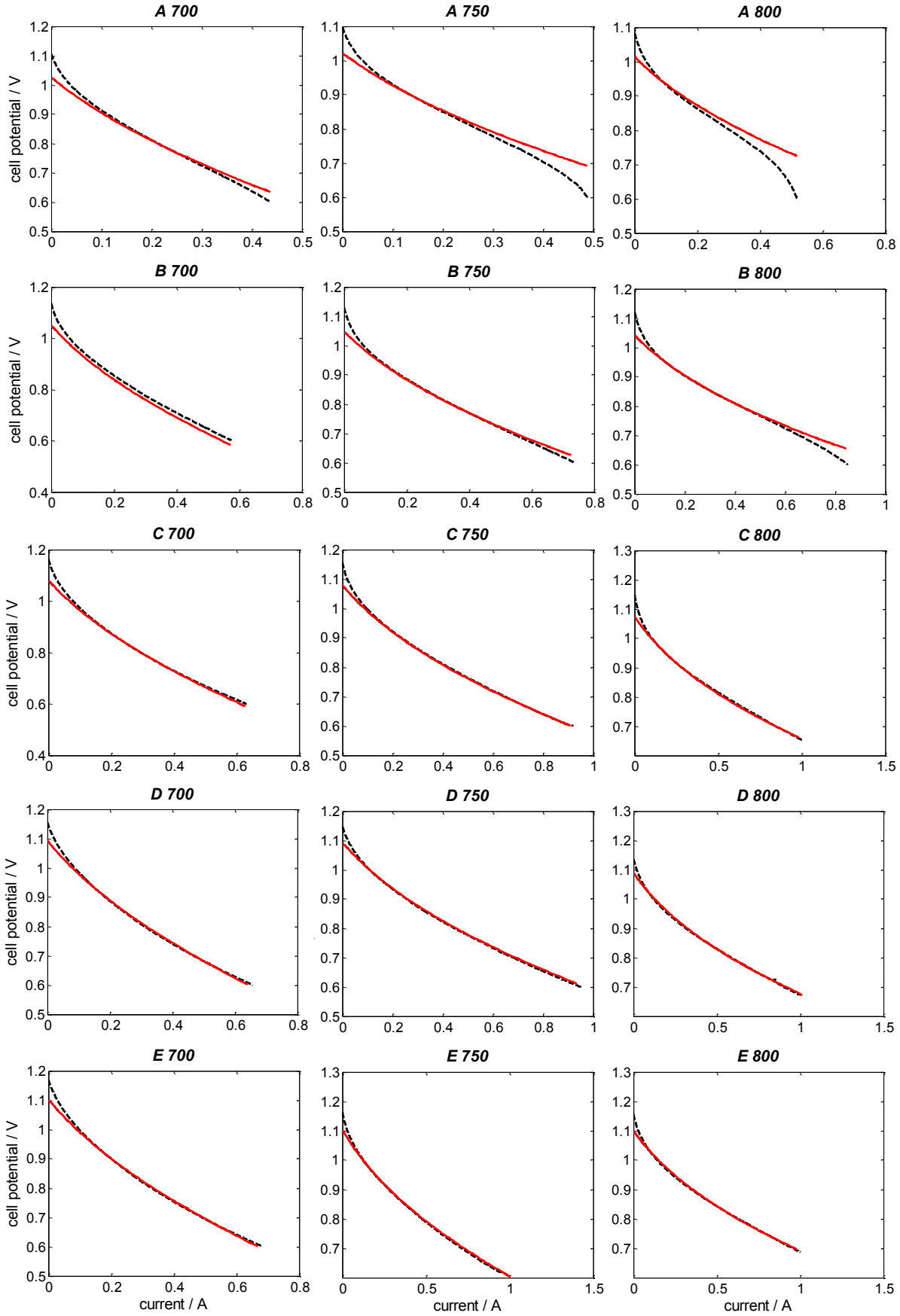


Figure 30. Experimental polarisation curves (black-dashed) for all gas compositions (Table 3) and all furnace temperatures vs. simulations with “mean” parameters (red-continuous) for the second experiment before degradation.

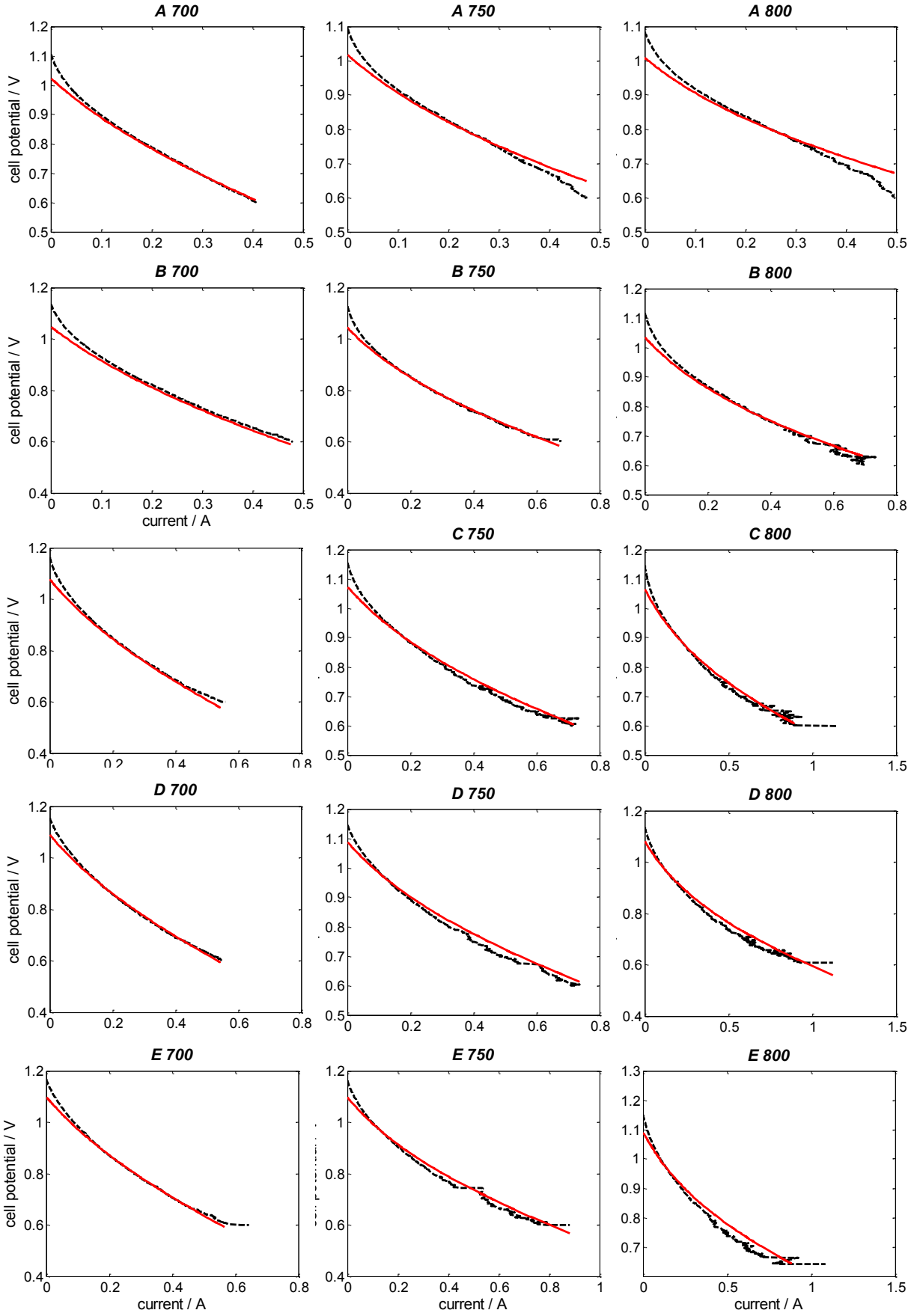


Figure 31. Experimental polarisation curves (black-dashed) for all gas compositions (Table 3) and all furnace temperatures vs. simulations with “mean” parameters (red-continuous) for the second experiment after degradation.

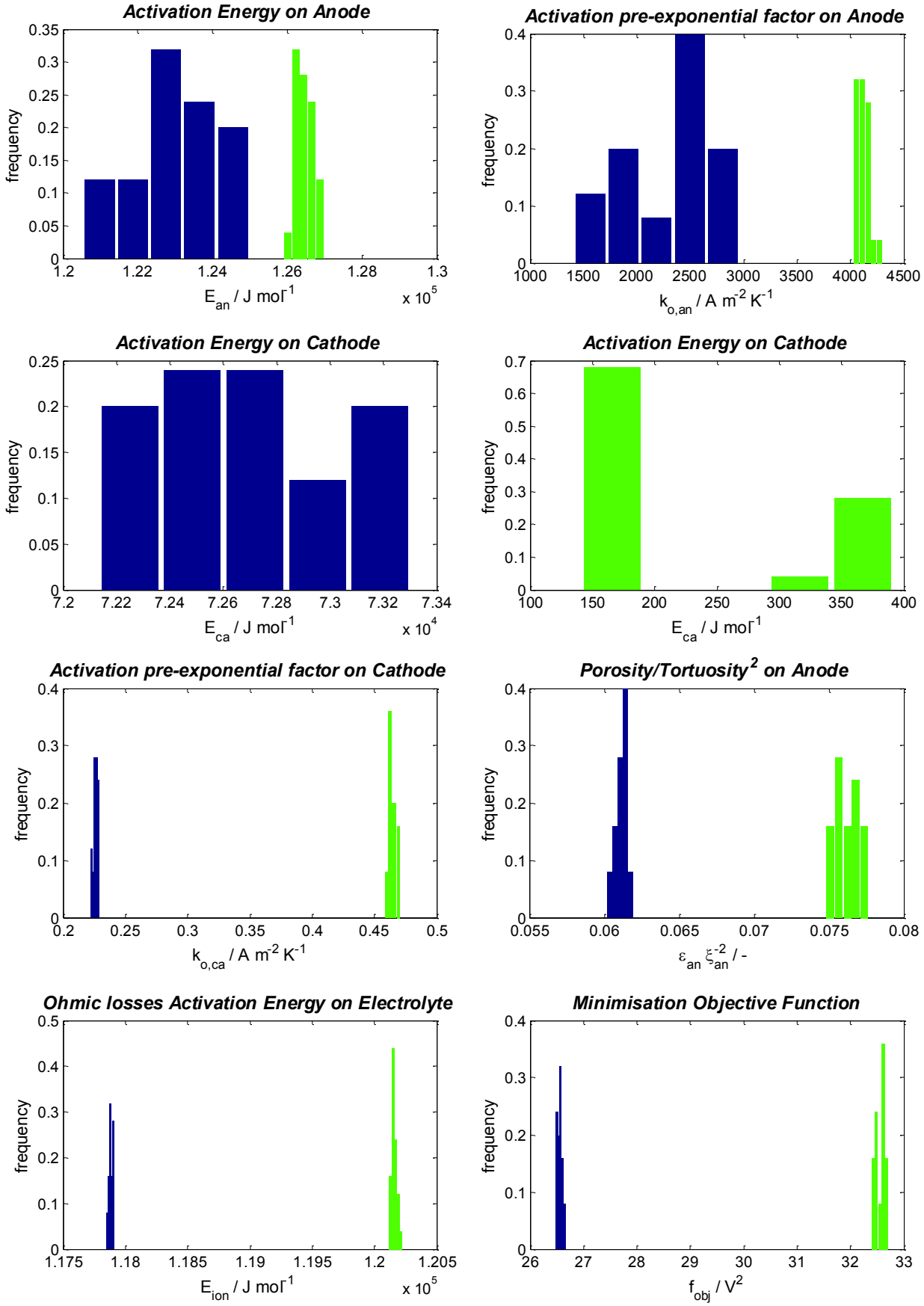


Figure 32. Comparison of histograms (blue/dark bars before degradation – green/light bars after degradation) of identified parameters and the objective function from experiments 0812-0813. *r = 25* parameter estimations were effectuated at *N = 1800* measurement points (*q = 120* points on the I–V curves). The results for $E_{act,ca}$ could not be shown in the same graph.

Figure 32 compares the histograms of the calculated parameters. As regards them, we can make the following notes:

- Although the current histograms provide information on the stochastic behaviour of the parameters, more repetitions are necessary to improve their quality.
- The parameters are statistically different before and after the cell's degradation.
- The anode activation energy ($E_{an}$) and the activation pre-exponential factor $k_{o,an}$ both increase, showing a higher dependency of the activation on the temperature.
- Similarly the ratio porosity/tortuosity$^2$ increases. This may be connected to an augmentation of the anode's porosity or a decrease of its tortuosity.
- Except for the change of their mean values, the parameters related to activation energy in the anode have smaller standard deviations compared to the initial state. Furthermore, the shapes of $E_{an}$ and $\varepsilon/\xi^2$ histograms change. These are indications that the current model has a different interaction with the experimentally produced data. Apparently the employed model is insufficient to reproduce the behaviour of the cell and a more comprehensive one is necessary.

## 3. Conclusion

We introduce a parameter estimation method from polarisation (I–V) curves with which the researcher obtains the stochastic behaviour of the sought parameters. This is done in a alternative manner based on experimental values rather than the usual linearised method based on partial derivatives. We apply the method on two different cases of button cells, the second of which was accidentally fast degraded. The obtained histograms show that the parameters do not follow a Normal probability distribution as is usually assumed. As regards the degraded cell, we were in position to infer whether the parameters are statistically different before and after the phenomenon. However, observations on the fuel cells' parameters and changes thereof depend strongly on the quality of the employed model. If it does not reproduce phenomena correctly, then it may give misleading results. Further investigation is required on the method in order to conclude on its advantages and its limitations.

## Acknowledgements

The research was funded by Swisselectric Research and the Swiss Federal Office of Energy under the SOF-CH1 contract. Calculations ran in Pleiades cluster in EPFL [11].

## References

[1] A. Nakajo, Z. Wuillemin, P. Metzger, S. Diethelm, G. Schiller, J. Van herle and D. Favrat, *Electrochemical model of solid oxide fuel cell for simulation at the stack scale. Part I: Calibration procedure on experimental data*, Manuscript submitted to the Journal of The Electrochemical Society

[2] A. Nakajo, *Thermomechanical and Electrochemical Degradation in Anode-Supported Solid Oxide Fuel Cell Stacks*, PhD Thesis no. 4930, EPFL, Lausanne, Switzerland, 2010.

[3] D. Larrain, *Solid Oxide Fuel Cell Stack Simulation and Optimisation, Including Experimental Validation and Transient Behavior*, PhD Thesis no. 3275, EPFL, Lausanne, Switzerland, 2005.
[4] L. Tsikonis and J. Van herle, *A Design of Experiments based method for the Characterisation of Solid Oxide Fuel Cells*, presentation in the 7th Symposium on Fuel Cell Modeling and Experimental Validation (MODVAL7), 23-24 March 2010, Morges – Switzerland, book of Abstracts pp. 62.
[5] L. Tsikonis, J. Van herle and D. Favrat, *Investigating Reliability on Fuel Cell Identification. Part I: A Design of Experiments Approach*, submitted for publication.
[6] P. Tanasini, M. Cannarozzo, P. Costamagna, A. Faes, J. VanHerle, A. Hessler-Wyser, and C. Comninellis, *Experimental and Theoretical Investigation of Degradation Mechanisms by Particle Coarsening in SOFC Electrodes*, Fuel Cells 2009, 9, No. 5, 740–752
[7] S. Diethelm, J. Van herle, *Ethanol internal steam reforming in intermediate temperature solid oxide fuel cell*, J Power Sources (2010), article in press. doi:10.1016/j.jpowsour.2010.11.063.
[8] http://www.norecs.com/index.php?page=141
[9] C.-L. Tsai and V.H. Schmidt, *Tortuosity in anode-supported proton conductive solid oxide fuel cell found from current flow rates and dusty-gas model*, J Power Sources 196 (2011) 692–699
[10] É. Walter and L. Pronzato, *Identification of Parametric Models from Experimental Data*, Springer Verlag, London, 1997.
[11] http://pleiades.epfl.ch/

## Appendix

The cell's potential is:

$$U_{cell} = E_{Nernst} - U_{act,an} - U_{act,ca} - U_{ion}$$

**Nernst potential**

The Nernst potential is given by:

$$E_{Nernst} = -\frac{\Delta G}{2F} - \frac{R \cdot T}{2F} ln\left[\frac{x_{H_2O,an}}{x_{H_2,an} \cdot x_{O_2,ca}^{0.5}}\right]$$

The molar fractions for the hydrogen, oxygen and water vapours are calculated using Fick's diffusion law for the cathode:

$$\mathcal{M}_i = \rho \cdot \mathcal{D}_{i-mix,eff} \cdot \nabla m_i$$

and dusty gas model for the anode:

$$\sum_{j,j\neq i} \frac{x_j \mathcal{N}_i - x_i \mathcal{N}_j}{\mathcal{D}_{i,j,eff}} + \frac{\mathcal{N}_i}{\mathcal{D}_{i,K,eff}} = -\frac{1}{RT}\left(\frac{d\left(x_i p_{an}\right)}{dz} + \frac{B_o x_i p_{an}}{\mathcal{D}_{i,K,eff} \cdot \mu}\frac{dp_{an}}{dz}\right)$$

with:

$$\mathcal{D}_{i,j,eff} = \frac{\varepsilon}{\xi^2}\mathcal{D}_{i,j}$$

$$\mathcal{D}_{i,K,eff} = \frac{\varepsilon}{\xi^2}\mathcal{D}_{i,K} = \frac{\varepsilon}{\xi^2}\frac{d_p}{3}\sqrt{\frac{8RT}{\pi M_i}}$$

$$\mathcal{N}_i = \frac{i}{2F}$$

$$B_o = \frac{d_p^2}{180}\frac{\varepsilon_{an}^2}{(1-\varepsilon_{an})^2}$$

**Activation overpotential on the anode**

The anode activation overpotential is calculated from the implicit functions:

$$i_{an} = \xi_{TPB,an}\cdot i_{o,an}\frac{\left(\frac{x_{H_2}}{x^*_{H_2}}\right)^{1/4} x^{3/4}_{H_2O}}{1+\left(\frac{x_{H_2}}{x^*_{H_2}}\right)^{1/2}}\left[exp\left(\frac{1}{2}\frac{F}{RT}U_{act,an}\right)-exp\left(-\frac{3}{2}\frac{F}{RT}U_{act,an}\right)\right]$$

$$i_{o,an} = T\cdot k_{o,an}\cdot exp\left[-\frac{E_{act,an}}{R}\left(\frac{1}{T}-\frac{1}{T_{ref}}\right)\right]$$

$$x^*_{H_2} = k^*_{o,an}\cdot exp\left(-\frac{E^*_{act,an}}{RT}\right)$$

**Activation overpotential on the cathode**

Similarly the cathode activation overpotential is:

$$i_{ca} = i_{o,ca}\frac{\left(\frac{x_{O_2}}{x^*_{O_2}}\right)^{3/8}}{1+\left(\frac{x_{O_2}}{x^*_{O_2}}\right)^{1/2}}\left[exp\left(-\frac{1}{2}\frac{F}{RT}U_{act,an}\right)-exp\left(\frac{3}{2}\frac{F}{RT}U_{act,an}\right)\right]$$

$$i_{o,ca} = T\cdot k_{o,ca}\cdot exp\left[-\frac{E_{act,ca}}{R}\left(\frac{1}{T}-\frac{1}{T_{ref}}\right)\right]$$

$$x^*_{O_2} = k^*_{o,ca}\cdot exp\left(-\frac{E^*_{act,ca}}{RT}\right)$$

**Ohmic overpotential on the electrolyte**

It is:

$$U_{ion} = i\cdot\left[\frac{d_{elec}}{\sigma_{o,ion}}+\frac{l_g}{\sigma_{o,ion}}\left(\frac{l_g/d_g-1}{d_g/l_g+1}\right)\right]$$

$$\sigma_{o,ion} = \frac{k_{o,ion}}{T}exp\left(-\frac{E_{ion}}{R\cdot T}\right)$$

The following table summarises the values of parameters used in the equations above.

| parameter | value of reference | unit |
|---|---|---|
| $d_p$ | 6.978e-7 | m |
| $\varepsilon_{an}$ | 0.309 | – |
| $\xi_{an}$ | 3.6538 | – |
| $\varepsilon_{ca}$ | 0.42 | – |
| $\xi_{ca}$ | 3 | – |
| $l_g$ | 9e-7 | m |
| $d_g$ | 1e-7 | m |
| $\xi_{TPB,an}$ | 1 | – |
| $E_{act,an}$ | 1.3111e5 | J $mol^{-1}$ |
| $k_{o,an}$ | 13.4572 | A $m^{-2}$ $K^{-1}$ |
| $E^*_{act,an}$ | 9.6e4 | J $mol^{-1}$ |
| $k^*_{o,an}$ | 2.1362e5 | – |
| $E_{act,ca}$ | 1.4019e5 | J $mol^{-1}$ |
| $k_{o,ca}$ | 0.149221 | A $m^{-2}$ $K^{-1}$ |
| $E^*_{act,ca}$ | 1.86e5 | J $mol^{-1}$ |
| $k^*_{o,ca}$ | 3.33E9 | – |
| $E_{ion}$ | 1.1e5 | J $mol^{-1}$ |
| $k_{o,ion}$ | 7.92E8 | Ohm$^{-1}$ $m^{-1}$ K |
| $T_{ref}$ | 873 | K |

A1311

# Multiphysics Model of the Anode of a Direct Methanol Fuel Cell

**P. A. García-Salaberri, M. Vera, I. Iglesias and R. Zaera**
Universidad Carlos III de Madrid
Avda. de la Universidad, 30
28911 Leganés, Spain
Tel.: +34-91-6249987
Fax: +34-91-6249430
pagsalab@ing.uc3m.es

## Abstract

A multiphysics across-the-channel model is presented for the anode of a liquid-feed Direct Methanol Fuel Cell (DMFC). The model considers both two-dimensional (2D) single-phase anisotropic transport of methanol in the anode gas diffusion layer (GDL) and anisotropic electron transport from the catalyst layer to the current collector rib, coupled to a one-dimensional (1D) model for the membrane and the cathode, which describes the electrochemical reactions kinetics, water and methanol crossover, and oxygen transport from the cathode channel to the cathode catalyst layer. As new contribution, the 2D model takes into account the effects of the inhomogeneous compression of the GDL associated with the repetitive rib-channel pattern, including non-uniform porosity, diffusivity and bulk electrical conductivity distributions, as well as non-uniform contact resistances over the GDL-rib and -membrane interfaces, which affect mass and charge transport phenomena. As a straightforward application, we have investigated the effect of the clamping pressure acting on the stack on the overall fuel cell performance.

# Introduction

Direct Methanol Fuel Cells (DMFCs) are electrochemical devices that convert the chemical energy of methanol and oxygen directly into electricity and heat [1]. The electrochemical reactions are facilitated by the presence of noble metal catalysts, so that no conventional high-temperature combustion processes occur in the cell. This substantially reduces the emissions of air pollutants and results in a more energetically efficient process due to the lack of any thermodynamic efficiency limit. DMFCs have two advantages over conventional Proton Exchange Membrane Fuel Cells (PEMFCs) operating with hydrogen, namely the ease of handling and storage of methanol and its higher volumetric energy density, which make them a potential substitute to conventional power sources for portable applications [2]. Nevertheless, DMFCs suffer from two fundamental problems: (i) the slow kinetics of the methanol electro-oxidation reaction and (ii) the ability of methanol to permeate through the polymer membrane crossing from anode to cathode (methanol crossover) [3]. In addition, there are common problems affecting both DMFCs and PEMFCs, such as water/gas/heat management, flow-field design and optimization, contact resistances at the GDL interfaces and multiphase mass transport phenomena that still need a better understanding.

The key component of a PEM fuel cell (both PEMFCs and DMFCs) consists of a five-layered structure, called the membrane electrode assembly (MEA), which is formed by a polymer electrolyte membrane (PEM) with a thin layer of catalyst on both sides, and a porous gas diffusion layer (GDL) in contact with each of the catalyst layers (CL) [4]. The MEA is further sandwiched between the bipolar plates (BP), which supply reactants to and remove products (and heat) from the active areas, act as current collectors, and provide mechanical support for the cells in the stack [5]. In DMFCs methanol is oxidized in the anode catalyst layer to form $CO_2$, protons, and electrons. The protons are transported through the PEM membrane to the cathode where they react with the oxygen and the electrons, which are evacuated by the anode GDL to the current collectors and flow through an external circuit providing electrical power. In this process, water is consumed at the anode and is produced in the cathode (see Fig. 1).

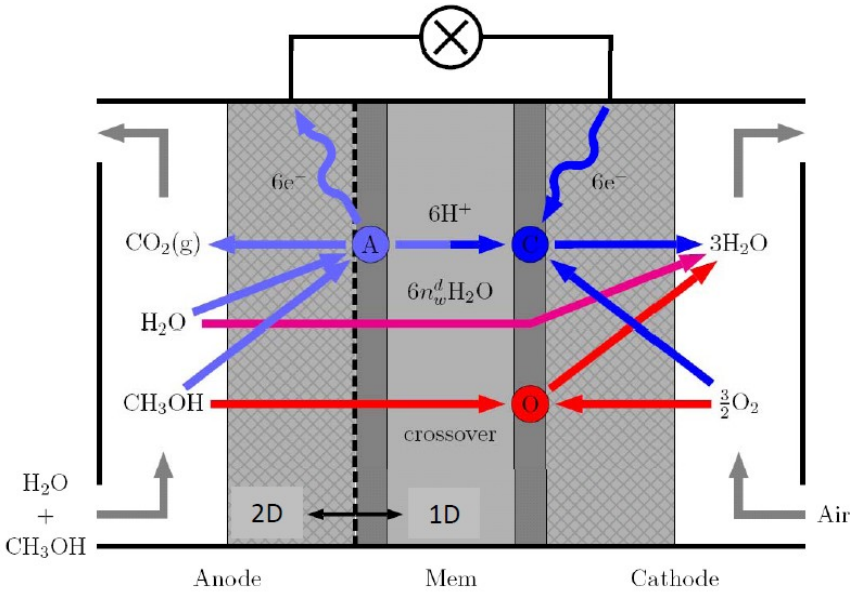


Fig. 1: Operating sketch of a DMFC, indicating the physical domains of the 2D/1D model.

One of the critical elements affecting the performance of PEM fuel cells is the GDL, which provides several functions during fuel cell operation: a passage for reactants access and excess products removal to and from the catalytic electrodes, high electronic and thermal conductivity, and adequate mechanical support for the MEA. In order to fulfill these requirements, GDLs are typically made of highly porous carbon-fiber paper, or cloth [6]. The high porosity of these materials provides to the GDL a characteristic soft and flexible structure which is susceptible of large deformations when subjected to compression, thus leading to significant modifications of its mechanical, thermal and electrical properties (thickness, porosity, permeability, thermal and electrical bulk conductivities and contact resistances, etc.) thus affecting mass, heat, and charge transport processes, fuel cell performance, and lifetime [7]. GDL compression occurs during the assembly/disassembly process of the stack [8], but also during cell operation due to membrane swelling [9]. Moreover, the repetitive rib-channel pattern of the bipolar plates results in a highly inhomogeneous compression load, which leads to spatially non-uniform GDL thickness and porosity distributions, as well as non-uniform electrical [10] and thermal [11] bulk conductivities and contact resistances (both at the rib-GDL and membrane-GDL interfaces). Thus, while large strains are produced under the rib, typically between 10-50% of the initial thickness [12], the region under the channels remains approximately at its initial uncompressed state.

The inhomogeneous compression of the GDL leads to several opposing effects. On one side, increasing the assembly pressure enhances electric and thermal conductivities by reducing bulk and contact resistances. Slight compressions may also reduce the mass transport resistance due to the shortening of the diffusion path to be covered by the reactants and products in their way to and from the catalyst layers. Nevertheless, excessive compression loads may impede reactant and product transport due to the loss of pore volume, which goes hand by hand with a reduction of the effective diffusivity coefficients of the chemical species. Moreover, excessive assembly pressures may damage typical paper type GDLs, induce local delamination of the GDL under the channel, and result in non-uniform compressive loads which may damage the membrane. Pore size reduction may also affect multiphase capillary transport phenomena in the GDL (i.e., liquid water removal in PEMFCs [13] and gaseous $CO_2$ transport in DMFCs [3]). Finally, partial intrusion of the GDL into the channel leads to a reactant flow rate reduction, or, alternatively, an increase of the parasitic power required to maintain the flow, thus affecting the overall efficiency of the stack.

In this paper, a multiphysics, isothermal, single-phase 2D/1D model for the anode of a liquid-feed direct methanol fuel cell (DMFC) is presented. The model takes into account the anisotropic nature of the GDL, and the effects of the inhomogeneous compression associated with the repetitive rib-channel pattern, including the non-uniform electric contact resistance distributions at the GDL interfaces. Two-dimensional (2D) mass, momentum and species transport in the anode gas diffusion layer is modeled using a commercial, finite-volume based, computational fluid dynamics (CFD) software, FLUENT® 12.1.4, complemented with user supplied subroutines. The 2D model is locally coupled to a one-dimensional (1D) model accounting for the electrochemical reactions in both the anode and the cathode, which provides a physically sound boundary condition for the velocity and methanol concentration fields at the anode gas diffusion layer/catalyst layer interface. The 1D model comprising the MEA, cathode gas diffusion layer, and cathode channel assumes non-Tafel kinetics to describe the complex kinetics of the multi-step methanol oxidation at the anode, and accounts for the mixed potential associated with methanol crossover, induced both by diffusion and electro-osmotic drag.

To account for the inhomogenous compression effects, a finite element method (FEM) model which fully incorporates the nonlinear orthotropic mechanical properties of the GDL has been developed in ABAQUS® 6.5.4. The model allows to calculate the porosity distribution in the GDL, and the contact pressure at the rib/GDL and membrane/GDL interfaces. From the porosity field and the contact pressure profiles, the effective bulk electrical conductivity field, the effective diffusivity field, and the contact resistance profiles are calculated through empirical correlations obtained from the open literature.

# 1. Modeling Approach

## 1.1. Model assumptions and cell geometry

The model assumptions are as follows: i) Single-phase, laminar, steady and isothermal flow, ii) The reactant concentrations are constant across the thickness of the anode and cathode catalyst layers, iii) The concentration of methanol is sufficiently small in the anode for the liquid phase to be a diluted methanol aqueous solution, iv) The membrane (Nafion® 117) is fully hydrated and is impermeable to gases, v) The methanol crossover is completely oxidized at the cathode catalyst layer, vi) The effect of buoyancy in methanol transport is neglected, vii) The pressure gradient across the different cell layers is neglected, viii) Ohmic losses in bipolar plates are neglected and ix) The voltage drop through the gas diffusion layer and its interfaces is equal in the anode and the cathode.

The cell geometry is shown in Fig. 2. We assume a parallel channel geometry for the anode current collector. Accordingly, we use symmetry boundary conditions at the channel/rib mid-planes to reduce the computational cost.

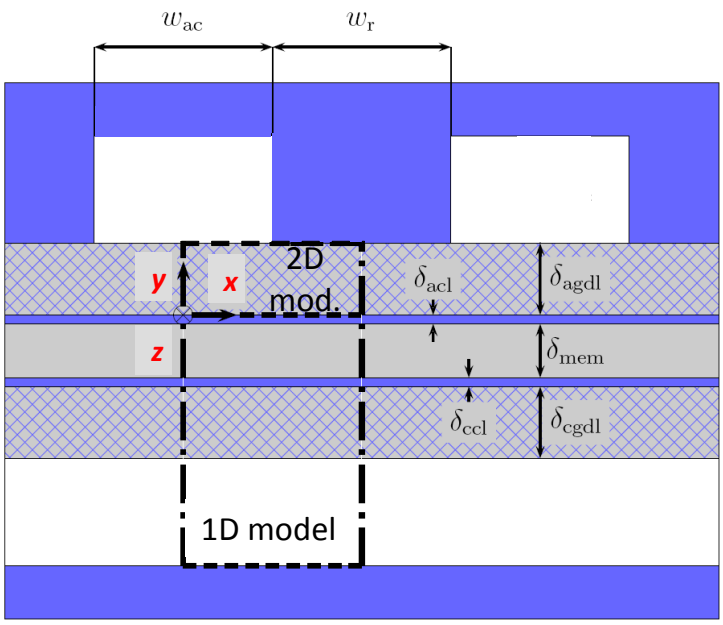


Fig. 2: Cross sectional geometry of the cell, indicating the computational domains for the 2D and 1D model. The analysis of flow in the cathode is omitted by introducing an overall mass transport coefficient $\alpha_2$. The geometric parameters are $\delta_{agdl} = \delta_{cgdl} = 190$ µm (Toray® TGP-H-060 [14]), $\delta_{acl} = \delta_{ccl} = 23$ µm, $\delta_{mem} = 185$ µm, $w_{ac} = 1$ mm and $w_r = 1$mm.

### 1.2. 2D model (anode gas diffusion layer)

The model presented in this section is a generalization of the model proposed in [15], which has been extended to include the transport of $CO_2$ and electrons in the anode gas diffusion layer, non-uniform contact resistances at the GDL-rib and -membrane interfaces and non-uniform porosity, effective diffusivities and effective electrical conductivities in the anode gas diffusion layer. The non-uniformity and anisotropy of the permeability have not been considered since the influence of the convective flux is negligible compared to the diffusive flux in DMFCs [16].

The conservation equations for the flow field ($u$, $p$), mass transport of species (methanol, $m$, and carbon dioxide, $CO_2$), and electric potential ($\varphi_e$) in the anodic GDL are:

$$\nabla \cdot u = 0\,,\ \frac{\rho}{\phi^2}(u\cdot\nabla)u = -\nabla p + \frac{\mu}{\phi}\nabla^2 u - \frac{\mu}{K}u \qquad \text{(1a,b)}$$

$$\nabla \cdot (\rho u C_i) = \nabla \cdot (\rho D_i^{eff} \nabla C_i) \quad i = m, CO_2 \qquad \text{(1c)}$$

$$\nabla \cdot (-\sigma^{eff}\ \nabla \varphi_e) = 0 \qquad \text{(1d)}$$

where $u$ denotes the superficial velocity in the porous media, $p$ the pressure, $C_i$ the molar concentration of species $I$ and $\varphi_e$ the electric potential in the anode gas diffusion layer. The physical properties involved in the equations are the porosity, $\Phi$, the density, $\rho$, the dynamic viscosity, $\mu$, the permeability, $K$, the effective coefficient of diffusion of species $i$, $D_i^{eff}$, and the effective electrical conductivity, $\sigma^{eff}$.

Equations (1a,b), (1c) and (1d) must be integrated supplemented with appropriate conditions on the boundaries of the 2D domain. In addition to the symmetry boundary conditions at the channel/rib mid-planes, at the channel/GDL interface we impose Dirichlet boundary conditions for the pressure and the concentration of species ($p$ = 0 Pa, $C_m$ = 0.3 M, $C_{CO_2}$ = 0 M) and no flux condition for the electric potential. On the other hand, at the non-permeable rib/GDL interface ($u$ = 0 and no flux of species) we set the voltage drop due to the rib/GDL contact resistance as

$$\sigma^{eff}\nabla\varphi_e\big|_{y=\delta_{agdl}} \cdot n = \frac{\varphi_e\big|_{y=\delta_{agdl}}}{R_{rib/GDL}} \qquad (2)$$

where $n$ is the outward normal and $R_{rib/GDL}$ the contact resistance at the rib/GDL interface. Note that the (equipotential) surface of the rib is taken as reference for the electric potential ($\varphi_e = 0$).

Finally, we impose the boundary conditions at the anode gas diffusion layer/catalyst layer interface. Here we prescribe the fluid velocity, the molar flux of methanol and $CO_2$, and the current density at the anode gas diffusion layer/catalyst layer interface:

$$u\big|_{y=0} \cdot n = (1 + 6n_d^w)\frac{i}{6F}\frac{W_w}{\rho} \qquad \text{(3a)}$$

$$(uC_m - D_m^{eff}\nabla C_m)_{y=0} \cdot n = N_m \qquad \text{(3b)}$$

$$(uC_{CO_2} - D_{CO_2}^{eff}\nabla C_{CO_2})_{y=0} \cdot n = -N_{CO_2} \qquad \text{(3c)}$$

$$\sigma\nabla\varphi_e\big|_{y=0} \cdot n = i \qquad \text{(3d)}$$

where $F$ is Faraday's constant, $n_d^w$ the coefficient of electro-osmotic drag of water and $Ww$ the molecular weight of water.

Once the local concentration of methanol in the catalyst layer, $Cm,acl \equiv C_m|_{y=0}$, and the cell voltage, $V$, are known, the 1D model presented below allows to calculate the local current density, $i$, the molar flow of methanol that reaches the catalyst layer, $N_m$, and the molar flux of $CO_2$ out of it, $N_{CO_2}$, which closes the mathematical problem.

### 1.3. 1D model (MEA and cathode)

The 1D model consists of 7 equations:

$$N_{O_2} = \alpha_2 (C_{O_2,amb} - C_{O_2,ccl}) \tag{4}$$

$$i + 6FN_{cross} = \delta_{ccl} (ai_0)_c \frac{C_{O_2,ccl}}{C_{O_2,ref}} \exp\left[\frac{\alpha_c F}{RT}\eta_c\right] \tag{5}$$

$$i = \delta_{acl} (ai_0)_a \frac{kC_{m,acl} \exp\left[\frac{\alpha_a F}{RT}\eta_a\right]}{C_{m,acl} + \lambda \exp\left[\frac{\alpha_a F}{RT}\eta_a\right]} \tag{6}$$

$$N_{cross} = 6n_d{}^m \frac{i}{6F} + D^{eff}_{m,mem} \frac{C_{m,acl}}{\delta_{mem}} \tag{7}$$

$$N_m = \frac{i}{6F} + N_{cross}, \; N_{CO_2} = \frac{i}{6F} \tag{8a,b}$$

$$N_{O_2} = \frac{1}{4F} i + \frac{3}{2} N_{cross} \tag{9}$$

where $ai_0$ is the product of the specific area of catalyst ($m^{-1}$) by the exchange current density, in general different for the anodic and cathodic reactions, $k$ and $\lambda$ are two experimental constants and $n_d{}^m$ is the electro-osmotic drag coefficient of methanol. Equation (4) models the convective-diffusive transport of oxygen from the ambient (*amb*) to the cathode catalyst layer (*ccl*) by a global coefficient of mass transport $\alpha_2$, (5) and (6) represent the kinetics of cathodic and anodic reactions [3,17], (7) expresses the molar flux of methanol crossover as the sum of electro-osmotic drag and molecular diffusion, and (8a,b) and (9) are the mass balances in the anode catalyst layers (methanol and $CO_2$) and the cathode ($O_2$), respectively.

Due to the methanol crossover in a DMFC the cathodic reaction (5) is never found in equilibrium, because even in open circuit there is a certain amount of oxygen that reacts with the methanol crossing the membrane ($6FN_{cross} > 0$). This allows to ignore the effect of the reversibility in reaction (5). The resolution of the system of equations (4)-(9) provides expressions for $NO_2$, $CO_{2,ccl}$, $N_{cross}$, $\eta_a$, $\eta_c$ and $i$ as function of $N_m$ and $C_{m,acl}$. Introducing the resulting values for $\eta_a$, $\eta_c$ and $i$ in the equation for the cell potential:

$$f(N_m, C_{m,acl}, \varphi_{e,acl}) \equiv E_{cell} - V - \eta_a(N_m, C_{m,acl}) - \eta_c(N_m) - i(N_m, C_{m,acl})\left(\frac{\delta_{mem}}{\sigma_{mem}} + 2R_{mem/GDL}\right) - 2\varphi_{e,acl} = 0 \tag{10}$$

where $R_{mem/GDL}$ is the contact resistance at the membrane/GDL interface, we obtain a nonlinear equation to calculate $N_m$ as function of the cell voltage $V$ and the local values of $C_{m,acl}$ and $\varphi_{e,acl}$. The numerical solution of this equation at each point of the anode catalyst layer links the 2D and 1D models through the conditions (3a)-(3d), closing the

mathematical model. Once solved the problem for a fixed value of $V$, the calculation of the average current density is immediate. Repeating the process for different values of $V$ the polarization curve is obtained.

The values of the different physical properties involved in the model can be found in [15] except the electric conductivity and initial porosity. The reference anisotropic electric conductivity and initial porosity correspond to the nominal values $\sigma_{ip}^{eff}$ = 17241.4 S/m, $\sigma_{tp}^{eff}$ = 1250 S/m and $\Phi_0$ = 0.8 reported in the product data sheet for Toray® carbon paper THP-H-060 [14].

### 1.4. Structural model (porosity and contact pressure)

The mechanical properties of the (graphite) bipolar plate were assumed to be isotropic, with a Young's modulus E = 10 GPa and a Poisson ratio v = 0.25, while for the gas diffusion layer we considered the nonlinear orthotropic properties of carbon paper. In particular, the GDL mechanical characterization assumed in our study corresponds to Toray® carbon paper TGP-H series, whose properties are widely reported in the open literature.

The following hypothesis were considered for the definition of the GDL mechanical behavior: i) The region under study is located far enough from the cell boundaries so that edge effects can be ignored, and the channels are sufficiently long to consider plane-strain conditions in the streamwise direction $z$ ($\varepsilon_z$ = 0), ii) The aligned geometry of the gas flow channels, added to the higher stiffness of the membrane compared to that of the GDL allows to restrict the displacement in the $y$ direction ($u_y$ = 0) at the lower boundary of the gas diffusion layer, iii) Large strain theory is required to properly reproduce the compression of the porous layer, since GDL strains under the rib area reach typical values between 10-50% during the assembly process, iv) The mechanical behavior of the heterogeneous carbon paper is described through a homogenized constitutive model, commonly used for fibrous materials, v) As in other non-woven felts, GDLs based on carbon paper typically show slightly different orientations of the fibers in the material plane, namely in the machine and cross-machine directions [18]. However, in our simulations the mechanical behavior in the x and z directions is considered equivalent. Due to the through-plane load state and the higher in-plane stiffness, small strains occur in these directions (except for local effects close to the lower corner of the rib). Accordingly, linear elastic behavior is assumed in the x and z directions, neglecting increase of stiffness due to fiber alignment and irreversible deformation due to disentanglement, vi) The GDL material is assumed to have the same properties in tension and compression. Although the properties in the through-plane direction considered in this paper correspond to compression tests, a thin GDL region situated below the channel undergoes tensile strains, a situation which must be taken into account, vii) The response in the $y$ direction is considered elastic. Several authors [7,19] observed hysteretic behavior (weakening of the material) and residual strains in cyclic compression tests. We only analyze the loading due to the first assembly process and also neglect variable loads due to heating or hydration of the membrane that may lead to time variable loads, viii) The shear modulus $G_{xy}$ is assumed to be constant up to failure [18,20], ix) Poisson's ratios $v_{yx}$ and $v_{yz}$ (defined as the ratios between the strain in the $x$ and $z$ directions and the strain in the $y$ direction) are assumed to be equal to zero, since due to the porous microstructure of the material and the high stiffness of the carbon fibers the volume reduction during compression can be attributed to the reduction of pore volume only [18].
Under the assumption stated above, the constitutive equation for the GDL corresponding to the assumed plane-strain conditions adopts the following form using Voigt notation:

$$\begin{bmatrix} d\sigma_x \\ d\sigma_y \\ d\tau_{xy} \end{bmatrix} = \begin{bmatrix} E_x/(1-\nu_{xz}\nu_{zx}) & 0 & 0 \\ 0 & E_y(\varepsilon_y) & 0 \\ 0 & 0 & G_{xy} \end{bmatrix} \begin{bmatrix} d\varepsilon_x \\ d\varepsilon_y \\ d\gamma_{xy} \end{bmatrix} \quad (11)$$

where $\sigma_i$ and $\varepsilon_i$ are respectively the normal true stress and the longitudinal true strain in direction $i$, and $\tau_{xy}$ and $\gamma_{xy}$ are the shear stress and strain associated to directions $x$ and $y$.

According to the results presented by Kleemann et al. [18], obtained for Toray® carbon paper TGP-H-060, the mechanical behavior of the GDL in the material ($xz$) plane is very different to that exhibited in the through-plane ($y$) direction. Since fibers are arranged in a bidimensional structure, the behavior of the material in its plane is much stiffer than in the transverse direction, where the porosity dominates the structural response. Thus, while the elastic moduli in the material plane ($E_x$ and $E_z$) are usually in the order of GPa, in the through-plane direction ($E_y$) it fails to overcome tens of MPa, similarly to the shear modulus ($G_{xy}$) which is also in the order of several MPa.

To characterize the nonlinear behavior of the GDL in the through-plane direction, of special relevance to our study, we have compiled multiple experimental data sets from the literature corresponding to TGP-H-060 [18,19] and TGP-H-090 [7,21] carbon papers. Figure 3 shows the different $E_y(\varepsilon_y)$ curves obtained by numerical derivation of the true stress-strain data obtained from the literature. Note that while the stress data were assumed to be reported as true stress values, since transverse deformations are negligible given the approximately zero Poisson's ratio $\nu_{yx}$, the strain data were assumed to be reported as engineering values, so that they had to be converted to true strains before proceeding with the numerical derivation. As seen in the figure, the $E_y(\varepsilon_y)$ curves exhibit three different regions of GDL response to compressive loads: an initial region for relatively small strains, where the material gradually hardens, an intermediate region with constant Young's modulus, and a final region for large strains where the material hardens again. The nature of these three regions can be understood based on arguments found in the literature. The first region has been attributed both to the flattening of the GDL surface asperities [12] and to the increased number of contacts among fibers caused by the initial closure of pores [6]; the constant region may be traced back to the intrinsic behavior of the microstructure of the porous layer; and the large strain hardening region is most likely due to the final collapse of the GDL and the resulting increase in contacts between fibers at high pore volume reductions [22]. Note that even though the PTFE content in the different GDLs is different, the nonlinear mechanical behavior is qualitatively similar in all cases.

The calculate the porosity field $\Phi(x,y)$ after the fuel cell assembly we assume that the volume changes experienced by the GDL are due solely to the decrease of pore volume, and use large strain theory. Thus the porosity is given by the following expression [23]:

$$\phi(x,y) = \frac{V_p}{V} = \frac{\phi_0 - 1 + e^{\varepsilon_V(x,y)}}{e^{\varepsilon_V(x,y)}} \quad (12)$$

where $\Phi_0$ is the initial porosity, $V_p$ the final pore volume, $V$ the final total volume, and $\varepsilon_V(x,y)$ the true volumetric strain at each point of the elastic material.

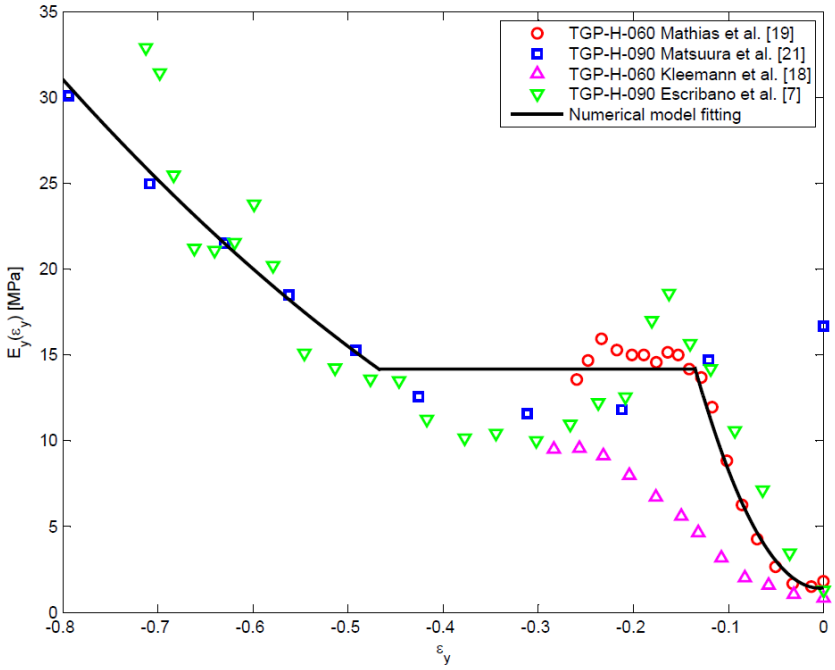


Figure 3: Nonlinear Toray® carbon paper TGP-H-060/090 mechanical behavior in the through-plane direction. $E_y(\varepsilon_y)$ calculated by numerical derivation of the true stress/strain curve obtained from the data reported by Mathias et al. [19] and Matsuura et al. [21] (20 wt.% PTFE), and the stress/displacement data reported by Kleemann et al. [18] and Escribano et al. [7] (10 wt.% PTFE).

### 1.5. Non-uniform anisotropic properties and contact resistances

To evaluate the effect of the obstruction caused by the pore walls on the diffusion fluxes of the chemical species in the GDL we shall refer to the experimental data reported by Flückiger et al. [24] and Möst et al. [25] using a novel electrochemical diffusimetry method. These authors have characterized the anisotropic effective diffusivity as a function of compression for different GDL types and hydrophobic treatments. To give mathematical expression to these results, we have fitted the reported effective in-plane (*ip*) and through-plane (*tp*) diffusivities for carbon paper TGP-H-060 of various PTFE contents using exponential functions:

$$\frac{D_{i,j}^{eff,ip}}{D_{i,j}} = \frac{\phi}{\tau_{ip}} = 0.029 e^{3.8\phi(x,y)}, \quad \frac{D_{i,j}^{eff,tp}}{D_{i,j}} = \frac{\phi}{\tau_{tp}} = 0.0065 e^{5.021\phi(x,y)} \qquad (13a,b)$$

where $D_{i,j}$ is the binary diffusivity of species $i$ in species $j$, $D_{i,j}^{eff}$ the effective binary diffusivity of those species in the porous material, and $\tau$ is the tortuosity. Due to the in-plane arrangement of the fibers the pores are preferentially oriented in this direction, which results in lower tortuosity and thus higher effective diffusivity. The above expressions reflect indeed that the anisotropy between the in-plane and through-plane direction is about 2 and increases as the GDL is compressed due to the realignment of fibers. It is worth noting that the isotropic spherical agglomerate model of Bruggeman and the more realistic anisotropic random fiber model of Tomadakis and Sotirchos, widely used in the literature, tend to oversimplify the complex geometry of real GDLs. Both models ignore, for example, the influence of structural irregularities such as binder and PTFE, resulting in an overestimation of the effective diffusivity by a factor of about 2 [24, 25, 26].

The effective electrical conductivity has been correlated with the experimental data reported by Reum for carbon paper TGP-H-060 with 20% PTFE [27]:

$$\sigma_{ip}^{eff} = 48221 - 46729\phi(x,y),\ \sigma_{tp}^{eff} = 6581.7 - 7228.9\phi(x,y) \quad [S/m] \qquad (14a,b)$$

As specified by the manufacturer [14], the measured conductivity in the in-plane direction is about one order of magnitude higher than that in the through-plane direction because of the preferential orientation of the fibers. In contrast to the effective diffusivity the decrease in porosity increases the electrical conductivity due to an increasing number of contact points. In particular, the in-plane conductivity increases linearly with decreasing thickness (porosity) so that the in-plane resistance remains almost constant [18].

To characterize the contact resistance at the rib/GDL interface we have collected several experimental data sets from the literature corresponding to the interaction between a graphite bipolar plate and TGP-H series Toray® carbon paper [19,28,29,30]. Even though the PTFE content in the measured GDLs is different and affects the value of the contact resistance, we have considered an averaged fit to all compiled data:

$$R_{rib/GDL} = 4.15 p_c^{-0.85} \quad [m\Omega cm^2] \qquad (15)$$

where $p_c$ is the contact pressure at the rib/GDL interface expressed in MPa.

Unlike the contact resistance at the rib/GDL interface, it is very hard to experimentally test the electrical contact resistance at the membrane (CL)/GDL interface and very few studies can be found in the open literature. Its value is strongly influenced by the presence of a microporous layer (MPL) [19]. When a MPL is coated to the GDL the contact resistance can be similar to that observed at the rib/GDL interface as reported by Kleemann et al. [18], but if the MPL is not present the values can be one order of magnitude higher than that observed at the rib/GDL interface as reported by Nitta et al [12]. Although these interesting findings, a large body of work is still needed to accurately predict the value of the membrane (CL)/GDL contact resistance. In this paper we have tested the response of the cell for two cases, one corresponding to a membrane/GDL contact resistance equal to that at the rib/GDL interface and another with a membrane/GDL contact resistance ten times higher.

## 2. Numerical results

Figures 4 and 5 show the polarization curve and the power density curve associated to different compression ratios of the GDL (expressed as a percentage of the initial thickness) for equal membrane/GDL and rib/GDL contact resistances. Due to the moderate value of the contact resistances the compression needed to significantly reduce the Ohmic losses is quite small. The maximum power density is achieved for a compression ratio around 10-15%. For higher values, the reduction of the effective diffusivity increases mass transport losses causing a decrease in the maximum power (and current density). On the other hand, Figs. 6 and 7 show the polarization curve and the power density curve for a membrane/GDL contact resistance ten times higher than that at the rib/GDL interface. By increasing the membrane/GDL contact resistance the compression ratio needed to maximize the cell power density increases to about 20-25%. As can be seen, for small compressions the Ohmic losses become too high and the performance is low. However, if the compression ratio is excessive the mass transport

losses lead to a decrease in the maximum power (and current density). It is worth noting that the decrease in the power density for compression ratios higher than the optimum is more significant for the case with lower membrane/GDL contact resistance. This result is expected to depend on the concentration of methanol considered at the channel/GDL interface and should be studied further.

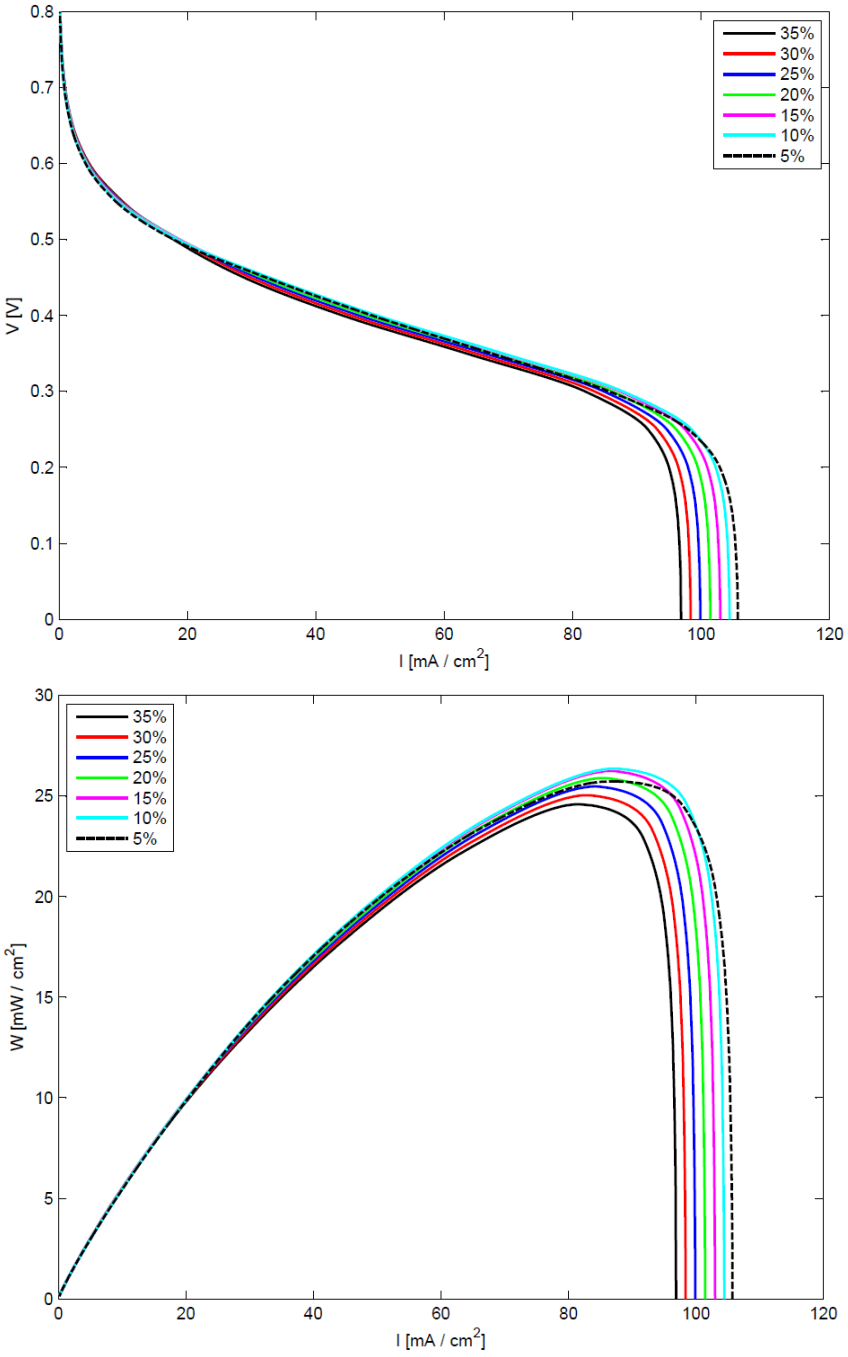


Fig. 4 & Fig.5: Polarization curve and power density curve for different compression ratios of the GDL (expressed as a percentage of the initial thickness). The membrane/GDL contact resistance is assumed to be equal to that at the rib/GDL interface.

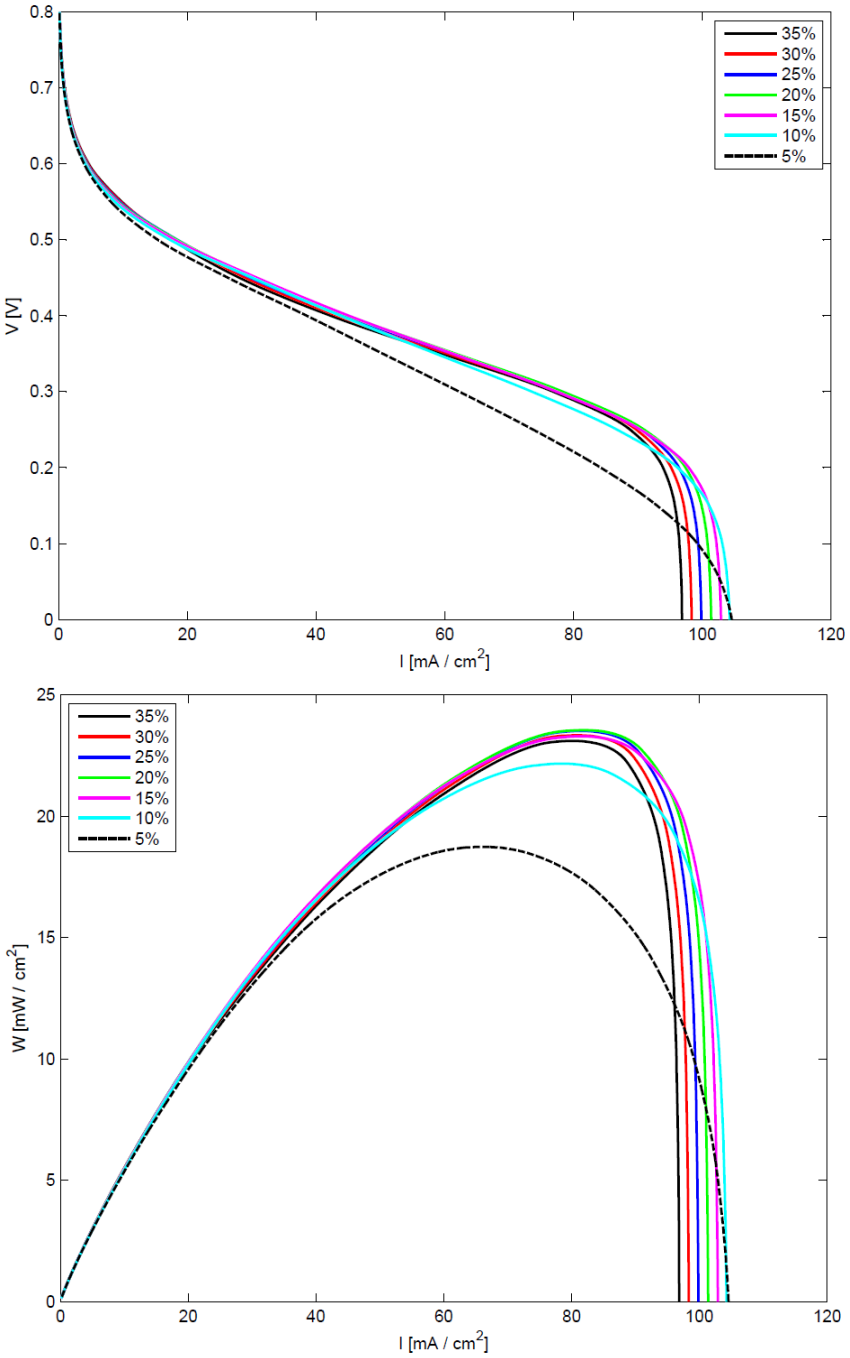


Fig. 6 & Fig. 7: Polarization curve and power density curve for different compression ratios of the GDL (expressed as a percentage of the initial thickness). The membrane/GDL contact resistance is assumed to be ten times that at the rib/GDL interface.

Fig. 8 shows the local current density profile at the anode catalyst layer for different cell voltages when the membrane/GDL is one order of magnitude higher. For high voltages (0.6-0.8 V), the current density under the channel is almost the same regardless of the compression ratio. However, the current density under the rib increases with compression. This behavior may be explained by the reduction of the effective diffusion path as the compression ratio is higher. At intermediate voltages (0.3-0.5 V) we can see the apparition of a local maximum near the channel rib interface due to the opposing effects caused by the high membrane/CL contact resistance under the channel and the low diffusivity under the rib. Note the low current density achieved with a 5% compression ratio compared with the other compression ratios because of the extremely high contact resistance at the GDL

interfaces. Finally, for low cell voltages (0-0.2 V) the local maximum disappears. The current density profile increases from the region under rib to the region under the channel with sigmoidal shape due to mass transport limitations associated with the methanol shortage at very high cell current densities. Interestingly, the different profiles get closer until they collapse into almost one at zero voltage.

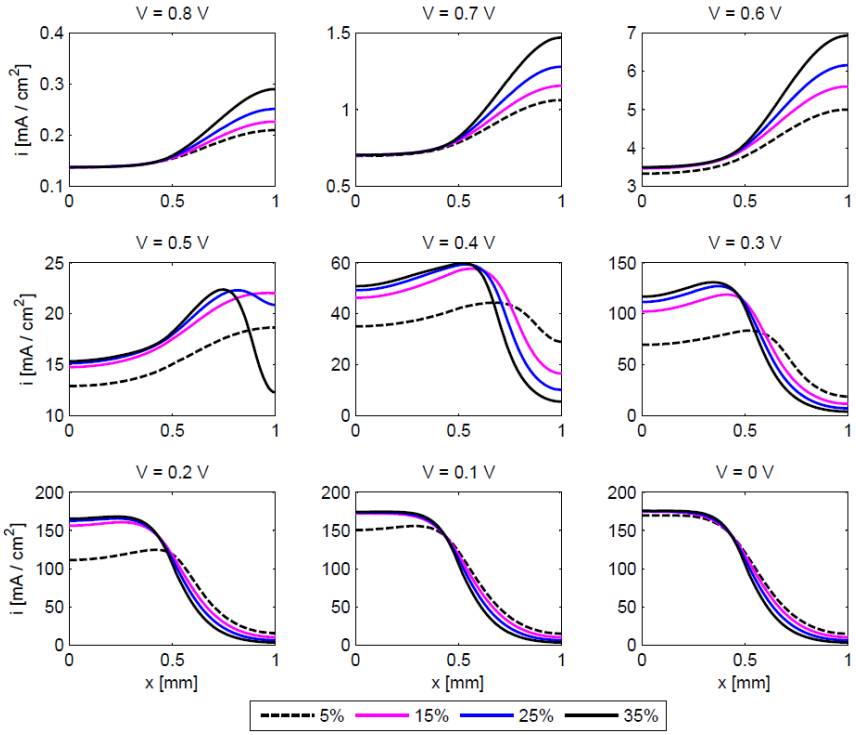


Fig. 8: Local current density profile for different compression ratios (expressed as a percentage of the initial thickness) at different cell voltages. The membrane/GDL contact resistance is assumed to be ten times that at the rib/GDL interface.

## 3. Conclusions

A multiphysics across-the-channel model for the anode of a liquid feed Direct Methanol Fuel Cell (DMFC) has been developed to simulate the anisotropic properties of the GDL and inhomogeneous compression effects (non-uniform porosity, diffusivity, bulk electrical conductivity and electric contact resistances at the GDL interfaces). Some interesting results have been extracted from the work-in-progress, showing the impact of the assembly compression on the cell performance. Along with the effective diffusivity, the most influential parameter appears to be the contact resistance at the membrane/GDL interface. The combined effect of both factors causes significant spatial variations in the local current density depending on the operating voltage.

# References


[1] Fuel Cell Handbook, 7th Edition, EG&G Technical Services, Inc., Under U.S. Dept. of Energy Contract DE-AM26-99FT40575, National Energy Technology Lab., Morgantown, WV, USA, 2004.

[2] F. Barbir, PEM Fuel Cells: Theory and Practice, Elsevier Academic Press (2005).

[3] Z. H. Wang, C. Y. Wang, Mathematical Modeling of Liquid-Feed Direct Methanol Fuel Cells, J. Electrochem. Soc. 150 (4) A508-A519 (2003).

[4] V. Mehta, J. S. Cooper, Review and analysis of PEM fuel cell design and manufacturing, J. Power Sources 114 (2003) 32-53.

[5] X. Li, I. Sabir, Review of bipolar plates in PEM fuel cells: Flow-field designs, Int. J. Hydrogen Energy 30 (2005) 359-371

[6] V. Radhakrishnan, P. Haridoss, Differences in structure and property of carbon paper and carbon cloth diffusion media and their impact on proton exchange membrane fuel cell flow field design, Materials Design 32 (2011) 861-868.

[7] S. Escribano, J. Blachot, J. Ethève, A. Morin, R. Mosdale, Characterization of PEMFCs gas diffusion layers properties, J. Power Sources 156 (2006) 8–13.

[8] Y. Zhu, C. Liu, J. Liang, L. Wang, Investigation of the effects of compression pressure on direct methanol fuel cell, J. Power Sources 196 (2011) 264-269.

[9] A. Kusoglu, A. M. Karlsson, M. H. Santare, S. Cleghorn, W. B. Johnson, Mechanical behavior of fuel cell membranes under humidity cycles and effect of swelling anisotropy on the fatigue stresses, J. Power Sources 170 (2007) 345-358.

[10] I. Nitta, O. Himanen, M. Mikkola, Contact resistance between gas diffusion layer and catalyst layer of PEM fuel cell, Electrochem. Comm. 10 (2008) 47-51.

[11] I. Nitta, T. Hottinen, M. Mikkola, Thermal conductivity and contact resistance of compressed gas diffusion layer of PEM Fuel Cell, Fuel Cells 08 (2008) 111-119.

[12] I. Nitta, Inhomogeneous compression of PEMFC gas diffusion layers, Doctoral dissertation, Helsinki (Finland), 2008.

[13] A. Bazylak, D. Sinton, Z.-S. Liu, N. Djilali, Effect of compression on liquid water transport and microstructure of PEMFC gas diffusion layers, J. Power Sources 163 (2007) 784-792.

[14] Toray® Carbon fiber Paper “TGP-H” datasheet, Toray Industries, Inc.

[15] M. Vera, A single-phase model for liquid-feed DMFCs with non-Tafel kinetics, J. Power Sources 171 (2007) 763-777.

[16] Z. Miao, Y-L. He, J-Q Zou, Modeling the effect of anisotropy of gas diffusion layer on transport phenomena in a direct methanol fuel cell, J. Power Sources 195 (2010) 3693-3708.

[17] J. P. Meyers, J. Newman, II. Modeling and Data Analysis of Transport and Kinetic Phenomena, J. Electrochem. Soc. 149 (6) A718-A728 (2002).

[18] J. Kleemann, F. Finsterwalder, W. Tillmetz, Characterisation of mechanical behavior and coupled electrical properties of polymer electrolyte membrane fuel cell gas diffusion layers, J. Power Sources 190 (2009) 92-102.

[19] M. Mathias, J. Roth, J. Fleming, W. Lehnert, in Handbook of Fuel Cells Fundamentals, Technology and Applications, Volume 3: Fuel Cell Technology and Applications, Chapter 46, W. Vielstich, H. A. Gasteiger, A. Lamm (Editors), 2003 John Wiley & Sons, Ltd.

[20] Y. Lai, P. A. Rapaport, C. Ji, V. Kumar, Channel intrusion of gas diffusion media and the effect on fuel cell performance, J. Power Sources 184 (2008) 120-128.

[21] T. Matsuura, M. Kato, M. Hori, Study on metallic bipolar plate for proton exchange membrane fuel cell, J. Power Sources 161 (2006) 74-78.

[22] P. Yi, L. Peng, X. Lai, A Numerical Model for Predicting Gas Diffusion Layer Failure in Proton Exchange Membrane Fuel Cells, J. Fuel Cell Sci. Technol. 8 (2011) 011011.
[23] P. Zhou, C. W. Wu, Numerical study on the compression effect of gas diffusion layer on PEMFC performance, J. Power Sources 170 (2007) 93-100.
[24] R. Flückiger, Transport Phenomena on the Channel-Rib Scale of Polymer Electrolyte Fuel Cells, Doctoral dissertation, ETH Zurich (Switzerland), 2009.
[25] M. Möst, M. Rzepka, U. Stimming, Analysis of the diffusive mass transport in the anode side porous backing layer of a direct methanol fuel cell, J. Power Sources 191 (2009) 456-464.
[26] J. Becker, R. Flückiger, M. Reum, F. N. Büchi, F. Marone, M. Stampanonic. Determination of Material Properties of Gas Diffusion Layers: Experiments and Simulations Using Phase Contrast Tomographic Microscopy, J. Electrochem. Soc. 156 (10) B1175-B1181 (2009).
[27] M. Reum, Sub-Millimeter Resolved Measurement of Current Density and Membrane Resistance in Polymer Electrolyte Fuel Cells (PEFC), ETH Zurich (Switzerland), 2008.
[28] X. Lai, D. Liu, L. Peng, J. Ni, A mechanical-electrical finite element method model for predicting contact resistance between bipolar plate and gas diffusion layer in PEM fuel cells, J. Power Sources 182 (2008) 153-159.
[29] L. Zhang, Y. Liu, H. Song, S. Wang, Y. Zhou, S. J. Hu, Estimation of contact resistance in proton exchange membrane fuel cells, J. Power Sources 162 (2006) 1165-1171.
[30] Y. Zhou, G. Lin, A. J. Shih, S. J. Hu, A micro-scale model for predicting contact resistance between bipolar plate and gas diffusion layer in PEM fuel cells, J. Power Sources 163 (2007) 777-783.